UNIVERSITY OF CALIFORNIA
RIVERSIDE

Search for Standard Model Production of Four Top Quarks at CMS in the Dilepton Channel at a Center of Mass Energy of 13 TeV

A Dissertation submitted in partial satisfaction
of the requirements for the degree of

Doctor of Philosophy

in

Physics

by

Jesse Alan Heilman

August 2016

Dissertation Committee:

Professor Stephen Wimpenny, Chairperson
Professor Robert Clare
Professor Owen Long

The Dissertation of Jesse Alan Heilman is approved:

Committee Chairperson

University of California, Riverside

Acknowledgments

I am grateful to my advisors, Professor Stephen Wimpenny and Professor Robert Clare, without whose help, I would not have been here. I would also like to thank Dr. James Keaveny, Professor Freya Blekman, and Lana Beck for their essential guidance and collaboration. Additional thanks goes to the CMS CSC collaboration for the irreplaceable experience of contributing to the construction and maintenance of the CMS Detector.

To my family for lifting each successive generation.

"If I have seen further, it is by standing on the shoulders of giants."

(Sir Issac Newton)

ABSTRACT OF THE DISSERTATION

Search for Standard Model Production of Four Top Quarks at CMS in the Dilepton Channel at a Center of Mass Energy of 13 TeV

by

Jesse Alan Heilman

Doctor of Philosophy, Graduate Program in Physics
University of California, Riverside, August 2016
Professor Stephen Wimpenny, Chairperson

The search for the production of four top quarks decaying in the dileptonic channel in proton-proton collisions at the LHC is presented. The analysis utilizes the data recorded by the CMS experiment at a center of mass energy of 13 TeV in 2015, which corresponds to an integrated luminosity of 2.6 fb^{-1}. A boosted decision tree algorithm is used to select signal and suppress background events. A 95% confidence level upper limit on the four top quark production cross-section of $14.9 \times \sigma^{SM}_{t\bar{t}t\bar{t}}$ is observed with $22.3^{+16.2}_{-8.4} \times \sigma^{SM}_{t\bar{t}t\bar{t}}$ expected. A combination is then performed with a parallel analysis of the single lepton channel to extend the reach of the search. The combined 95% confidence level upper limit on the four top production cross-section is observed to be $10.2\times$ $\sigma^{SM}_{t\bar{t}t\bar{t}}$ with $10.8^{+6.7}_{-3.8}\times$ $\sigma^{SM}_{t\bar{t}t\bar{t}}$ expected: the most precise upper limit on standard model four top production to date.

Contents

List of Figures

List of Tables

Chapter 1

The Standard Model

The Standard Model of Particle Physics (SM) is currently the most well understood and best tested description of elementary particles and their interactions. It describes the interactions of quarks and gluons through the strong nuclear forces as a $SU(3)$ gauge theory and the electroweak sector as a $SU(2)\times U(1)$ interaction mediated by the weak gauge bosons $W^{\pm}$, Z^0 and the photon (γ).

The SM is widely interpreted to describe the interactions of elementary particles and forces. From the discovery of the electron by Thompson, through the theory of Electromagnetic fields by Maxwell, the discovery of nucleon substructure in deep inelastic scattering experiments, all the way to the discovery of the Higgs boson at the LHC in 2012: the Standard Model has continued to be one of the most precisely tested theories in the history of Particle physics. While the SM is lacking in some areas, such as connections to the dark sector hypothesized through cosmological observations, it does offer a precise description, and natural grouping as shown in in Fig. 1.1, of the interactions between the smallest constituents of matter we have observed.

1.1 Elementary Particles

As technology developed to allow physicists to examine smaller and smaller pieces of matter, many different layers of structure were observed. The Standard Model dictates that at the most fundamental level, matter consists of two types of particles: quarks and leptons. Both of these classes of particles have spin of $\frac{1}{2}$ (in units of $\hbar$) and no further underlying structure at currently probed scales. They interact with the Electroweak $SU(2)\times$

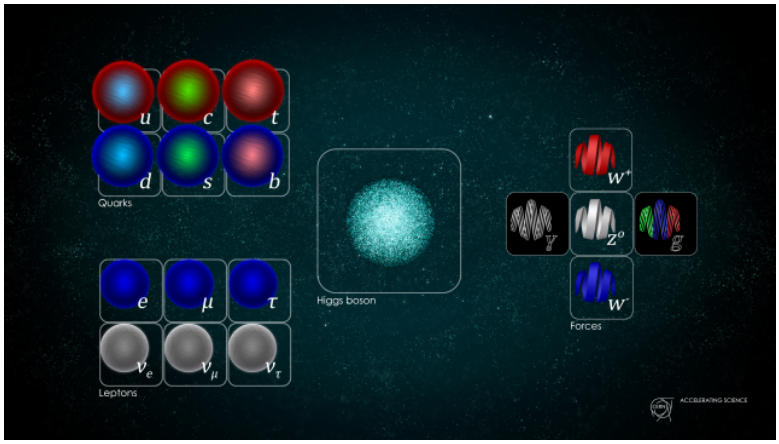

Figure 1.1: The Standard Model (SM) of particle physics[35].

$U(1)$ forces but only quarks interact with the Strong $SU(3)$ force described by Quantum Chromodynamics. Table 1.1 shows a summary of the properties of the quarks and leptons. Each of these particles also has an associated anti-particle (often denoted with a line above the the symbol) which carries opposite quantum numbers as its partner.

In the SM, the particles are arranged into three 'generations'. The up quark, down quark, and the electron with its associated neutrino make up the first generation; the charm quark, strange quark, muon, and muon neutrino make up the second generation; and the top quark, bottom quark, tau, and tau neutrino make up the third one. The generations are connected through the weak interaction by decays from the higher generations to the lower ones such as:

$$\mu^- \rightarrow e^- + \bar{\nu}_e + \nu_\mu. \tag{1.1}$$

Weak interactions are constrained by the conservation of lepton number (L) which must be conserved in all leptonic interactions. A different lepton number is assigned to each generation and anti-particles carry negative lepton number. This is described in Equation 1.1, where the both the initial and final states carry $L_e = 0$ and $L_\mu = 1$.

The number of lepton flavors, and hence particle generations, has been the subject of much study. Experiments at LEP, probing decays of the Z^0 boson, showed that to a very high precision, there are only 3 flavors of light neutrinos below the Z^0 mass scale. This is consistent with the standard model prescription of three particle generations. An additional complication in the neutrino sector is shown in solar neutrino oscillation observations, where

Table 1.1: Properties of quarks and leptons.

Lepton	**Q/e**	**Mass (MeV)**	**Lepton Flavor**
ν_e	0	$< 2 \times 10^{-6}$	$L_e = 1$
e	-1	0.511	$L_e = 1$
ν_μ	0	< 0.19	$L_\mu = 1$
μ	-1	105.66	$L_\mu = 1$
ν_τ	0	< 18.2	$L_\tau = 1$
τ	-1	1777.0	$L_\tau = 1$
Quark	**Q/e**	**Mass (GeV)**	**Quark Flavor**
u	$+\frac{2}{3}$	2.3×10^{-3}	N/A
d	$-\frac{1}{3}$	4.8×10^{-3}	N/A
s	$+\frac{2}{3}$	95×10^{-3}	$C = 1$
c	$-\frac{12}{3}$	1.275	$S = 1$
t	$+\frac{2}{3}$	173.5	$T = 1$
b	$-\frac{1}{3}$	4.18	$B = 1$

it was demonstrated that neutrinos can change from one flavor into another. This mixing means that the neutrino sector, while very light, must have non-vanishing mass and that their mass and flavor states are not orthogonal.

The quarks also are arranged into three generations that are traditionally connected to the lepton generations. Each generation forms an isospin ($I = \frac{1}{2}$) doublet with the $I_z = +\frac{1}{2}$ particle denoted 'up-type' and the $I_z = -\frac{1}{2}$ denoted 'down-type'. Up-type quarks carry an electric charge of $Q = \frac{2}{3}e$ with down-type quarks carrying $Q = -\frac{1}{3}e$. Quarks also exhibit their own version of flavor conservation with flavor numbers shown in Table 1.1. This is more complicated in the quark sector however, due to the presence of the quantum chromodynamic color charge and that members of the same doublet do not share a flavor quantum number.

1.2 Interactions and Forces

The spin $\frac{1}{2}$ fermions discussed above only make up part of the picture that the standard model paints. Each fermion interacts with one or more of the fundamental forces: Electromagnetic, Weak Nuclear, and Strong Nuclear. Additionally, since all the fermions have mass, they will interact gravitationally. However, since the gravitational coupling constant is so much weaker than any other force (23 orders of magnitude weaker than the

electromagnetic coupling constant) and there has been no successful description of quantum gravity, we will not discuss gravitational interactions of the fundamental particles here.

Classically, the interaction of matter with forces was described by field equations such as Maxwell's equations or Newton's description of gravity. The advent of the quantum, relativistic description of matter lead to the forces being described in terms of the exchange of bosons between particles. Thus, a force carrying boson was associated with each type of force interaction: the photon for electromagnetic interactions, the $W^{\pm}$ and Z^0 bosons for the weak force, and the gluon for the strong force.

The photon is a massless boson that does not carry the electromagnetic charge and has an energy directly proportional to its angular frequency in units of $\hbar$. Thus, it can not interact with itself. Since it is massless and cannot self interact, the photon requires the presence of some other massive particle in order to pair produce fermions.

The weak force has a charged current carrier, the $W^{\pm}$, and a neutral current carrier, the Z^0. The charged current allows for processes mediated through the weak force where the particles can have their charge changed. This is obviously seen in the weak quark decays mentioned in 1.1 such as

$$t \rightarrow b + W^{+} \rightarrow b + \mu^{+} + \nu_{\mu} \tag{1.2}$$

where the charge migrates from the t branch through the W^{+} and into the lepton system. Perhaps one of the most interesting properties of the weak interaction is the fact that it maximally violates parity. The weak force couples preferentially to the left-handed helicity states of leptons leading to effects such as helicity suppression in pion decays. The neutral weak current provides additional phase space for pair production and annihilation as well as the production of pairs of neutrinos.

The strong nuclear force is responsible for the confinement of nucleons in atomic nuclei as well as interactions between quarks which carry the strong charge: color. While the electromagnetic force only has a single charge (with a positive and negative aspect) the strong force has three charges: (R)ed, (G)reen, and (B)lue (and their anti-colors $\bar{R}\bar{G}\bar{B}$). This convention arose because stable hadrons are only allowed to be 'color neutral' and the analog of additive color in visible light provided an appropriate metaphor. Color neutral combinations are a pair of a color and its anti-color or an equal mixing of the three charges (RGB or $\bar{R}\bar{G}\bar{B}$). This leads to the most common hadrons being Baryons (made from 3 quarks) and Mesons (made from 2 quarks). More exotic color neutral states have

been postulated and indeed, in 2013, a pentaquark hadron was discovered at the LHCb experiment[4].

The gluon that mediates the strong interaction is, like the photon, massless. However, unlike the photon, it carries color charge itself. The gluon itself is bi-colored carrying a color and an anti-color (eg $R\bar{B}$). While there are nine possible color anti-color combinations, the SU(3) nature under which the strong force is described shows that colorless gluons ($R\bar{R}$, $G\bar{G}$, $B\bar{B}$) are actually not linearly independent. One can always express one of those states in terms of the other two. This results in there being 8 valid color combinations for gluons and, in fact, experimental results confirm this.

Another key difference between the strong and electromagnetic forces is that they have opposite behaviors as you increase the distance scale of the interaction. When two colored particles are separated, the potential between them increases. A metaphor of a spring is often used; though a spring's behavior is not described by the same form. This leads to a behavior called hadronization. When the potential energy between the two particles becomes high enough, a particle antiparticle pair can be vacuum produced. This process repeats until enough pairs have been produced that the final state particles are strongly bound in color neutral hadrons.

The final standard model boson was first observed in 2012 by the CMS and ATLAS experiments at the Large Hadron Collider (LHC). The Higgs boson had been postulated in 1964 as mediating the process by which particles gained mass through spontaneous breaking of symmetry below some energy threshold. Numerous studies are currently being carried out by physicists at CERN and studies of the Higgs are expected to yield pivotal results in the next few years of running at the LHC.

1.3 Beyond the Standard Model

Despite its many successes in describing the basic structure of matter, the Standard Model is not perfect. The particles and interactions it describes paint an incomplete picture of the universe. Particularly, the standard model is, at times, in conflict with astronomical observations. Above, it is already mentioned that the SM has no way of incorporating gravity into its descriptions of particle interactions and, in fact, every attempt thus far has been unsuccessful despite the fact that gravity is by far the most dominant force acting on larger scales in the universe. More than this, astronomical observations estimate that the

fraction of the energy in the universe made up of standard model particles is only $\sim 5\%$. The rest is hypothesized to be made up of so called 'dark matter' and 'dark energy'. The search for dark matter in particular is high on the list of goals for experimental physicists looking to extend the SM.

Additionally, the standard model's prescription of neutrinos is one of massless fermions. As mentioned earlier in this chapter, solar neutrino observations established that neutrino species can mix, indicating some non-vanishing neutrino masses. Further, the mass difference squared between the 3 energy eigenstates has been measured lending evidence that at least 2 of those states have mass. Since the only the square of the mass differences are known, it is unknown what the mass ordering of the neutrinos is. The existence of a non-vanishing neutrino mass also suggests that there may be a right handed coupling to the neutrino sector that has yet to be observed.

These puzzles and many others demonstrate that the standard model is an incomplete description of the universe and much research needs to be done to complete our understanding. With the confirmation of the existence of the Higgs boson, many experiments, including the LHC, are endeavoring to expand our understanding into these 'Beyond the Standard Model' (BSM) regions. One particular problem with relevance to this analysis is the issue of the top quark mass. At 175.3 GeV, the top quark is two orders of magnitude heavier than the next heaviest fermion and contributes greatly to the physics of electroweak symmetry breaking through its coupling to the Higgs boson mass. Thus, a study of top quarks and their associated interactions is important to our understanding of physics above the electroweak symmetry breaking scale.

Chapter 2

Production of Four Top Quarks

The top quark is the most massive of the standard model particles[2]. First observed at the Tevatron at Fermilab in 1995 by the CDF and D0[5] collaborations, it completed the three generational structure of the quark sector proposed by the standard model. Since then, it has been the subject of much study due to the unique property that it decays before hadronization can take place. This means that by studying the decays of the top quark we can examine how a 'bare' quark behaves in the absence of other quantum chromodynamic effects. Additionally, due to the large mass, top quarks contribute greatly to the couplings of the Higgs boson and precision measurements of the top quark and its properties are essential to measurements involving the Higgs.

The mystery of the scale of the top quark mass is one that has garnered a considerable amount of theoretical speculation. One possible probe into possible BSM interactions with the top quark is to examine the production of four top quarks simultaneously; more specifically, two top-antitop pairs. Production of four top quarks is possible under the prescription provided by the Standard Model but many BSM theories such as the presence of massive colored bosons, top compositeness, extra dimensions, and certain versions of supersymmetry enhance the production cross section of the four top process[18, 9, 49, 21, 22, 36]. A measurement of this production cross section has never been performed and would provide a solid data point around which to interpret these and other BSM theories. In this analysis, we aim to set an upper limit on the production cross section of the four top process.

Before the details of the measurement can be properly discussed, it is important to understand the processes that go into the production and measurement of processes

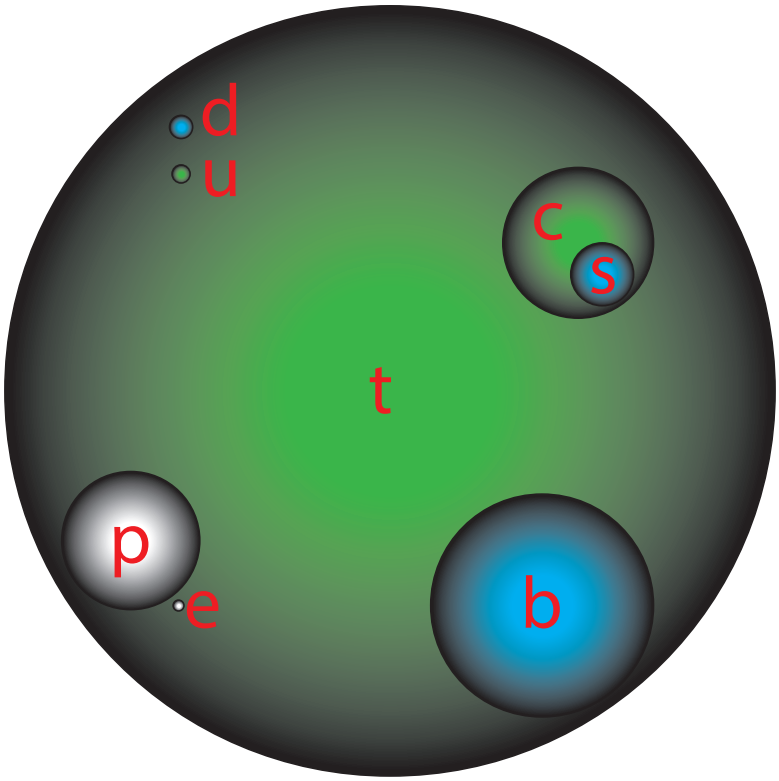

Figure 2.1: Relative masses of the quarks (with the proton and electron for reference) represented by the volume of a sphere.

involving top quarks. In the following sections of this chapter, a description of top quark phenomenology is presented, followed by descriptions of the leading order production of four top quarks under the standard model. Next, a phenomenological comparison with the most common top quark production method is detailed followed by a brief description of previous attempts at measurement of four top production.

2.1 Top Quark Phenomenology

The top quark decays with a nearly unity branching ratio to a bottom quark and associated W boson. Theoretically, the decay path to a strange or down quark is not forbidden but it is highly suppressed. For all intents and purposes in most physics analyses the top is assumed to decay in the bottom quark path with unity probability. Thus, the final states of top quark decays are characterized by how the W boson decays: either leptonically or hadronically. Processes involving multiple top quarks are classified by

how many W bosons decay leptonically.

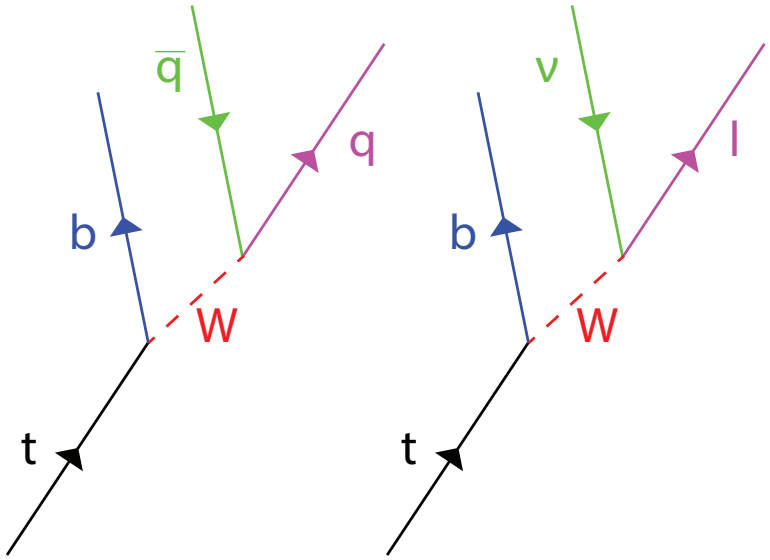

Figure 2.2: Hadronic(left) and Leptonic(right) decays of a top quark.

The most common form of top quark production in colliders is the production of top-antitop pairs. At the LHC this can occur through gluon-gluon or quark-antiquark interactions. The gluon-gluon production path dominates $t\bar{t}$ production due to the relative strength of the Parton Density Functions (PDFs) of the initial state partons in proton-proton collisions. Since there are no valence level antiquarks in protons, the only way for an initial state antiquark to be present is through a sea quark that must be produced from a gluon inside the proton. Thus the quark-antiquark process is suppressed with respect to the gluon-gluon path.

Single top quark production is also possible in the SM. There are three different dominant production mechanisms for single top quarks at the LHC: s-channel, t-channel, and associated production with a W boson as seen in Figure 2.4.

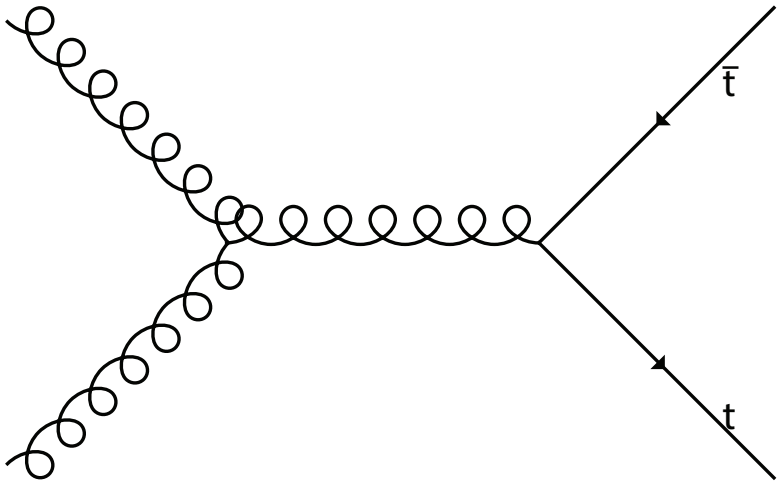

Figure 2.3: Leading order gluon fusion production of $t\bar{t}$ pairs.

2.2 Leading Order Production of Four Top Quarks

The production of four top quarks at the LHC proceeds in a similar fashion to that of $t\bar{t}$ pairs. The gluon-gluon pathway dominates the production cross section while the quark-antiquark pathway is suppressed in proton-proton collisions as anti-quarks are only present from sea quarks. However, production of four top quarks is a higher order process and thus greatly suppressed with respect to $t\bar{t}$ production. Theorists have calculated the SM production cross section at $\sqrt{s} = 13$ TeV to next to leading order precision to be $\sim 9.1\text{fb}^{-1}$[7, 12].

2.3 Comparison of $t\bar{t}$ and $t\bar{t}t\bar{t}$ Production

The dominant background when searching for events with four top quarks is pair production of top quarks. At $\sqrt{s} = 13$ TeV, $t\bar{t}$ has an inclusive SM production cross section of 831.76 pb^{-1} making a naive signal to background ratio on the order of 10^{-5}. Thus proper understanding of the phenomenological differences between these two processes is essential to the construction of a strategy to disentangle them. For the purposes of this discussion, I will assume the dileptonic decay channel as this is the type of event that this analysis focuses on.

The largest area of difference between the two processes in the dilepton channel is the presence of the two additional hadronically decaying top quarks. The two extra top

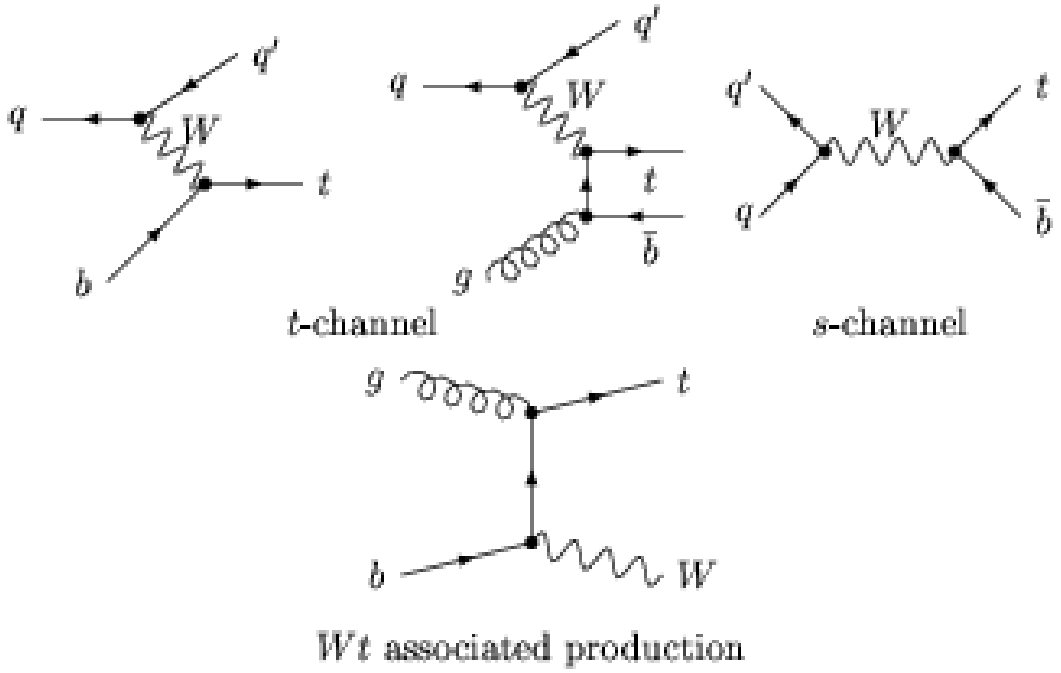

Figure 2.4: Single top quark production at the LHC[13].

quarks will contribute two b partons and 4 other partons to the event that will not be present in dileptonic $t\bar{t}$. One would then think that it would be straightforward to disentangle the two processes by just looking at events with a high jet multiplicity (see Section 6.1 for a definition of jets). Practically, the presence of extra jets from sources such as gluon splitting, Initial State Radiation (ISR), or Final State Radiation (FSR) can add jets to $t\bar{t}$ events. Even though the probability of adding a significant number of extra jets is small, the 5 orders of magnitude enhancement in the $t\bar{t}$ cross section when compared to the four top cross section makes the separation of signal and background difficult. These extra jets will, however, on average have a softer energy spectrum since they come from bremstrahlung processes and their emission probability falls off rapidly with increasing energy. Thus the presence of many hard jets in an event could indicate that it is a four top event rather than a two top event.

Another possible area of difference is the presence of same sign leptons. Dileptonic $t\bar{t}$ production always produces leptons of opposite signs, where as there is a probablilty that the two W bosons that decay leptonically will be of the same sign in four top production.

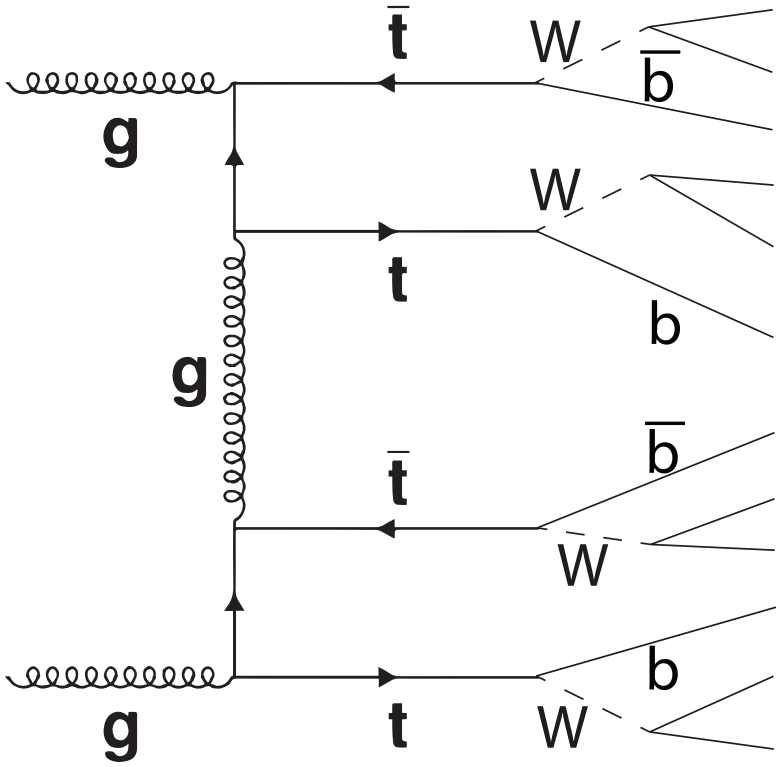

Figure 2.5: One of the leading order gluon-gluon diagrams for $t\bar{t}t\bar{t}$ production.

While this is a potentially huge source of differentiation, using same sign lepton pairs requires a different strategy based on lepton charge mis-identification that is not under the purview of this analysis. Thus, for this search, we focus only on events with opposite sign lepton pairs and little difference is expected in the leptonic information between signal and background.

Finally, one might exploit the fact that at 13 TeV, the probability for $t\bar{t}$ production to occur above threshold is considerably more likely than for four top production. Correlated to the above discussion on the presence of extra jets in $t\bar{t}$ events that will allow them to mimic four top events, these extra jets provide energy for the $t\bar{t}$ system to recoil from, making them less back to back in the detector's rest frame. Exploiting this topological difference also has potential to provide discrimination power between four and two top production.

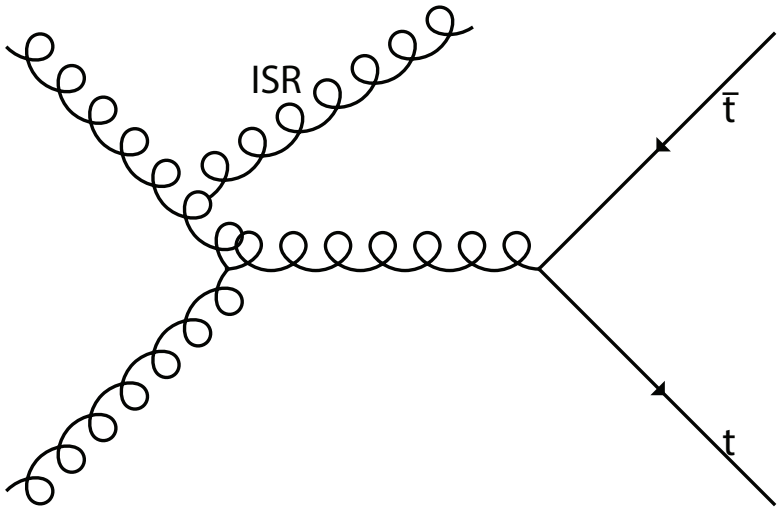

Figure 2.6: Initial State Radiation from $t\bar{t}$ production.

2.4 Previous Searches

This analysis focuses on data collected at the Large Hadron Collider during the first year of Run II in 2015. Previously, another search was carried out with the LHC Run I data at 8 TeV where the leading order four top production cross section is ≈ 1 fb. The strategy used in that analysis focused on the single lepton decay channel using Boosted Decision Trees. The analyzers showed that splitting the events into categories based on the jet multiplicity and then performing a simultaneous fit to these categorized distributions increased the sensitivity of the analysis significantly. Using this strategy, they obtained a 95% CL upper limit on the four top production cross section of 63 fb with 42^{+18}_{-13} fb expected[42]. At the time, this was the tightest limit. This analysis will extend to the dilepton channel using the 13 TeV data recorded during 2015.

Chapter 3

The Large Hadron Collider

The Large Hadron Collider, located at CERN, is the largest and most powerful particle accelerator in the world. In March 2010, it began colliding protons with a center of mass energy of $\sqrt{s} = 7$ TeV, about 50% of the nominal design energy. Over the next few years, combined with some upgrade efforts, the LHC dialed up its energy and intensity. In 2015, it reached a center of mass energy of $\sqrt{s} = 13$ TeV.

Installed in the retrofitted tunnel left by the Large Electron-Positron (LEP) collider, the LHC spans a circumference of 26.7 km under the French-Swiss countryside near the city of Geneva, Switzerland. Crossing the Swiss-French border 4 times, the LHC is comprised of 1232 superconducting bending dipoles that steer the beam around the circumference of the LHC. Thousands of other multi-pole magnets (both superconducting and normal) that focus, clean, and maintain the integrity of the beam are installed around the ring as well as a superconducting Radio Frequency (RF) cavity system that accelerates the beams to the nominal collision energy.

The LHC has four experiments that measure the products from the collisions produced at the Interaction Points (IPs). ATLAS and CMS are two large 'general purpose' detectors located on opposite sides of the LHC ring. CMS, located at IP5, is the instrument used for this analysis and thus will be the focus of discussion. It is described in detail in chapter 4. Two smaller experiments, focusing on more specific physics programs, are installed at the two IPs adjacent to ATLAS. ALICE, at IP2, focuses on heavy ion physics during special runs where the LHC collides lead or gold atoms instead of protons. LHCb, at IP8, searches for CP-violation and rare physics related to b-quarks. Illustrations of the

Figure 3.1: An aerial view of the LHC accelerator complex.

LCH experimental complex are shown in Figures 3.1 and 3.2.

In addition to the high center of mass collision energy, the LHC is designed to deliver as much luminosity as possible to the experiments. The luminosity (L) of an accelerator can be determined by:

$$L = \frac{N_b^2 n_b f_{rev} \gamma_r}{r\pi\epsilon_n \beta} F \tag{3.1}$$

where N_b is the number of particles per bunch, n_b is the number of bunches per beam, f_{rev} is the revolution frequency, γ_r is the relativistic form factor, ϵ_n is the normalized transverse beam emmittance, β is the beta function at the collision point and F is the geometric luminosity reduction factor due to parameters such as beam crossing angle, bunch length and transverse beam size.

The number of events, N_{event}, of a particular process expected for a given luminosity can be found by:

$$N_{event} = L\sigma_{event} \tag{3.2}$$

where σ_{event} is the cross section for the process in question. Since Eq. 3.1 expresses luminosity in units of $\frac{[Length]^2}{[Time]}$ and a cross section has units of $[Length]^2$, Eq. 3.2 gives the number of events per unit time for the process in question. While this is a useful quantity, it is more useful to predict the number of events for a specific process over a given dataset. Thus, the amount of data is nominally calculated integrated over time and is expressed in units of inverse cross section. In this way, it is easy to quote a number of predicted events

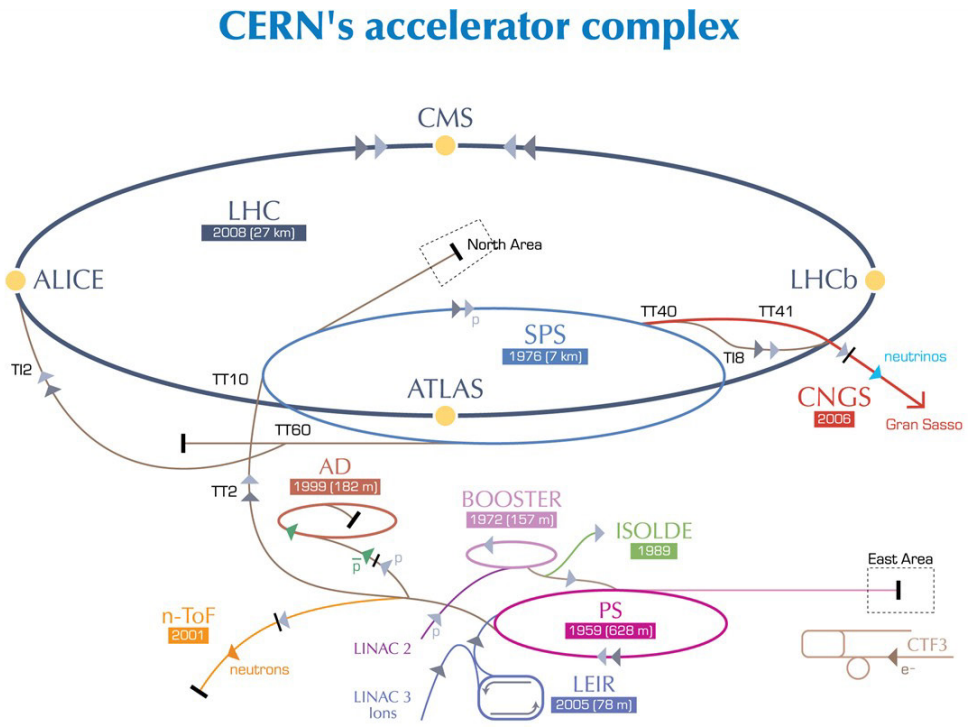

Figure 3.2: A schematic illustration of the LHC complex and injection chain[34].

just by multiplying the integrated luminosity, most often quoted in inverse femtobarns, by the relevant cross section and allows analyzers to predict how much data they will need to make a statistically significant observation.

The LHC has a peak design luminosity of $L = 10^{34}\text{cm}^{-2}\text{s}^{-1}$. However, the luminosity does not remain constant. The LHC goes through cycles called fills where protons are injected, and accelerated to the nominal beam energy. The luminosity peaks at the beginning of the fill and declines over time due to the collisions, beam cleaning, beam shaping, and interactions with other materials and remnants in the LHC beampipe. A nominal fill has an estimated lifetime of $\tau_l \approx 15$ hours, but this can vary considerably based on machine parameters.

Running at full design parameters, beams injected into the LHC have a bunch spacing ≈ 25 ns with $n_b = 2808$ bunches with each bunch containing $N_b \approx 10^{11}$ protons. Other nominal machine parameters for the 2015 data taking period, which is used for this analysis, can be found in Table 3.1.

Table 3.1: Nominal LHC beam parameters during the 2015 data taking period

Machine Parameter		**Nominal Value**
Energy	[GeV]	6500
Luminosity	[$cm^{-2}s^{-1}$]	10^{34}
Number of Bunches		2808
Bunch Spacing	[ns]	24.95
Protons per Bunch	[p/b]	1.15×10^{11}
Beam Current	[A]	0.58
Transverse Emmitance	[μm]	3.75
Longitudinal Emmitance	[eVs]	2.5
Bunch Length	[cm]	7.55

3.1 Interaction Points

As the beams circulate in the LHC, they are kept in separate beampipes to minimize the interaction of counter circulating bunches. Just before reaching an experimental Interaction Point (IP) the beams are deflected into the same beam pipe and into a trajectory to produce collisions in the center of the experiments. The crossing of the beams happens in either the horizontal or vertical plane depending on the IP: vertical at ATLAS and ALICE and horizontal at CMS and LHCb. Immediately before the beams collide, multiple magnets are used to adjust the beam profiles and focus them into a colliding trajectory at the nominal collision point. The beam optics for IP1 and IP5 where ATLAS and CMS are located respectively is shown in Figure 3.3.

At the IPs, the beams cross at a small angle because of the need to re-separate them on the other side of the interaction region for their continued circulation around the LHC. The effect of the crossing angle ($\sim 200 - 300\mu$rad) reduces the luminosity slightly but is a necessary feature of the circular collider design.

3.2 Injection Chain

The main LHC ring is not designed to accelerate proton beams all the way from zero to 7 TeV. Instead, it takes advantage of a complex of old accelerators that have been re-purposed to inject beams into the LHC with a significant amount of energy. This is illustrated in Figure 3.2. The beams are first accelerated to 50 MeV through a linear

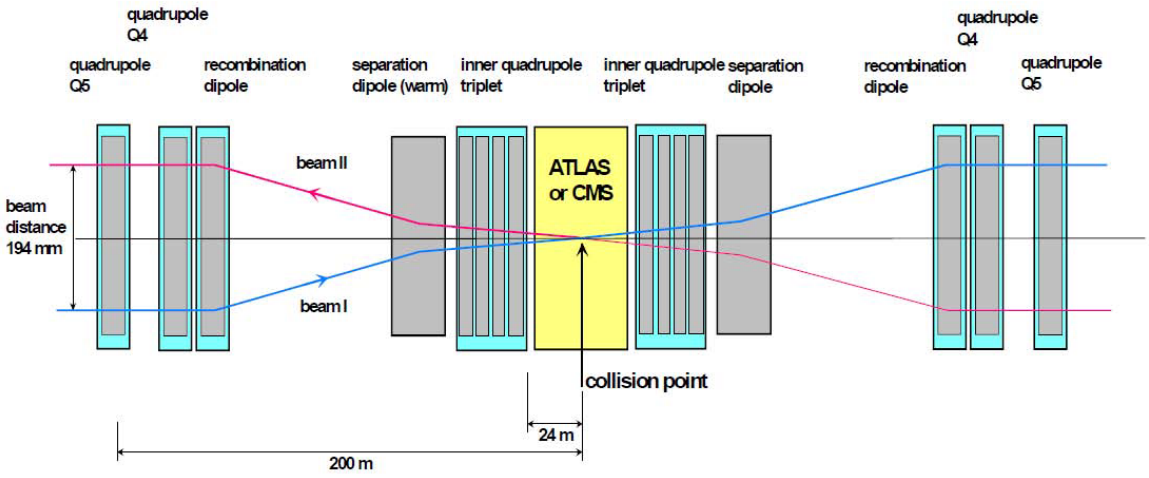

Figure 3.3: A schematic diagram of the beam optics around IP 1 and 5.

accelerator (Linac2) and then injected into the Proton Synchrotron Booster (PSB) where they achieve an energy of 1.4 GeV. From here they are injected into the Proton Synchrotron (PS) and accelerated to 28 GeV before being accelerated to 450 GeV in the Super Proton Synchrotron (SPS). At this point, the beams are ready for injection into the LHC where they will be accelerated to the nominal collision energy.

3.3 Magnetic Systems

As in any circular collider, the beams in the LHC must be bent around the ring such that they can make many orbits. In order to do this, a Lorentz force must be applied to the beam using a magnetic field. The magnetic field required to bend a beam appropriately in a circular collider can be expressed as:

$$B = \frac{p}{qR} \tag{3.3}$$

Where B is the required field, p is the beam momentum, q is the electric charge of the particle and R is the accelerator's radius. Using the nominal design values, the LHC requires an 8.33 T bending field for a beam energy of 7 TeV. This necessitates the use of superconducting magnets as it is much more difficult to generate a stable field of this strength with normal magnets. While Niobium-Titanium (NbTi) superconducting magnet coils have been used at previous accelerators, the LHC improves on the power of the coils by cooling them with supercritical helium at a temperatures below 2 K (compared to 4 K for standard liquid

Helium cooling), allowing for larger current in the coils and roughly a factor of two increase in the possible bending field strength.

The bending of the LHC beam is done in 110 m cells containing 6 bending dipoles. Possibly one of the more iconic images associated with the LHC, 1232 of the large, blue bending dipole cryostats are distributed around the ring. Figure 3.4 shows a cross section of one of the dipoles and Figure 3.5 shows the arrangement of the bending field lines resulting from the magnets.

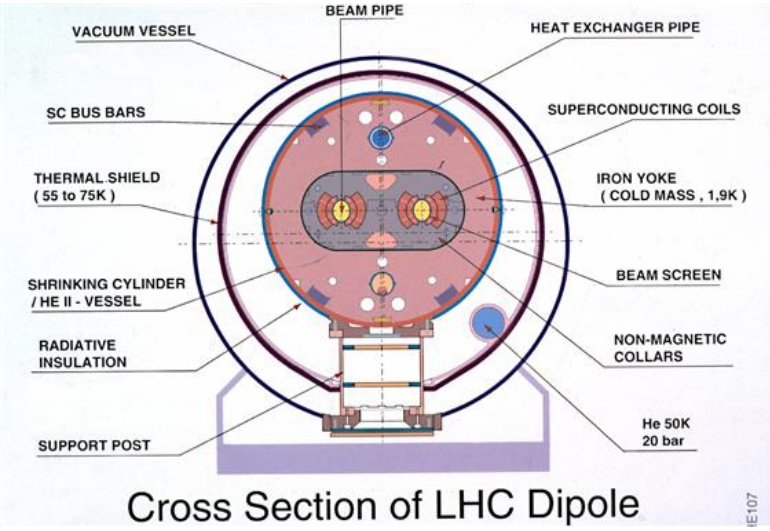

Figure 3.4: A schematic cross section of a LHC bending dipole[1].

In addition to the bending dipoles, the LHC makes use of a host of other multipole magnets (both normal and superconducting) to shape and clean the beam as it circulates.

3.4 RF Systems

Acceleration of beams in the LHC is done through the use of eight superconducting, Radio Frequency (RF) resonant cavities. Located around IP4, these cavities each generate a 2 MV acceleration voltage at full power, providing 16 MV of acceleration per beam. As the beam circulates, each pass through the RF system increases the beam energy by approximately 0.5 MeV; requiring about 20 minutes to bring the beam from the injection energy of 450 GeV to the nominal collision energy of 7 TeV.

The acceleration is done by driving the RF cavities at a resonant frequency that

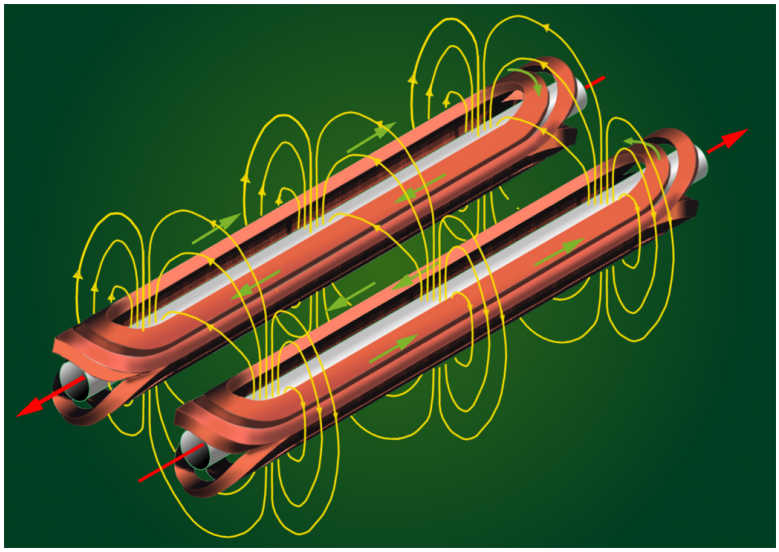

Figure 3.5: An artistic representation of the LHC bending dipole field lines around the beam pipe[23].

is tuned to the revolution frequency of the beams. If the beam and the cavity are in phase with each other, the beam will see no field as it will be aligned with the node of the cavity oscillation. If the bunch is slightly behind the node, either in phase or in frequency, it will see an accelerating force and be moved closer to the node. The opposite is true if the beam is ahead of the node. Figure 3.6 demonstrates this visually.

Using this self tuning behavior of the RF system, as the beam circulates, the driving frequency in the cavities can be slowly increased resulting in the beam gaining energy as it is forced to catch up as it is now lagging behind the new cavity resonance. At the nominal beam energy, any momentum losses incurred during an orbit of the machine will be compensated for in the RF system as long as that loss is not catastrophic enough to shift the beam significantly away from the cavity resonance. Additionally, if there is any significant momentum spread in the bunches themselves, they will be pushed down the gradient of the field strength and centered on the resonant node.

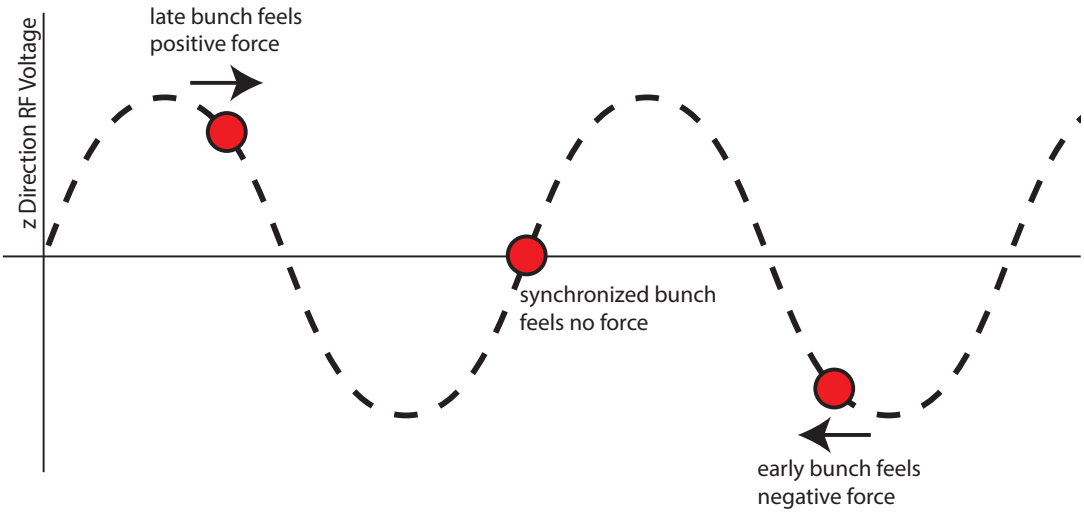

Figure 3.6: Artist's interpretation of RF acceleration synchronization.

Chapter 4

The CMS Detector

The Compact Muon Solenoid (CMS) detector is one of two general purpose detectors operating at the LHC and is designed to record collisions between protons or ions at the LHC collision energies. The LHC delivers collisions to the interaction points IPs at a nominal luminosity of 10^{34} cm^{-2} s^{-1} with a total proton-proton cross section of ≈ 100 mb. This results in an interaction rate of $\approx 10^9$ inelastic collisions per second. With 25 ns between bunch crossings, each event may have many hard scattering collisions resulting in a great many particles per bunch crossing. Being able to accurately handle the high rate and high occupancy environment, as well as certain benchmark physics goals, strongly informed the design of the detector.

The coordinate system in CMS is defined as a cylindrical geometry with the z-axis along the beamline and positive in the direction of the clockwise beam as viewed from above. The azimuthal angle, ϕ, is measured from the x axis, which points in the direction of the center of the LHC ring. The polar angle, θ, is measured in the rz plane but is more commonly expressed as the pseudo-rapidity $\eta = -\ln[\tan(\frac{\theta}{2})]$. Since the proton is a composite particle, the initial state longitudinal momentum can not be known. Thus many quantities under study are calculated in plane transverse to the beam line where the initial momentum is known to be very small on the scale of the resolution of CMS.

During the design phase of CMS, the collaboration established a set of requirements that would allow for an effective implementation of the CMS physics program. These requirements were[28]:

- Good muon identification and momentum resolution over a wide range of momenta in the region $|\eta| < 2.5$, good dimuon mass resolution ($\approx 1\%$ at

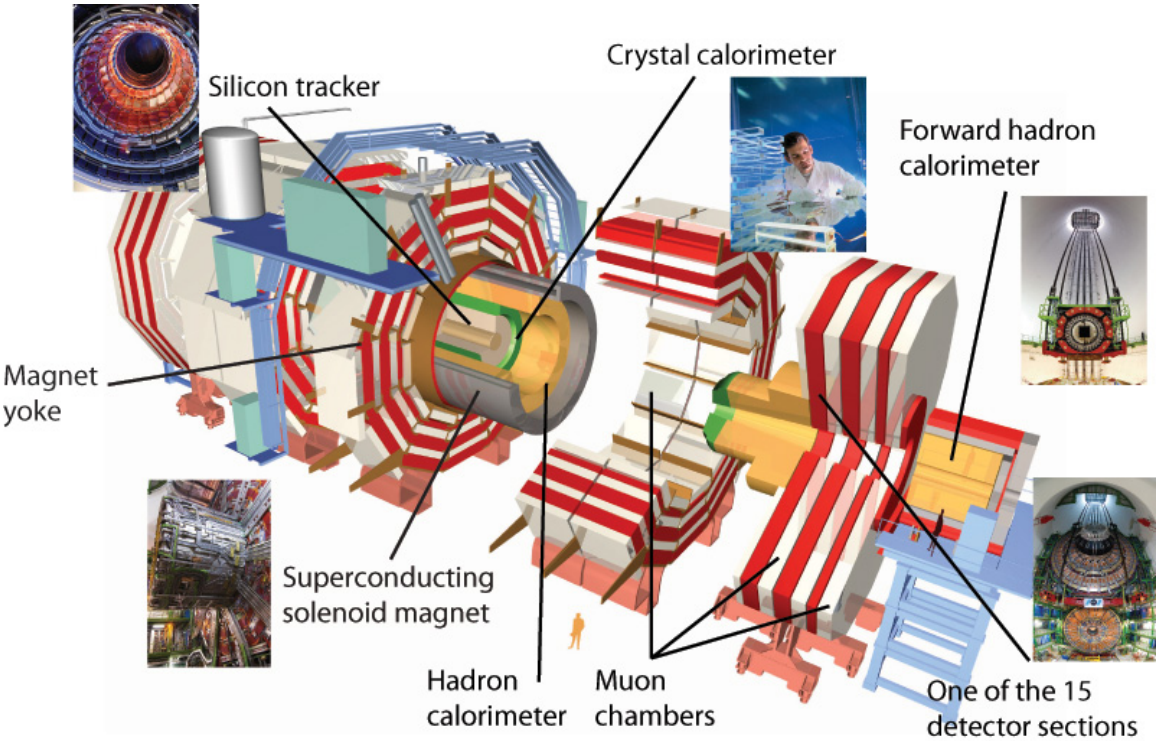

Figure 4.1: The Compact Muon Solenoid.

100 GeV), and the ability to determine unambiguously the charge of muons with $p < 1$TeV.

- Good charged particle momentum resolution and reconstruction efficiency in the inner tracker. Efficient triggering and offline tagging of τ's and b-jets, requiring pixel detectors close to the interaction region.
- Good electromagnetic energy resolution, good diphoton and dielectron mass resolution ($\approx 1\%$ at 100 GeV), wide geometric coverage ($|\eta| < 2.5$), measurement of the direction of photons and/or correct localization of the primary interaction vertex, π^0 rejection and efficient photon and lepton isolation at high luminosities.
- Good missing transverse energy, E_T^{miss}, and dijet mass resolution, requiring hadron calorimeters with a large hermetic geometric coverage ($|\eta| < 5$) and with fine lateral segmentation ($\Delta\eta \times \Delta\phi < 0.1 \times 0.1$).

To this end, CMS is constructed in a series of concentric sub-detectors arranged parallel to the LHC beam line. Each subsystem is built with a central barrel section and endcaps that terminate the barrel and extend coverage toward the beam pipe. The main subsystems are:

- Layers of pixel detectors positioned closest to the interaction point to provide good tracking and vertex resolution.
- Layers of high granularity silicon strip detectors to cope with a high multiplicity environment.
- A two component calorimetry system to measure charged particle and jet energies.
- A muon tracking system outside of the central solenoid to provide muon identification and improve muon momentum measurement.

These subsystems work in concert to identify and reconstruct particles created in the LHC collisions, providing a view of the final state of the whole event. Charged particles are bent by Lorentz forces in the magnetic field while leaving tracks in the inner tracker before depositing their energy in the calorimeters. Neutral hadrons and photons deposit energy in the calorimeters but are not deflected by the magnetic field nor do they leave tracks in the inner tracker. Muons are highly penetrating and pass through the inner detector and are then measured in the Muon tracking system outside of the solenoidal volume. All these systems are held by iron flux return yolks that both provide for mechanical rigidity of the detector as well as shape the magnetic flux lines as they circle from one side of the solenoid back to the other.

The particulars of the design decisions for each subdetector are outlined in their respective following sections.

4.1 Superconducting Solenoidal Magnetic Field

Central to the design of CMS is the central superconducting solenoid. The choice of magnetic field configuration for CMS was motivated by above requirements on performance of the muon system. Requiring unambiguous determination of the charge of a 1 TeV muon sets the required bending power across the detector by the magnetic field. Thus, CMS was designed with a large superconducting solenoid at its core. The magnet coil has 2168 turns and is $\approx$ 13 meters long with a $\approx$ 6 meter inner bore. The magnet nominally carries 19.9 kA of current, stores 2.7 GJ of energy and operates at a central field strength 3.8 Tesla.

The exterior field is returned to the coil through iron flux return yolks that also provide structural rigidity for CMS. The return field is strong enough to saturate 1.5 m of

iron but the return yolks are sufficiently large to contain the majority of the return flux, leaving the area occupied by the muon system in a minimal field. Detailed surveys and models of the CMS magnetic field are imperative to the understanding of its operation.

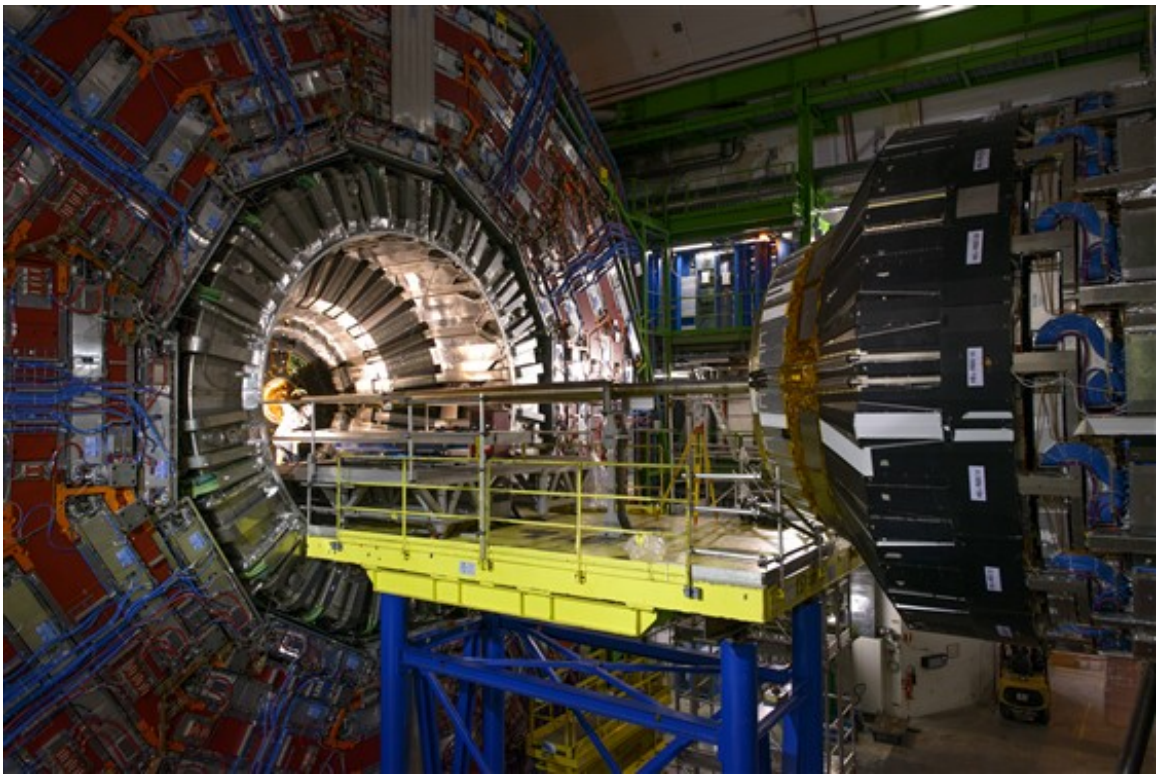

Figure 4.2: The CMS Barrel and Endcap nosecone[16].

4.2 Inner Tracker

The Inner Tracker is composed of two subsystems: the Pixel Tracker and the Strip Tracker. Working together they are responsible for measuring the position and momentum of charged particles resulting from collisions. Many considerations were taking during the tracker design phase. High constraints on the measurement of both track momentum and vertex position are required while keeping the materials budget as low as possible. Any significant showering or multiple scattering in the tracker would obfuscate measurements both in the tracker itself and in the caolrimeters.

4.2.1 Pixel Tracker

The Pixel Tracker is located in the innermost region of CMS, closest to the interaction point. It is composed of four layers of silicon pixel modules. These modules measure the crossing point of particles that traverse the active region of the pixels. The pixel modules are overlapped such that the system provides total coverage in the region $|\eta| < 2.5$. The position of each module is precisely measured such that a 2-D hit can be translated in to a 3-D position measurement of the particle's trajectory. The system is layered in 4 concentric shells in order to provide accurate measurement of the bending of the track in the central magnetic field.

Semiconductor junctions make up the active material in both the Pixel Tracker and the Strip Tracker. In the Pixel Tracker, a p-n junction with n-+ pixels implanted on the other side of the n-type bulk act as the sensing element. The p-n junction is reversed biased resulting in a depletion band of a known depth for a given bias voltage. When an ionizing particle crosses the sensor, it frees electrons and holes proportional to the energy of the incident particle. The electrons then drift to the n-+ implants while the holes drift to the p-type side of the junction allowing a signal readout of that current. The depth of the substrate is determined both by the CMS material budget and the required depletion depth for reasonable detector performance.

Performance constraints on the resolution of track vertexing close to the interaction point, IP, require a resolution of pixel hits of $15\mu m$ in the layer closest to the IP and $40\mu m$ at outside of the tracker. Taking advantage of the high magnetic field in the inner regions of CMS, the size of a sensing pixel has been specified as being square with $150\mu m$ per side. While this individual element is much larger than the required resolution, in the barrel region a Lorentz angle of 32° on the drifting electrons due to the 3.8 T magnetic field causes significant charge sharing between adjacent pixels. Based on the proportions of charge shared, a tighter measurement on the hit position is possible even with a relatively large sensing element.

The endcap pixels, however, do not benefit from this in a nominal geometry where the endcap discs are perpendicular to the beamline, as the magnetic field lines are parallel to the drift trajectories of the freed electrons. To compensate for this, the pixel modules in the endcaps are collected into 'blades' and then rotated around their central radial axis by 20°. This causes charge sharing between pixels and allows for the required resolution demanded by the CMS performance goals.

Being able to rely on a larger pixel allows for not only an easier logistical application of the pixel modules themselves, but for more room to create a more robust electronic readout system.

One of the most important roles of the Pixel Tracker is to aid in the reconstruction of track vertices in the interaction region. By providing several high resolution 3-D tracking hits close to the interaction point, the pixel tracker enables the CMS software to distinguish tracks coming from a primary vertex (PV) that activated the Trigger from other vertices from pileup. This allows us to isolate interesting physics objects from the chaos of the high particle multiplicity created by the LHC collisions and distinguish processes of interest from the event background.

Another function of the vertexing is in the reconstruction of secondary vertices from the decay of long lived particles such as b-hadrons. Due to the decay lifetime of these particles, they will create tracks that originate away from the IP and proper identification of these secondary decay vertices allows CMS to tag, for example, a jet as having come from a b-hadron. This functionality is of particular import to any analysis that makes use of heavy flavor information or is searching for long lived BSM objects.

4.2.2 Strip Tracker

The second part of the CMS Tracking System is the Silicon Strip Tracker, often referred to as the SST or just the Strip Tracker. The Strip Tracker, like the Pixel Tracker, also utilizes silicon ionization detecting elements. Where the pixel tracker is essential to associate tracks with vertices, the strip tracker's primary purpose is to measure, with high precision, the momentum of tracks.

The geometry and technical details of how the Strip Tracker is constructed reflects this alternate purpose. In order to measure the transverse momentum of charged tracks, the Silicon tracker must measure the bending radius of those tracks as they pass through the 4T central magnetic field. The long lever arm across the radius of the Strip Tracker combined with multiple measurements of the track's position allow for resolutions in line with the Detector Design Goals.

The Strip tracker is composed of 4 sections. Designated the Tracker Inner Barrel (TIB), Tracker Outer Barrel (TOB), Tracker Inner Endcap (TIC), and Tracker Outer Endcap (TOC), these four sections are made up of silicon microstrip modules. Each module contains an active region with p-type strips implanted into an n-type bulk. While this

differs from the sensor type used in the Pixel Tracker, the operation principle is the same.

In the barrel sections, TIB and TOB, the sensor modules have a rectangular active area and strips are arranged parallel to the beamline to provide measurement in the r-ϕ plane. The TIB and TOB are then further separated into two subsections with the sections labeled with a 1 closest to the IP. The pitch and number of the strips changes from layer to layer to reflect the occupancy needs as the distance from the IP increases as well as to tune the number of strips on a module to an electronics modularity of 256. Modules are arranged in an overlapping fashion to provide complete coverage with some layers being composed of double layer back-to-back modules with an offset of 100 mrad between the two sides.

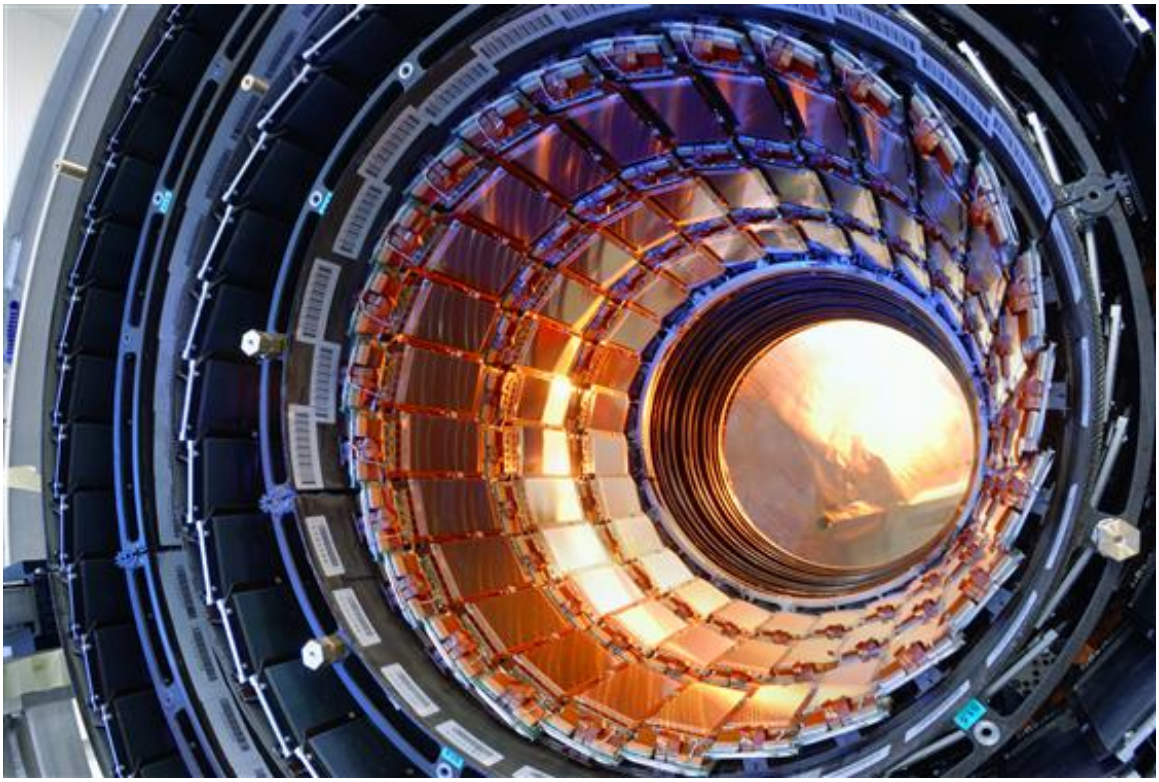

Figure 4.3: The Silicon Strip Tracker[15].

Just as with the Pixel Tracker, the high multiplicity environment is a primary driving factor in determining the granularity in the Strip Tracker. As an additional complicating factor, at the radius of the Strip Tracker, the occupancy of low p_T tracks from minimum bias events that are insufficiently energetic to leave the tracker is high, increasing the channel occupancy significantly as these trapped tracks circle in the magnetic field.

Thus the Strip tracker is highly segmented, resulting in 9.6 million channels over an active area of 198 m^2 of silicon; which is the average floor space for an apartment in the USA.

4.3 Calorimetry

For a complete Lorentz invariant measurement of collisions inside the LHC, one must reconstruct the four-vector of all particles resulting for the collision. The tracking systems in CMS are responsible for the measurement of the momentum of these particles, but to gain the complete picture their energy must also be measured.

The energy measurement, or calorimetery, of particles in CMS is divided up into two complimentary subsystems: The Electromagnetic Calorimeter (ECAL) and the Hadron Calorimeter (HCAL). These detector systems measure the energy of different types of particles as they leave the central tracking volume. To first order, the ECAL measures the energy of electromagnetically interacting particles while the HCAL measures the energy of strongly interacting particles. However, several complicating factors require a more complete view of the total calorimetery system for the proper measurement of particle energies. These issues will be addressed in Chapter 6 during the discussion of the reconstruction of physics objects. In the following sections, technical details on the design, construction, and operation of the two calorimetery systems is presented.

4.3.1 Electromagnetic Calorimeter

The Electromagnetic Calorimeter, ECAL, is tasked with measuring the energy of electrically charged particles resulting from the LHC collisions. The ECAL is composed of nearly 72,000 Lead-Tungstate ($PbWO_4$), scintillation crystals arranged into barrel (EB) and endcap (EE) regions. In the EB, the crystals are 23 cm in length and vary in cross-sectional area depending on their position in η. In the EE, the crystals are slightly shorter at 22 cm but have uniform a cross-section across all of the crystals in the endcap.

Lead-Tungstate was chosen as the crystal material based on properties that would enable the Higgs to gamma gamma search in the CMS physics program. The time scale for the Lead-Tungstate scintillation is approximately 80% on the order of 25 ns allowing for proper interface with the LHC bunch crossing timing. The crystals also have a naturally short radiation length of 0.89 cm making them a good choice for a compact calorimeter.

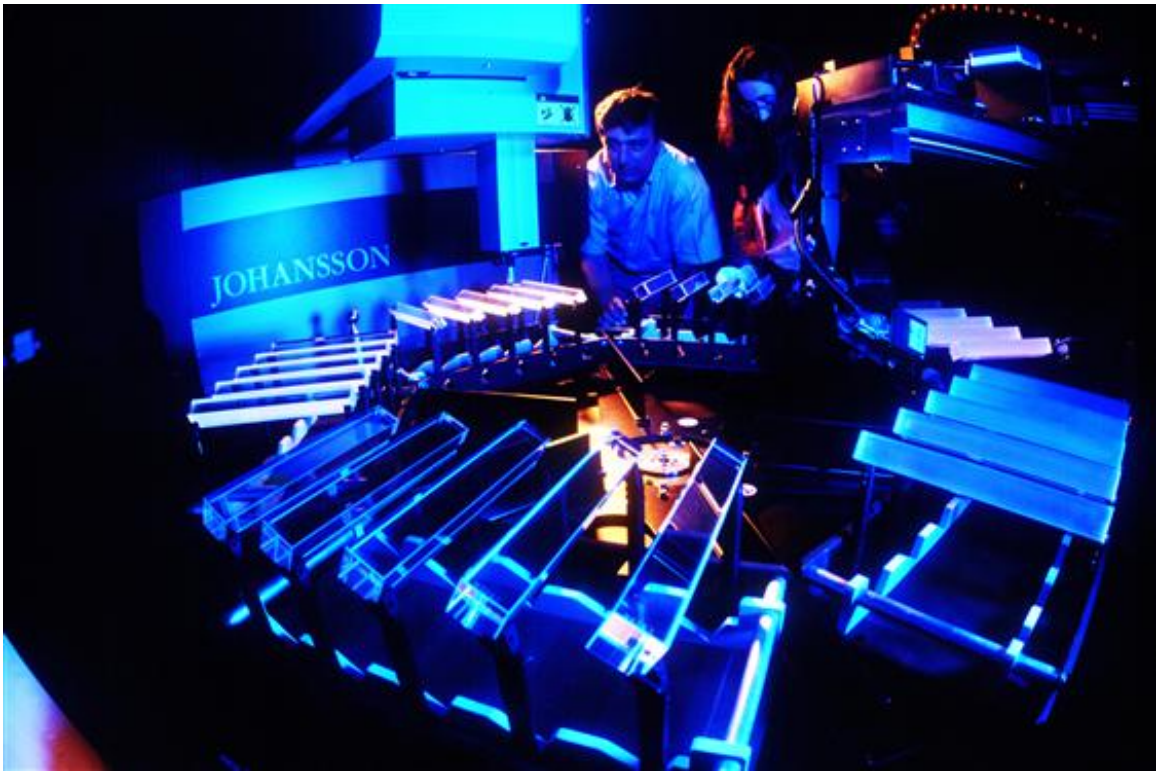

Figure 4.4: Lead-Tungstate crystals used in the CMS ECAL[39].

Approximately 25 radiation lengths in each crystal is sufficient to capture the majority of electromagnetic energy as particles traverse the ECAL. This combined with a small Moliere radius of 2.2 cm provides a resolution on the energy of electromagnetic showers of better than 1% for typical electron energies, which is in line with the CMS design goals.

4.3.2 Hadron Calorimeter

The HCAL has the job of measuring the energy of strongly interacting, electrically neutral particles. This is accomplished by interleaving dense absorber material with a short nuclear interaction length with scintillators. The absorber material induces hadronic showering from incident particles and then the ionization energy of those showers is collected as light in the scintillators. Based on calibration data, the energy of the incident particle can then be inferred. This design differs from the ECAL design wherein the $PbWO_4$ crystals act to both induce and measure the electromagnetic showers.

The HCAL is subdivided into 4 regions, barrel (HB) endcap (HE) outer (HO) and forward (HF). As this analysis only pertains to particles in the barrel and endcap regions,

discussion of the HF design and operation will not be included.

Due to the high magnetic field present at CMS, materials used in the construction of the HCAL must be necessarily non-magnetic. Additionally, space constraints inside the CMS magnet coil necessitate a compact design of the HB and HE systems. The absorber must therefore have a high density to increase the number of nuclear interaction lengths across the available volume of the detector. Brass was chosen as a suitable absorber material being very dense, non-magnetic, and readily available for low cost.

In the HB, 16 layers of scintillators interleaved with brass are arranged into 36 (18 on each side of the IP) wedges each covering an azumuthal range of $\Delta\phi = 20°$. These wedges are segmented in the z direction creating stacks as seen in Figure 4.5. This results in a thickness of 5.8 nuclear interaction lengths at $\eta = 0$ and 10 interaction lengths at $|\eta| = 1.2$ Energy deposited in each stack is added in order to make the measurement of a shower's energy.

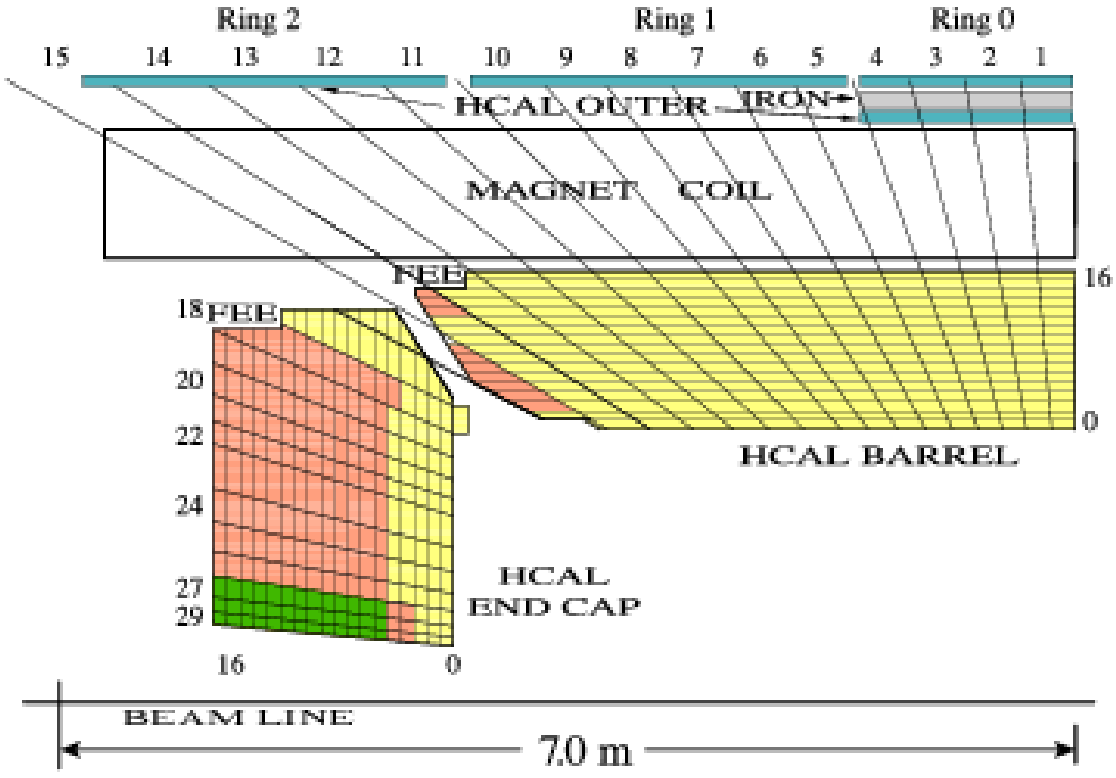

Figure 4.5: A schematic diagram of the CMS HCAL[24].

The HE is built in a similar fashion but for a different geometry conducive to the endcap. Brass disks, instead of rectangular plates, make up the absorber material and scintilators segmented in ϕ and r provide the active material to make up the stacks. The HE is also designed in 36 wedges covering the same ϕ ranges and their counterparts in the HB.

In the crossover region between the HB and HE, the adding of layers is complicated slightly by the geometry of the crossover. The gap between the HB and HE, while not projective to the IP, makes collecting segments into non-uniform stacks advantageous to ensure energy collected is associated with the proper shower, especially in a high multiplicity environment.

The final part of the HCAL that will be discussed here is the HO. The HO is an extra layer of scintilator plates placed outside of the CMS Magnet Coil. Recall that in the barrel region, the constrained volume resulted in a reduced the number of nuclear interaction lengths especially at low η. This allows for the possibility that showers will not terminate in the HCAL and will punch through into the outer regions of CMS. The HO attempts to catch the tail of these showers and essentially uses the CMS Magnet Coil as its absorber layer. About 5% of hadrons with energies above 100 GeV will deposit energy in the HO.

4.4 Muon System

The Muon system contains three different types of detectors. In the barrel, Drift Tubes (DT) provide tracking of muons that have penetrated into the outer layers of the barrel while in the endcaps, Cathode Strip Chambers (CSC) provide an analogous function. Both of these systems are paired with Resistive Plate Chambers (RPC) which provide high precision timing data on muons for the CMS Trigger system.

At the typical energies particles are produced at in CMS, muons are minimum ionizing particles and will thus penetrate through the inner layers of the detector with a minimal energy loss. Figure 4.6, shows the stopping power (dE/dx) of a muon passing through matter as a function of the muons momentum. For this energy scale, all other particle species expected in LHC collisions (excepting neutrinos) either fall in the multiple scattering or radiation dominated regions of the dE/dx curve. This, combined with the usefulness of muons in realizing the CMS physics program, makes useful having a separate

detector subsystem to identify and measure muons with a high precision. Indeed, muons are a central part of the namesake of CMS.

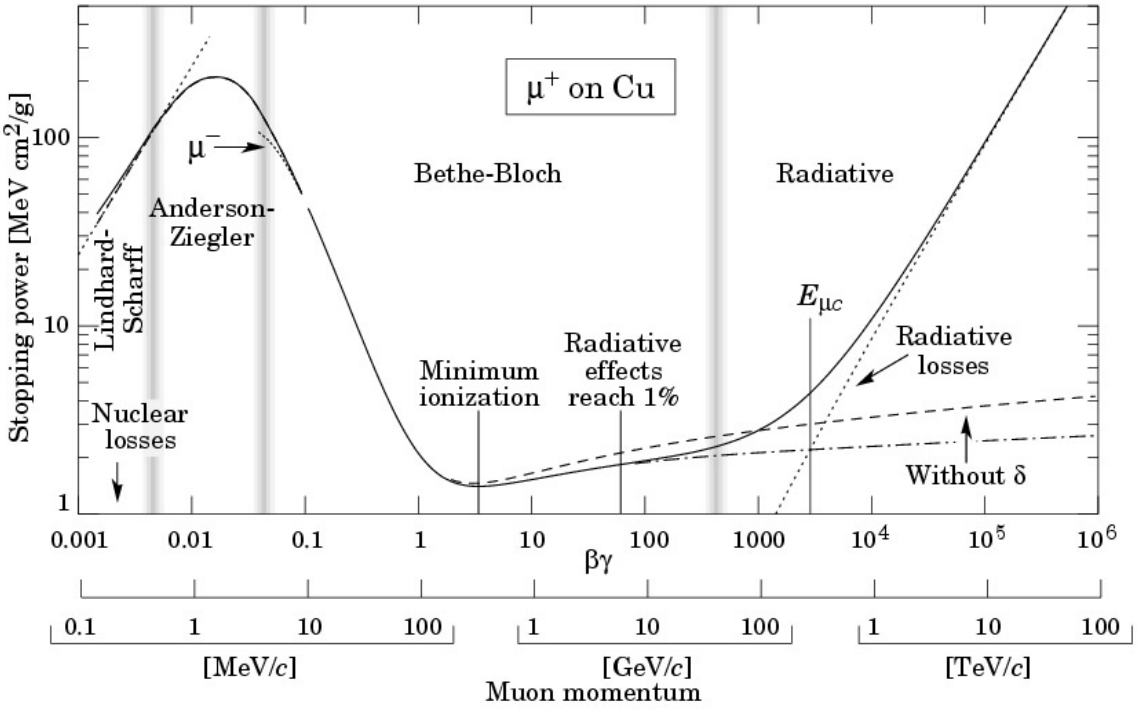

Figure 4.6: Energy deposition in matter for a muon as a function of momentum[44].

All of the muon system detectors are located outside the central magnet volume (with the possible expection of the ME1/1 layer in the endcap) and are thus intervened with the iron flux return yolks as seen in Figure 4.1.

4.4.1 Barrel Muon Drift Tubes

The Drift Tubes (DT) are responsible for measuring the position and momentum of muons in the barrel region of CMS. The basic sensing element of the DTs is a single rectangular drift tube with a single central wire. Similar to the CSCs, the DTs operate by collecting the charge deposited by ionizing the gas medium present in the tube. The wire is kept at voltage providing an electric field inside the tube and causing the liberated electrons to drift toward the wire. The electrons fall onto the wire and this is read out by the front end electronics as a current.

The DTs are collected into set of drift cells called Super Layers, SLs. Each SL is

composed of three layers of DT cells each staggered by a half cell. Three SLs are collected into a single DT chamber with the middle SL rotated by 90° with respect to the other two layers in the chamber.

Each drift cell cross section is 40 mm by 13 mm and is 2.4 m long, corresponding to a maximum drift time of 380 ns when filled with an 85% Ar + 15% CO_2 gas mixture. The choice of the rectangular geometry for the basic gas cell was made in order to effectively shape the electric field inside the cell to allow for measurement of the timing of the hit in the cell. This can be done through simple mean timer circuits leading to a time resolution of a few nano-seconds and stand-alone bunch crossing identification. Electrodes on two sides of the drift cell provide this field shaping in concert with the voltage on the wire. Additionally, the particular dimensions of the drift cells keep the overall number of electronic channels from becoming unmanageable while still fulfilling the CMS design goals with respect to muon measurement.

4.4.2 Endcap Muon Cathode Strip Chambers

The Cathode Strip Chambers (CSC) are one of the two subsystems that make up the Endcap Muon (EMU) system. 468 trapezoidal chambers make up four layers with each layer being made up of multiple rings. They are oriented on the endcaps with each chamber covering an interval of angle within its particular ring. As the circumference of each ring scales with the distance from the beampipe, the chambers size changes, the further the ring is from it. There are 5 types of chambers denoted as ME1/1 ME1/2, ME1/3, ME234/1, and ME234/2. While these 5 chamber types differ in size, number of readout channels, and resolution requirements; they are all based on the same design.

Based on Multi-wire Proportional Counter technology, each chamber has 6 gas gaps to multiply measure muon trajectories in each chamber. Each gap consists of two copper planes with anode wires strung between them. When a particle traverses the gap, it deposits energy by ionizing gas in the gap. The electrons, freed by the ionization, drift toward the wires as they fall down the electric potential created by the 3.8 kV voltage kept on the wires. As the electrons fall down the potential well, they increase in energy until they are sufficiently energetic to ionize other gas atoms on their path. This causes a cascade effect that amplifies the current read out by the anode electronics.

On most chambers (ME1/1 chambers differ slightly due to a significantly different drift angle caused by the flux return in the region they occupy), the wires are aligned

normal to the chamber's long axis and provide a one dimensional measurement of muon trajectories in the r-direction. To compliment this measurement, one of the copper planes that sandwich the gap has strips milled into it. As the strips are essentially large planes of conductor, the image charge of the electron cascade can be measured on the strips. Thus, the strips are milled perpendicular (mostly) to the wires. The milling of the strips actually maintains a constant angle of each strip as it extends through the chamber. In this way, when the chambers are oriented on the endcap, each gap provides a measurement of muon trajectory in the $r-\phi$ plane. The position of the chamber and the gap inside that chamber provides the z-coordinate measurement and allows for a high precision measurement of the best fit track through all the hit in the chambers.

The CSC layers are held between Endcap Flux Return Yolks (YE) much in the same way the Barrel Muon system is. While the YB are open ended cylenders the YE are large iron disks the full radius of CMS. The saturation of the YE causes the return field to point largely in the r-direction inside the YE disks and like in the YB, to be minimal over chambers. The exception to this field environment is in the ME1/1 chambers.

The ME1/1 chambers are situated in the nosecone of the endcap. This support structure is on the inside of the YE1 disks and is inserted into the end of the CMS magnet volume. This means that the electrons freed in the ME1/1 chambers, just as in other parts of CMS, see a Lorentz force as they drift toward the wires. For this reason, the wires in the ME1/1 chambers are fixed at an angle to the strips to account for this Lorentz drift.

4.4.3 Resistive Plate Chamber

The Resistive Plate Chambers (RPC) are gaseous parallel plate detectors that work in tandem with both the DTs and the CSCs. Also gaseous ionization detectors, the RPCs are constructed of two gas gaps each ≈ 2 mm across. One side of each gap has strips of electrodes used for collecting the liberated charge in the gap and each gap is oriented with its strips normal to the other.

The spatial resolution is considerably poorer that that of the other detectors in the muon system. However, RPCs have a timing resolution comparable to that of scintilators and thus provide excellent timing information at high rate. This is paramount to the operation of the Trigger System when muons are involved and is discussed below.

4.5 Trigger

During nominal running, the LHC bunch crossings produce on average 15 proton-proton interactions per bunch crossing every 25 ns. This event rate is far above the capability of the computing and reconstruction systems in CMS to handle. Thus, a trigger system to effectively and reliable filter out uninteresting events from the data is required to moderate the total data output of CMS.

The CMS trigger system is separated into two subsystems, the Level 1 trigger and the High Level trigger, that work in concert to provide filtered data to the analyzers

4.5.1 Level 1 Trigger

The Level 1, L1, trigger system is the first level of filtering on the CMS data. The necessity of making trigger decisions very quickly at the L1 level means that L1 trigger decisions are made on primitive variables output from dedicated trigger electronics in each subsystem. These primitives, constructed from things like coincident hits in trackers and columns in the calorimeters, provide a core determination of the presence of interesting physics objects. They are then pattern matched to provide preliminary muon, electron, and jet candidates that the L1 trigger system can use in order to decide whether or not to pass the event to the High Level Trigger.

4.5.2 High Level Trigger

The High Level trigger, HLT, is the second filtering decision made on CMS data. After an event passes a L1 trigger, it is sent to the computing farm where it goes through standard reconstruction and isolation algorithms and outputs collections of physics objects as described in Chapter 6.

The HLT then sorts and filters events based on criteria such as, for example, the presence of a muon with transverse momentum (p_T) $\geq$ 17 GeV and an additional muon with $p_T \geq 8$ Gev with appropriate isolation requirements. Many trigger 'paths' such as this are collected into the CMS HLT menu. Analyzers will select what trigger paths are relevant for their signal and use those collections of events for their measurements.

The CMS computing farm is limited in the amount of data it can process in a given time. The throughput from the L1 trigger is much larger than the maximal output of the HLT and thus, entries in the HLT trigger menu must all compete for bandwith. This

results in the thresholds for various trigger paths being tuned so that their rate fits within their assigned bandwidth. Bandwidth is assigned by the CMS Trigger group based on the number and physics priority of analyses desiring use of the path.

Chapter 5

Data and Simulation

5.1 Data Samples

The data used in this analysis are drawn from the full 2015 DoubleMuon, MuonEgG and DoubleEG. This corresponds to an integrated luminosity of $\approx 2.6\text{fb}^{-1}$. All data have been processed using the 76X version of the CMSSW software into version 2 of the CMS miniAOD data format. A complete list of the specifications of the data samples is provided in Tables 5.1 to 5.3. Valid runs in the data were selected using the SILVER JSON as this analysis does not consider the forward region.

5.2 Simulation Samples

Simulation samples used in this analysis were produced as part of the CMS Run II Fall 2015 production campaign. All samples have been processed using the 76X version of the CMSSW software. In order to scale the simulation samples to the data, simulated events

Dataset	Int. Lumi (pb^{-1})
/DoubleMuon/Run2015C_25ns-16Dec2015-v1/MINIAOD	17.2
/DoubleMuon/Run2015D-16Dec2015-v1/MINIAOD	2612.1
Total	2629.3

Table 5.1: Dataset name and integrated luminosity for the data samples used for the $\mu\mu$ channel.

Dataset	Int. Lumi (pb^{-1})
/MuonEG/Run2015C_25ns-16Dec2015-v1/MINIAOD	17.2
/MuonEG/Run2015D-Run2015D-16Dec2015-v1/MINIAOD	2612.3
Total	2629.5

Table 5.2: Dataset name and integrated luminosity for the data samples used for the $e\mu$ channel.

Dataset	Int. Lumi (pb^{-1})
/DoubleEG/Run2015C_25ns-16Dec2015-v1/MINIAOD	17.2
/DoubleEG/Run2015D-16Dec2015-v2/MINIAOD	2610.4
Total	2627.6

Table 5.3: Dataset name and integrated luminosity for the data samples used for the ee channel.

must be weighted to their theoretical cross section using Eq. 5.1, where L_{eff} is determined on a sample by sample basis from Eq. 5.2 for the appropriate sample size and cross section as seen in Table 5.4.

$$W_{event} = \frac{L_{Data}}{L_{eff}} \tag{5.1}$$

$$N_{MC} = L_{eff}\sigma_{MC} \tag{5.2}$$

The aMC@NLO generator utilizes negatively weighted events in order to cancel out events relating to higher order diagrams[8]. This results in the effective statistics of any sample created using aMC@NLO being reduced in a manner consistent with Eq. 5.3. Effective statistics of samples utilizing aMC@NLO are documented in the right most column of Table 5.4 where applicable and such samples are normalized using the number of effective events, N_{eff}, rather than the number of total events, N_{tot}.

$$N_{eff} = N_{tot} - 2N_{neg} = N_{pos} - N_{neg} \tag{5.3}$$

Since the $t\bar{t}t\bar{t}$ signal is so small, one must consider contributions from other subleading top quark backgrounds that could mimic $t\bar{t}t\bar{t}$ production. For this analysis, the contributions from $t\bar{t}$H, $t\bar{t}$Z, and $t\bar{t}$W are considered. After passing the baseline selection,

the contribution from these sources is very small (< 10 events across all final states). These have been included by merging them with the $t\bar{t}$ simulations to produce a single $t\bar{t}$ +X sample, which will be compared to the data.

A list of simulation samples used in studies of sources of systematic uncertainty are give in Table 5.5.

5.2.1 Pile-up re-weighting procedure

In order to generate enough data to be able to examine rare and exotic processes, the LHC must deliver a high instantaneous luminosity in the form of highly populated bunches in the beams. This leads to the possiblity of multiple hard scattering events in every bunch crossing. This phenomenon can be quantified in terms of the number of primary vertices present in each event and is dubbed as 'pile-up.'

To correct for differences in the pile-up distributions of data and simulation, an event-by-event re-weighting is applied to the simulation. The weight for each event is calculated using the official CMS prescription for 2015 data[27] with a minimum bias cross section of 69 mb. The distributions for the number of primary vertices for data and simulation events which pass the different baseline selections detailed in Chapter 7.2, after the re-weighting procedure has been applied, can be seen in Fig. 5.1. The distributions are in good agreement, which demonstrates the validity of the re-weighting procedure.

Dataset	Eff. Events	σ (pb^{-1})
/TTTT_TuneCUETP8M1_13TeV-amcatnlo-pythia8/ RunIIFall15MiniAODv2-PU25nsData2015v1_76X_mcRun2_asymptotic_v12_ext1-v1	393K	0.0091
/TTTo2L2Nu_13TeV-powheg/ RunIIFall15MiniAODv2-PU25nsData2015v1_76X_mcRun2_asymptotic_v12_ext1-v1	107M	831.7
/ST_tW_antitop_5f_inclusiveDecays_13TeV-powheg-pythia8_TuneCUETP8M1/ RunIIFall15MiniAODv2-PU25nsData2015v1_76X_mcRun2_asymptotic_v12	1M	71.7
/ST_tW_top_5f_inclusiveDecays_13TeV-powheg-pythia8_TuneCUETP8M1/ RunIIFall15MiniAODv2-PU25nsData2015v1_76X_mcRun2_asymptotic_v12	1M	71.7
/DYJetsToLL_M-50_TuneCUETP8M1_13TeV-madgraphMLM-pythia8/ RunIIFall15MiniAODv2-PU25nsData2015v1_76X_mcRun2_asymptotic_v12_ext1-v1	250M	6025.2
/TTZToLLNuNu_M-10_TuneCUETP8M1_13TeV-amcatnlo-pythia8/ RunIIFall15MiniAODv2-PU25nsData2015v1_76X_mcRun2_asymptotic_v12-v1	400K	0.293
/TTWJetsToLNu_TuneCUETP8M1_13TeV-amcatnloFXFX-madspin-pythia8/ RunIIFall15MiniAODv2-PU25nsData2015v1_76X_mcRun2_asymptotic_v12-v1	250K	0.204
/ttHJetTobb_M125_13TeV_amcatnloFXFX_madspin_pythia8/ RunIIFall15MiniAODv2-PU25nsData2015v1_76X_mcRun2_asymptotic_v12-v1	1.6M	0.293
/TTJets_SingleLeptFromTbar_TuneCUETP8M1_13TeV-madgraphMLM-pythia8/ RunIIFall15MiniAODv2-PU25nsData2015v1_76X_mcRun2_asymptotic_v12_ext1-v1	50M	831
/TTJets_SingleLeptFromT_TuneCUETP8M1_13TeV-madgraphMLM-pythia8/ RunIIFall15MiniAODv2-PU25nsData2015v1_76X_mcRun2_asymptotic_v12_ext1-v2	50M	831

Table 5.4: Dataset name, total number of events, and cross section for the simulated samples. All samples are generated in version 2 of the CMS miniAOD data format.

Dataset	Events	Generator Order	σ (pb^{-1})
/TTTo2L2Nu_13TeV-powheg-ScaleUp/ RunIIFall15MiniAODv2-PU25nsData2015v1_76X_mcRun2_asymptotic_v12-v1	30M	NLO	831
/TTTo2L2Nu_13TeV-powheg-ScaleDown/ RunIIFall15MiniAODv2-PU25nsData2015v1_76X_mcRun2_asymptotic_v12-v1	30M	NLO	831
/TTJets_DiLept_TuneCUETP8M1_13TeV-madgraphMLM-pythia8/ RunIIFall15MiniAODv2-PU25nsData2015v1_76X_mcRun2_asymptotic_v12-ext1-v1	25M	NLO	831

Table 5.5: Dataset name and total number of events for the simulated systematic samples. All samples are generated in version 2 of the CMS miniAOD data format.

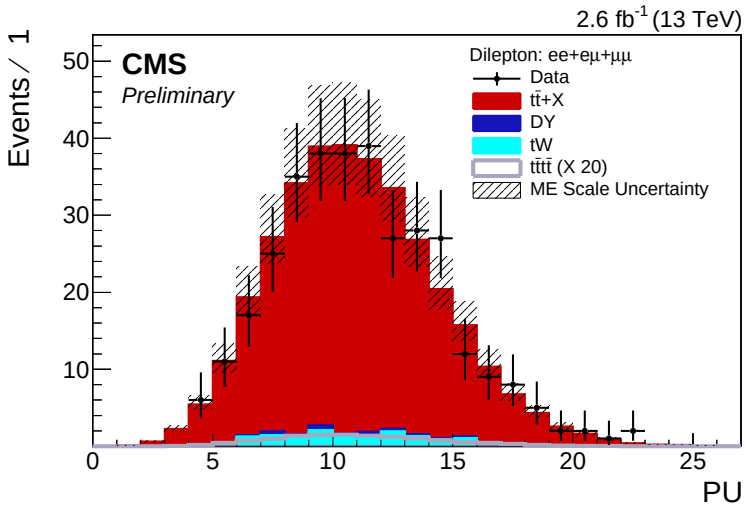

Figure 5.1: The number of primary vertices across all channels for data and simulation after re-weighting.

Chapter 6

Object Reconstruction and Identification

The object definitions described here are based on the standard 2015 recommendations for dilepton + jets decay channels provided by the CMS TOP Physics Analysis Group (PAG)[38]. The particle flow, PF, algorithm[29] is used to reconstruct the final state objects in each event. Events are required to contain at least one primary vertex as determined by PF. Reconstructed final state objects are placed in collections according the the version 2 CMS miniAOD[26] format definitions. The following physics objects are constructed for analysis.

6.1 Jets

Jets are reconstructed with the $anti - k_T$ clustering algorithm with a cone radius of $R = 0.4$ ($\Delta R = \sqrt{\Delta\theta^2 + \Delta\phi^2}$) from the set of PF candidates present in the event once charged hadron PF candidates from PU are removed[19, 20]. Corrections are applied to the jet momenta to compensate the non-uniformity of the detector's response in $\mathrm{p_T}$ and η. These are known as the L1Fastjet and L2L3Residual corrections[25]. Additionally, the resolution of jet energies is known to be worse in data than in simulation. To correct this, jet energies in simulation are smeared by 10%. To further suppress fake jets arising from isolated photons, leptons and malfunctioning calorimeter channels, jets must satisfy the standard CMS loose jet identification criteria. Jets are required to have η in the range $|\eta| < 2.4$ and a $\mathrm{p_T}$ exceeding 30 GeV. Jets must also be separated from the nearest reconstructed

loose working point electron, as in Section 6.2.3, and loose working point muon, as in Section 6.2.2, by $\Delta R < 0.3$ in order to remove fake jets that have been reconstructed as the result of lepton showers.

Various *event-level* variables used in the analysis are based on the collective activity of these selected jets. The H_T of an event is defined as the scalar sum of the transverse momenta of the selected jets.

6.1.1 b-jet identification

The Combined Secondary Vertex version 2 algorithm, CSVv2, is used to identify or *tag* jets originating from b-quarks. This algorithm produces a discriminator variable with values ranging from 0 to 1 for each jet based on the impact parameter information of the tracks in the jets in combination with the presence of secondary vertex. Larger values of the discriminator correspond to more b-like jets. B-tagged jets are defined as those with discriminator values exceeding the medium working point of the Combined Secondary Vertex (CSV) version 2[30] algorithm, CSVM, of 0.800. This requirement yields an efficiency of selecting jets originating from b quarks of 69% and a mistag rate of selecting up, down, strange and gluon flavour jets of $\approx 1\%$. The usage of b-tagging in this analysis is discussed further in Section 7.2.1.

6.2 Lepton Identification

6.2.1 Relative Isolation

Relative isolation is defined by the PF algorithm as the ratio of the scalar-summed charged hadronic transverse energy ($E_T^{chargedhadronic}$) plus the summed neutral hadronic energy ($E_T^{CorrectedNeutralHadronic}$) plus the summed photon energy ($\Sigma E_T^{Photons}$) in a cone of R=0.4 to the muon's $\vec{p_T}$, i.e.,

$$RelIso = (\Sigma E_T^{chargedhadronic} + \Sigma E_T^{CorrectedNeutralHadronic} + \Sigma E_T^{Photons})/p_T^{\mu} \tag{6.1}$$

Charged hadrons which are associated to sub-leading primary vertices are ignored when calculating the isolation. In order to suppress the effect of neutral particles from

sub-leading primary vertices, a correction is applied to the neutral hadronic energy inside the cone.

For the relative isolation of muons, a cone size of $R = 0.4$ is used and a correction known as the $\Delta\beta$ is used. The correction is derived from the ratio of charged to neutral energy which has been measured to be ≈ 0.5. Hence, the neutral energy from sub-leading primary vertices in a jet, $E^{neutral,sub-leading}$ may be approximated as $0.5 \times E_{charged,sub-leading}$ and the 0.5 is referred to as the $\Delta\beta$ factor. The corrected neutral hadronic energy, $E_T^{CorrectedNeutralHadronic}$, for the $\Delta\beta$ correction is then defined as:

$$\Sigma E_T^{CorrectedNeutralHadronic} = max(0, \Sigma E_T^{NeutralHadronic} - 0.5 * \Sigma E_T^{chargedhadronic}) \quad (6.2)$$

where the max() function is used to ensure that the corrected neutral hadronic energy is never assigned a negative value. Thus, the more isolated a lepton is, the lower its relative isolation value.

For electrons, relative isolation is defined similarly as for muons but with a cone size of $R = 0.3$. Instead of the $\Delta\beta$ correction, electrons have their isolation corrected by a quantity derived from the event-specific average pile-up energy density per unit area in the phi-eta plane (ρ) and the effective area based on shower shapes that the EGM POG has measured. The product of these two quantities replaces the $0.5 * \Sigma E_T^{chargedhadronic}$ in the expression for the corrected neutral hadron energy resulting in the corrected neutral hadronic energy, $E_T^{CorrectedNeutralHadronic}$, for the Effective Area correction to be defined as:

$$\Sigma E_T^{CorrectedNeutralHadronic} = max(0, \Sigma E_T^{NeutralHadronic} - \rho * \text{EffArea}) \quad (6.3)$$

6.2.2 Muons

The initial muon collection in each event is defined as the set of PF candidates reconstructed as muons in the MiniAODv2 data format. The muons used in this analysis are defined further using the standard Run2 loose identification and isolation working point recommendations provided by the CMS muon POG. The details of how each cut is defined are found in reference [46]. They are required to satisfy the following criteria:

- Is a GlobalMuon OR a TrackerMuon
- Is a ParticleFlowMuon
- $p_T > 20$ GeV
- $|\eta| < 2.4$
- Relative isolation, RelIso, < 0.25

6.2.3 Electrons

The initial electron collection in each event is defined as the set of PF candidates reconstructed as electrons in the version 2 miniAOD data format. They are required to have a $E_T > 25$ GeV and be inside $|\eta| < 2.5$. Additionally, electrons used in this analysis are defined using the standard recommendations for the spring 2015 cut based loose working point provided by the CMS EGM POG. The details of how each cut is defined are found in reference [45]. Electrons passing the loose working point are required to satisfy the following criteria:

- Barrel Electrons $|\eta_{SuperCluster}| \leq 1.479$
  - full5x5_sigmaIetaIeta < 0.0103
  - abs(dEtaIn) < 0.0105
  - abs(dPhiIn) < 0.115
  - hOverE < 0.104
  - Relative Isolation using Effective Areas < 0.0893
  - ooEmooP < 0.102
  - abs(d0) < 0.0261
  - abs(dz) < 0.41
  - expectedMissingInnerHits ≤ 2
  - pass conversion veto
- Endcap Electrons $1.479 < |\eta_{SuperCluster}| \leq 2.5$
  - full5x5_sigmaIetaIeta < 0.0301

- abs(dEtaIn) < 0.00814
- abs(dPhiIn) < 0.182
- hOverE < 0.0897
- Relative Isolation using Effective Areas < 0.121
- ooEmooP < 0.126
- abs(d0) < 0.118
- abs(dz) < 0.822
- expectedMissingInnerHits ≤ 1
- pass conversion veto

Chapter 7

Event Preselection

7.1 Triggers

The events used in this analysis were collected using triggers based on the presence of a pair of leptons of the flavors appropriate to the channel. The names of these triggers and the data taking periods to which they correspond are listed in tables 7.1, 7.2 and 7.3. For all simulated samples, the trigger paths are analogous to the data paths only with a different version number from the HLT menu. In cases where more than one trigger path is recommended: if either path is fired, the event is accepted.

Dilepton trigger scale factors have been taken from [6] and have been applied to events passing the corresponding trigger paths.

7.2 Baseline event selection

In this section, a list of criteria applied to the reconstructed objects described in the previous sections in the events triggered by the double muon, muon-electron, and double electron triggers are detailed. These criteria form what will be henceforth referred to as the

Run range	HLT path
Run 2015C	HLT_Mu17_TrkIsoVVL_TkMu8_TrkIsoVVL_DZ_v2
Run 2015D	HLT_Mu17_TrkIsoVVL_TkMu8_TrkIsoVVL_DZ_v2

Table 7.1: Data period and corresponding trigger names for the $\mu\mu$ channel.

Run range	HLT path
Run 2015C	HLT_Mu17_TrkIsoVVL_Ele12_CaloIdL_TrackIdL_IsoVL_v2
	HLT_Mu8_TrkIsoVVL_Ele17_CaloIdL_TrackIdL_IsoVL_v2
Run 2015D	HLT_Mu17_TrkIsoVVL_Ele12_CaloIdL_TrackIdL_IsoVL_v3
	HLT_Mu8_TrkIsoVVL_Ele17_CaloIdL_TrackIdL_IsoVL_v3

Table 7.2: Data period and corresponding trigger names for the $e\mu$ channel.

Run range	HLT path
Run 2015C	HLT_Ele17_Ele12_CaloIdL_TrackIdL_IsoVL_DZ_v2
Run 2015D	HLT_Ele17_Ele12_CaloIdL_TrackIdL_IsoVL_DZ_v3

Table 7.3: Data period and corresponding trigger names for the ee channel.

baseline selection.

For each final state channel, pairs of opposite sign leptons are created based on the minimal working point requirements for that channel as outlined below. This analysis considered only opposite sign lepton pairs as the fake background estimation for same sign pairs is beyond the ability of the analyzers to perform at this time. In addition, the binned shape analysis based on a Boosted Decision Tree as described in section 9 is not appropriate for an opposite sign analysis for reasons discussed previously.

For the final states where the lepton pair consists of two leptons of the same species, a veto on the invariant mass of the dilepton pair is performed. The invariant mass of the pair is required to be outside of the range between 76 GeV and 106 GeV which represents a 30 GeV window around the Z-boson mass. This is referred to as the *ZVeto*. Additionally, pairs with invariant mass less than 20 GeV are excluded to remove contributions from low mass resonances. The criteria applied in the double muon, electron-muon, and double electron channels are as follows:

$\mu\mu$:

- Exactly one opposite sign lepton pair consisting of two loose isolated muons
- Exactly zero loose electrons
- Z mass veto on the lepton pair
- At least 4 jets with $E_T > 30$ GeV
- At least 2 jets passing the CSVv2M b-tagging criterion

- $H_T > 500$ GeV

  $e\mu$:

- Exactly one opposite sign lepton pair consisting of one loose isolated muon and one loose electron
- At least 4 jets with $E_T > 30$ GeV
- At least 2 jets passing the CSVv2M b-tagging criterion
- $H_T > 500$ GeV

  ee:

- Exactly one opposite sign lepton pair consisting of two loose electrons
- Exactly zero loose muons
- Z mass veto on the lepton pair
- At least 4 jets with $E_T > 30$ GeV
- At least 2 jets passing the CSVv2M b-tagging criterion
- $H_T > 500$ GeV

7.2.1 Btag re-weighting

Significant differences exist between the b-tagging efficiencies measured by the CMS BTV POG in data and those predicted by simulation. The BTV POG measures a set of scale factors, SF, which are defined as the ratio of the b-tagging efficiency in data to the efficiency in simulation, i.e.,

$$SF(\eta, P_T) = \frac{\epsilon(\eta, \mathrm{p_T})^{data}}{\epsilon(\eta, \mathrm{p_T})^{simulation}} \tag{7.1}$$

Scale factors are defined separately for b and light quark (u, d, s, g) jets and scale factors for c jets are defined to be the same as for b jets as is recommended by the CMS b-tagging group. As the baseline selection requires at least two medium working

point b-tagged jets, a re-weighting procedure is applied to simulated events in order to correct for the expected difference between the efficiency of this requirement in data and simulation. The chosen re-weighting procedure is one of the recommended methods of the BTV POG[17]. The method proceeds by defining the probability of an event in simulation producing a given number of tagged and untagged jets, P(MC),:

$$P(MC) = \prod_{taggedjets} \epsilon_i \times \prod_{untaggedjets} (1 - \epsilon_i) \tag{7.2}$$

where ϵ_i is the efficiency of tagging a jet flavour i within the CSVv2M criterion. While the probability of an event in data producing a given number of tagged and untagged jets, P(DATA), is defined as follows:

$$P(DATA) = \prod_{taggedjets} SF \cdot \epsilon_i \times \prod_{untaggedjets} (1 - SF \cdot \epsilon_i) \tag{7.3}$$

where SF is the appropriate scale factor for a jet of flavour i. The weight applied to simulated events, ω, is defined as

$$\omega = \frac{P(DATA)}{P(MC)} \tag{7.4}$$

7.2.2 Heavy Flavor Re-weighting

When discriminating $t\bar{t}$ from signal, background events must have extra jets from processes like gluon splitting. Since this analysis relies heavily on b-tagging information, $t\bar{t}$ events which have radiated a gluon that splits into a $b\bar{b}$ pair (termed *ttbb* events) will most closely resemble signal events. The analysis presented in reference [32] has measured the relative cross section of $t\bar{t}$ events with a $b\bar{b}$ gluon split to all events with an extra gluon split ($R = \sigma_{ttbb}/\sigma_{ttjj}$) and found a discrepancy between simulation and data[32]. In order to correct for this, we apply an event weight, $R_{Data}/R_{MC} = 1.71$, to events in simulation that are identified as *ttbb* events. These events are identified by using the generator level jets in the event. A jet is identified as coming from a b-parton by the existence of a b-hadron in

the jet cone. Jets with a $E_T \geq 20$ GeV and inside $|\eta| \leq 2.5$ are flagged as b jets. If an event has 3 or more b jets, it is flagged as a *ttbb* event. All other events are flagged as *ttll*, where l refers to a jet from a u, d, s, or c quark. In order to preserve the total $t\bar{t}$ cross section, *ttll* events are scaled down by a factor $(1 - R_{Data})/(1 - R)MC)$. This re-weighting is performed on all $t\bar{t}$ samples including those samples used for systematic variations.

7.2.3 Cut-flow

In tables 7.4, 7.5, and 7.6 the numbers of data events selected and the number of simulated events expected after each step of the baseline selections for each channel are detailed. After the baseline selection has been applied the $t\bar{t}$ component represents 93% of the total background.

Table 7.4: Cut flow for the $\mu\mu$ channel (2.6 fb^{-1} of int. lumi.)

	Data	$t\bar{t}t\bar{t}$	ST	$Z + jets$	$t\bar{t} + H$	$t\bar{t} + Z$	$t\bar{t} + W$	$t\bar{t}$
initial	48036797	22.07	155849.46	14530873.12	715.34	1543.27	970.28	209004.05
Trigger/PV	6058144	1.83	2720.99	2068610.88	18.96	184.92	74.29	24015.07
2 OS Iso μ	1938180	0.58	1262.81	1741352.19	4.69	88.40	32.72	13218.33
Mass Veto	185774	0.51	987.00	132178.65	3.68	24.88	29.02	10060.18
$\geq$ 4 Jets	1817	0.49	42.18	242.93	2.18	14.99	14.49	1114.82
$\geq$ 2 b-tags	569	0.36	13.64	7.97	1.68	5.22	5.03	445.30
HT $\geq$ 500 GeV	86	0.28	4.63	2.51	0.52	2.10	2.00	81.82

Table 7.5: Cut flow for the $e\mu$ channel (2.6 fb^{-1} of int. lumi.)

	Data	$t\bar{t}t\bar{t}$	ST	$Z + jets$	$t\bar{t} + H$	$t\bar{t} + Z$	$t\bar{t} + W$	$t\bar{t}$
initial	12510430	22.99	162491.79	15163979.81	745.89	1609.02	1010.56	217430.80
Trigger/PV	5645331	2.93	4957.15	69835.51	29.67	138.84	135.00	41679.93
1 Iso. μ	319559	1.69	3327.46	33152.64	14.43	72.58	90.29	30881.55
1 Iso. e	38807	0.97	2065.78	5906.39	7.39	37.24	55.70	21305.76
$\geq$ 4 Jets	2618	0.94	79.62	26.62	4.36	19.76	28.33	2358.83
$\geq$ 2 b-tags	1019	0.67	26.82	1.21	3.38	7.09	10.03	940.34
HT $\geq$ 500 GeV	185	0.51	7.76	0.40	1.07	2.70	4.08	172.13

Table 7.6: Cut flow for the ee channel (2.6 fb^{-1} of int. lumi.)

	Data	$t\bar{t}t\bar{t}$	ST	$Z + jets$	$t\bar{t} + H$	$t\bar{t} + Z$	$t\bar{t} + W$	$t\bar{t}$
initial	86664901	22.69	160333.38	14898761.85	735.96	1585.31	997.48	214705.42
Trigger/PV	4026394	1.30	1937.24	1841547.02	9.96	147.75	60.33	17598.97
2 OS Iso. e	1236546	0.41	828.57	1163426.12	2.95	63.12	22.22	8336.54
Mass Veto	108898	0.36	656.47	85183.43	2.39	19.34	20.05	6472.65
$\geq$ 4 Jets	1200	0.35	26.63	181.02	1.40	12.17	10.48	733.62
$\geq$ 2 b-tags	329	0.26	8.45	5.31	1.09	4.37	3.64	290.31
HT $\geq$ 500 GeV	69	0.20	3.14	0.98	0.36	1.92	1.41	55.99

Chapter 8

Data Validation and Modeling

8.1 Data-simulation agreement

In this section, the agreement between the distributions of all relevant variables in the data and simulated samples passing the baseline selection is discussed. Table 7.5, shows the samples of events passing the baseline selection are dominated by $t\bar{t}$ events. Due to the four jet and $H_T \geq 500$ GeV requirements, these $t\bar{t}$ events will be dominated by higher order processes containing multiple additional partons. Theoretical predictions for the cross section and kinematics of these processes are particularly sensitive to the choice of the factorization and renormalization scale. Hence the uncertainty on the normalization and shapes of the $t\bar{t}$ distributions arising from imperfect knowledge of these scales is expected to be the dominant systematic uncertainty. In order to make a fair comparison between data and simulation, the scale uncertainty on both the shape and normalization for each distribution under study is calculated using the procedure described in Section 10. In this section the distributions for the variables which characterize the objects and events in the baseline selected sample are shown. In each plot, the systematic uncertainty arising from the scale uncertainties is displayed by a hatched region. Additionally, since the signal is often too small to see compared to the dominant background, it is overlain and magnified 20 times. In each figure the lower plot shows the observed number of events in data divided by the predicted number of events in simulation.

The parton showering used for the simulated samples used in this analysis are processed using PYTHIA8 [47, 48]. The value of α_S used in the PYTHIA8 setup does not give a good description of the data. To correct for this, studies were carried out in order

to adjust the simulation to more accurately reflect the data. These studies are detailed in Appendix A and the method discussed in Appendix A.2 is applied to all simulation samples used in this analysis.

All events contributing to the plots in this section have passed the relevant baseline selection for the final state channel they represent: Figure 8.1 shows the jet multiplicity and H_T for the $\mu\mu$ channel, Figure 8.2 shows the the pseudo-rapidity and transverse momentum of the hardest muon, Figure 8.3 shows the invariant mass of the selected lepton pair, and Figure 8.4 shows the transverse energy spectra of the hardest and second hardest jets in the event. The μe channel is presented in Figures 8.5 through 8.8 and the ee channel is presented in Figures 8.9 through 8.12. In all cases, the data and simulation are in agreement within the tolerance of their uncertainties.

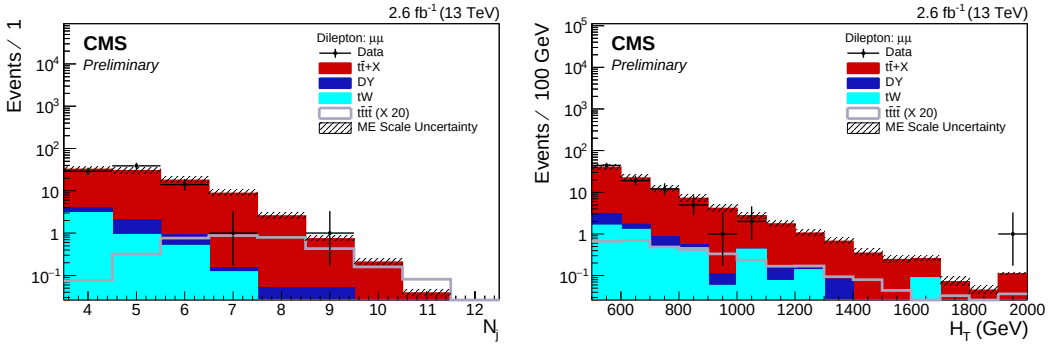

Figure 8.1: Number of jets (left) and the scalar sum of transverse jet energy (right) for the $\mu\mu$ channel.

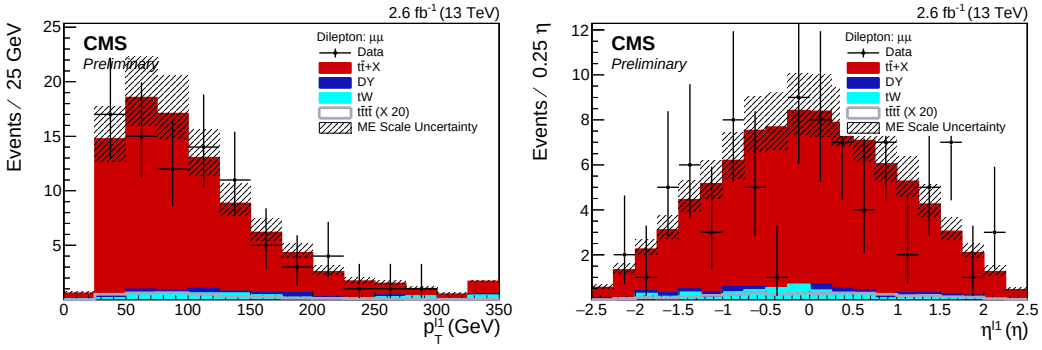

Figure 8.2: Transverse momentum (left) and pseudo-rapidity (right) of the leading lepton in the $\mu\mu$ channel.

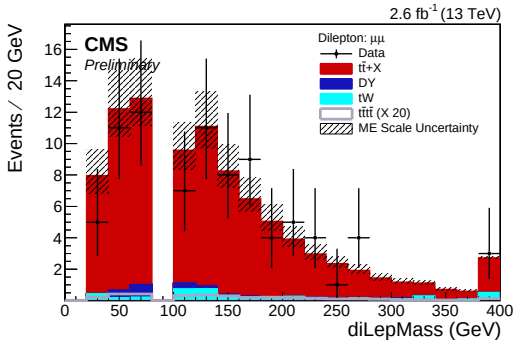

Figure 8.3: Invariant mass of the lepton pair in the $\mu\mu$ channel.

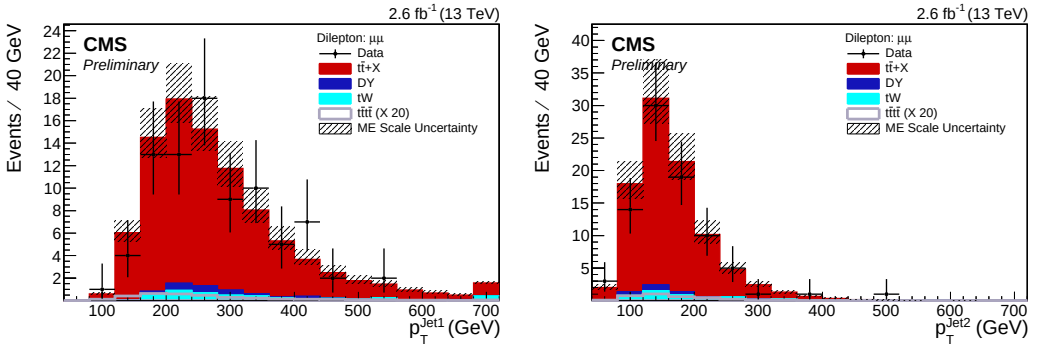

Figure 8.4: Transverse momentum of the hardest (left) and second hardest (right) jets in the $\mu\mu$ channel.

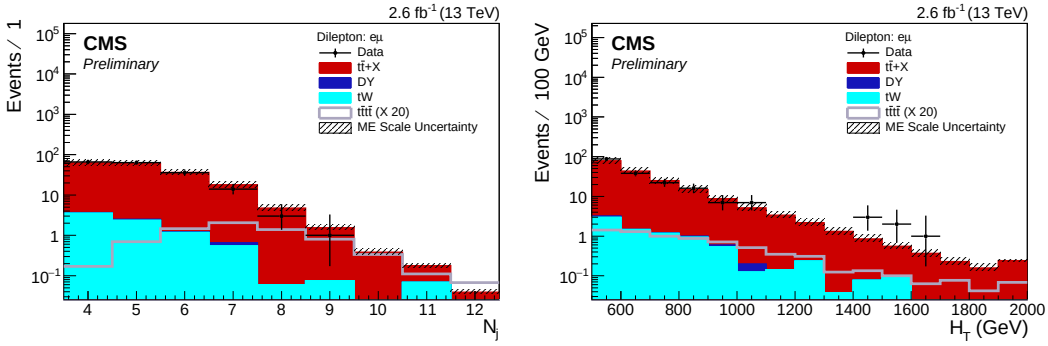

Figure 8.5: Number of jets (left) and the scalar sum of transverse jet energy (right) for the μe channel.

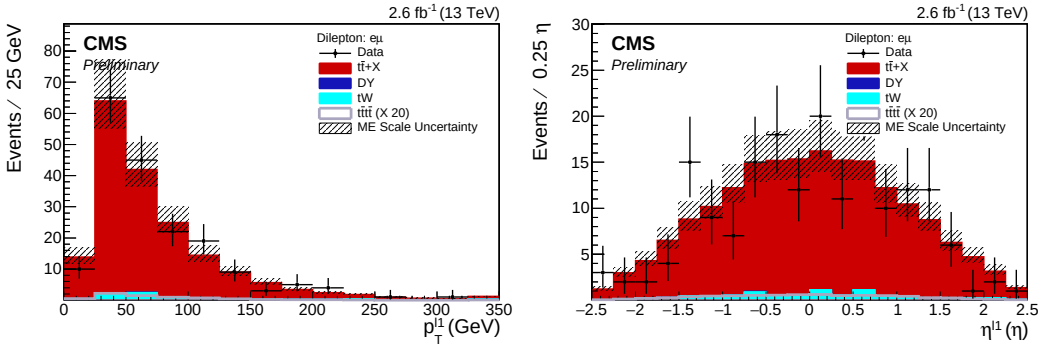

Figure 8.6: Transverse momentum (left) and pseudo-rapidity (right) of the leading lepton in the μe channel.

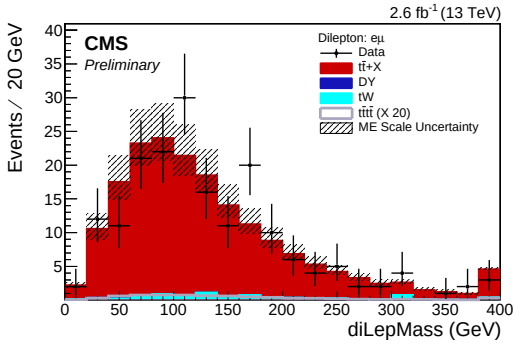

Figure 8.7: Invariant mass of the lepton pair in the μe channel.

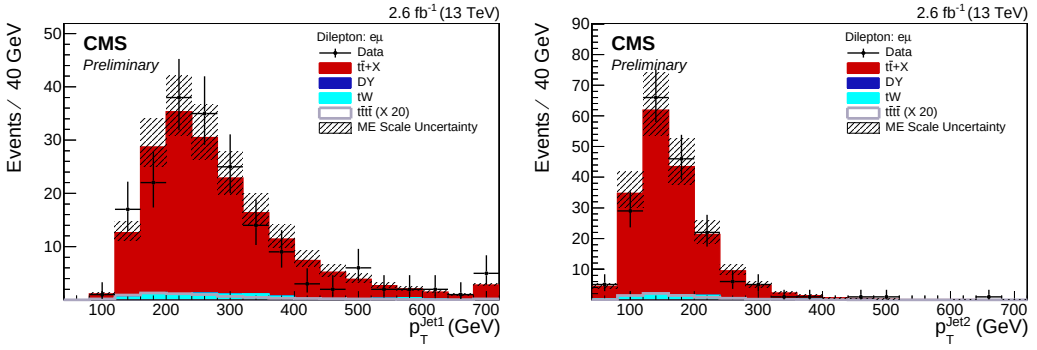

Figure 8.8: Transverse momentum of the hardest (left) and second hardest (right) jets in the μe channel.

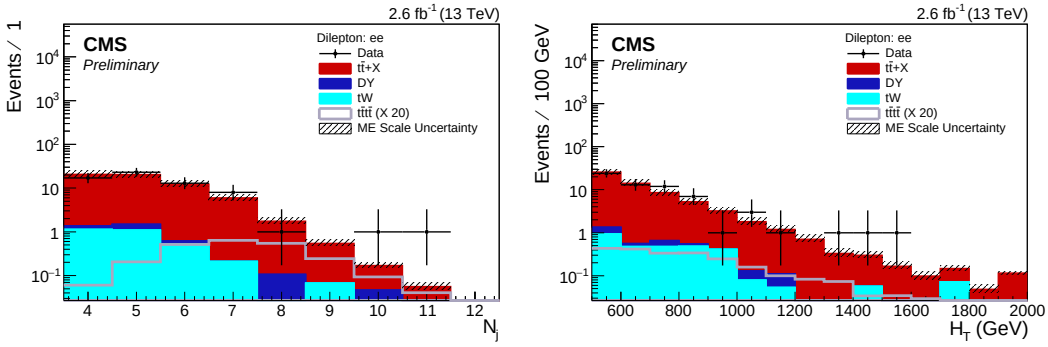

Figure 8.9: Number of jets (left) and the scalar sum of transverse jet energy (right) for the ee channel.

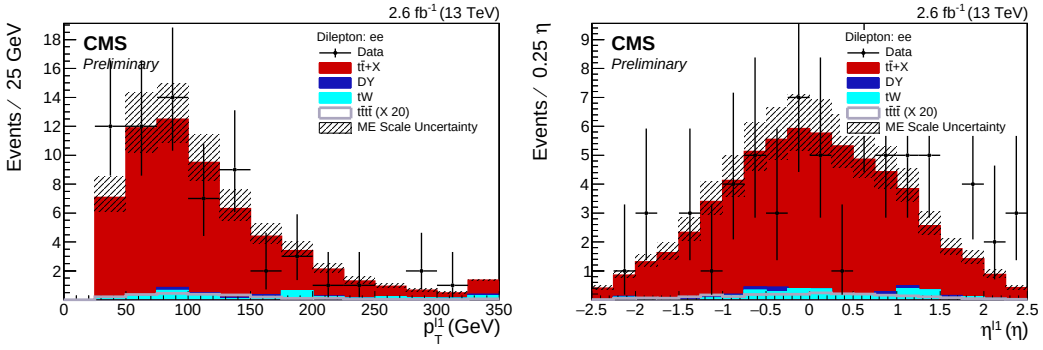

Figure 8.10: Transverse momentum (left) and pseudo-rapidity (right) of the leading lepton in the *ee* channel.

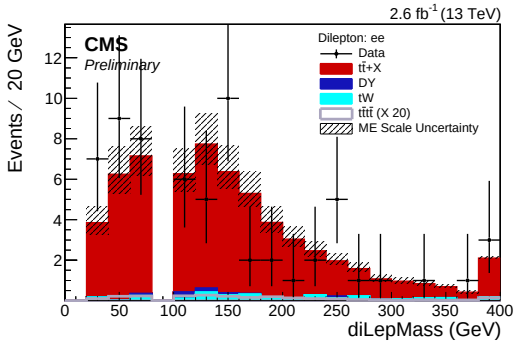

Figure 8.11: Invariant mass of the lepton pair in the *ee* channel.

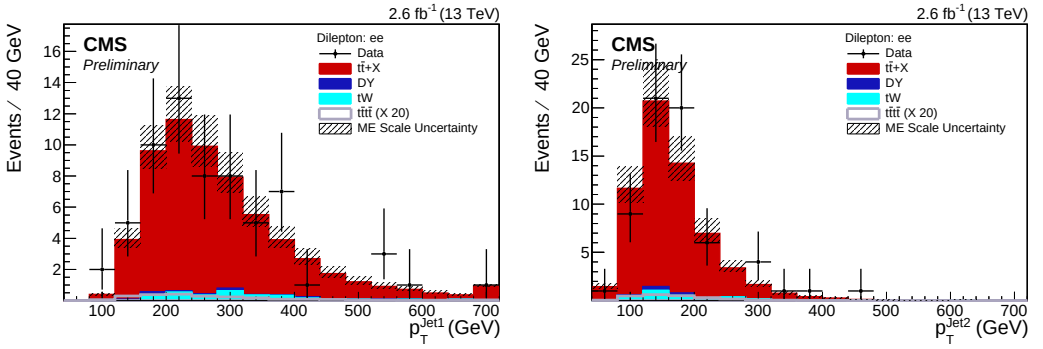

Figure 8.12: Transverse momentum of the hardest (left) and second hardest (right) jets in the *ee* channel.

Chapter 9

Multivariate Discrimination

As $t\bar{t}$ is by far the dominant background process after the baseline selection has been applied, sensitivity to $t\bar{t}t\bar{t}$ largely depends on the ability to further discriminate between this process and $t\bar{t}$. In this section, *event-level* variables which have the potential to distinguish between $t\bar{t}t\bar{t}$ and $t\bar{t}$ + jets events are detailed. The variables are grouped into four categories based on the underlying physical characteristics which they exploit: *Top-content*, *Event activity*, *Event topology*, and *b-jet content*. Unless otherwise indicated, all plots in the section are the addition of the three final state channels in order to provide sufficient statistics to make a determination of their agreement in data and simulation. The differences in leptonic kinematics across the final state channels has been shown to cause negligible differences in the variables presented here.

9.0.1 Top-content

The presence of multiple hadronic top quarks in di-leptonic $t\bar{t}t\bar{t}$ events may be exploited to distinguish these events from the $t\bar{t}$ + jets background which contain no hadronic top quarks.

The $anti-K_T$ jet reconstruction algorithm employed in this analysis can not resolve jets which have, $\Delta R = \sqrt{\theta^2 + \phi^2}$, the distance between the jets in $\eta - \phi$ space, of less than 0.4. Thus a hadronic top quark may only be deemed *reconstructible* if the minimal ΔR between any two of the three jets produced from the decay exceeds 0.4. In the previous search for four top quarks at 8 TeV [31], studies on the viability of the hadronic top reconstruction were carried out looking at the number of reconstructable hadronic top

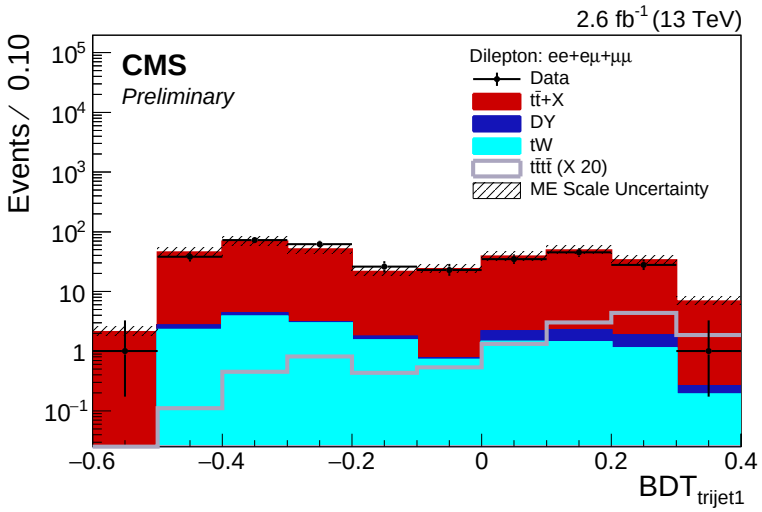

Figure 9.1: $BDT_{trijet1}$ combined across channels.

quarks in $t\bar{t}t\bar{t}$ and $t\bar{t}$ events. This study determined that a large fraction of semi-leptonic $t\bar{t}t\bar{t}$ events contained at least two reconstructable hadronic top quarks while a negligible fraction of semi-leptonic $t\bar{t}$ events did. This behavior is extended to the dilepton case with one less reconstructable hadronic top quark in each sample type.

As in the previous work, the key challenge in the reconstruction of a hadronic top in an event containing many jets is the correct selection of the three jets which arise from the same top quark. Employing the technique taken from the 8 TeV analysis, jets in the event are combiatorically grouped into tri-jets and then passed through a Boosted Decision Tree, BDT, algorithm to differentiate good from bad tri-jets. The BDT discriminant value of the highest ranked tri-jet is given the name $\mathrm{BDT_{trijet1}}$ and will be used to discriminate between $t\bar{t}t\bar{t}$ and $t\bar{t}$.

9.0.2 Event activity

Given that nominal dileptonic $t\bar{t}t\bar{t}$ events will contain up to eight hard jets from top decays while $t\bar{t}$ events will contain only up to two, variables based on the hadronic activity of the event will possess discrimination power. The most obvious variable is the number of reconstructed jets $\mathrm{N_j}$, which is shown in Figure 9.2. The weighted jet multiplicity ($\mathrm{N_j^W}$) takes this into account by folding the jet multiplicity with the $\mathrm{p_T}$ spectrum. This is

defined as

$$N_{\mathrm{j}}^{\mathrm{W}} = \frac{\int_{30}^{125} N_{\mathrm{j}}\left(E_{threshold}\right) * E_{threshold}\ dE_{threshold}}{\int_{30}^{125} E_{threshold} dE_{threshold}} = \frac{\Sigma_{0}^{N_{\mathrm{j}}} N_{\mathrm{j}}\left(E_{threshold}\right)\left[E_{threshold}^{2}/2\right]_{E_{upper}}^{E_{lower}}}{\left[E_{threshold}^{2}/2\right]_{30}^{125}}, \tag{9.1}$$

where $\mathrm{E}_{threshold}$ is the $\mathrm{p_T}$ threshold above which a jet is counted. $N_{\mathrm{j}}\left(E_{threshold}\right)$ are the number of jets above the energy threshold, E_{lower} is the set of $[30, E_j]$ and E_{upper} is the set of $[E_j, 125]$, where E_j are the energies of each jet in ascending order. This equation can be solved analytically as shown in the right part of Eq. 9.1. The numerator can be split into a sum of integrals in which the number of jets are constant in each of the integral ranges. It has higher values for events with many high-$\mathrm{p_T}$ jets than for events with the same number of jets where only few are high $\mathrm{p_T}$ and the rest are close to the selection threshold.

Another such variable is the $\mathrm{H_T^b}$, defined as the scalar sum of the $\mathrm{p_T}$ values of all the b-tagged jets in the event. Signal events will contain four b-jets originating from the decay of top quarks while background events will contain only two, with the additional b-jets coming from $\mathrm{g} \to \mathrm{b\bar{b}}$, which should be approximately the same in both cases. As the b jets originating from top decays tend to have larger values of $\mathrm{p_T}$ than those arising from other processes, the $\mathrm{H_T}$ of the b-tagged jets, $\mathrm{H_T^b}$ will tend to have larger values for signal than for background.

Additionally, the transverse energy of the 3rd and 4th hardest jet should provide discrimination between signal and background. In $t\bar{t}$ events these jets will come from bremstrahlung and thus have softer spectra than the jets coming from decay of top quarks in $t\bar{t}t\bar{t}$ events. Further jets are not considered as the pre-selection only guarantees the presence of 4 jets in the event. Given that the two jets in $t\bar{t}$ events are the b-jets required to select the event, the transverse jet energy beyond those two b-jets holds additional discriminating power. This is defined as $\mathrm{H_T^{2M}}$.

9.0.3 Event Topology

A complimentary strategy to the top content discrimination strategy aims to use the difference in the hadronic activity between $t\bar{t}$ and $t\bar{t}t\bar{t}$ in tandem with the large $\mathrm{H_T}$ requirement specified in the baseline selection. In di-leptonic $t\bar{t}$, only up to two jets that come from hard processes. Any other hadronic activity in the event will necessarily arise

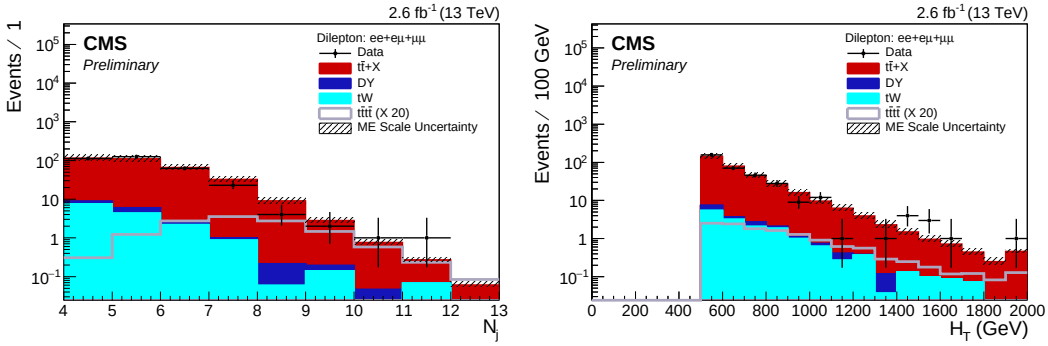

Figure 9.2: Number of jets across all channels (left) and the scalar sum of transverse jet energy (right).

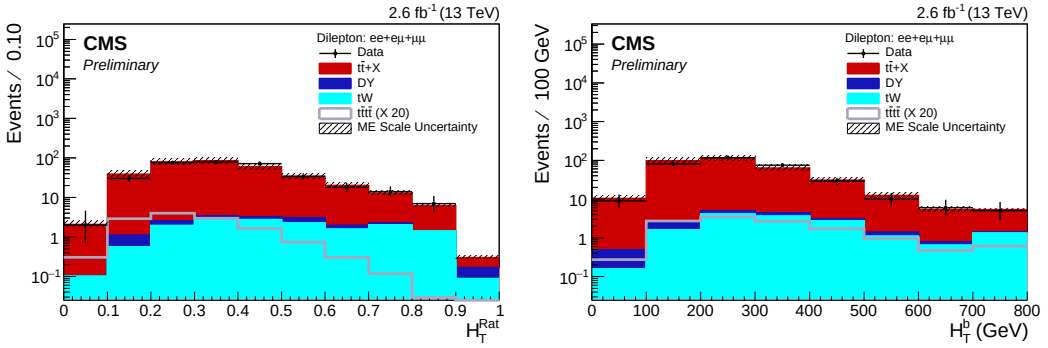

Figure 9.3: The ratio of the scalar sum of the two selected b-jets transverse energy to the H_T of the whole event (left) and the scalar sum of transverse b-jet energy (right).

from gluon splitting and initial or final state radiation, ISR/FSR. The $t\bar{t}$ system will recoil off any ISR/FSR boost, causing $t\bar{t}$ events to be less central than $t\bar{t}t\bar{t}$ events which have significantly more hadronic energy from hard processes.

The Centrality of a group of objects can be defined as the ratio of the scalar summed transverse energy to the scalar summed total energy of those objects. The centrality of the jets in the event is defined as C.

The Sphericity of a group of objects is defined by creating the matrix shown in equation 9.2 from the three principal components of their momenta where α and β refer to the principal momenta of the i-th particle. Solving the eigenvalue problem of the tensor, one constructs the sphericity, $S = \frac{3}{2}(\lambda_2 + \lambda_3)$, where λ_2 and λ_3 are there two smallest

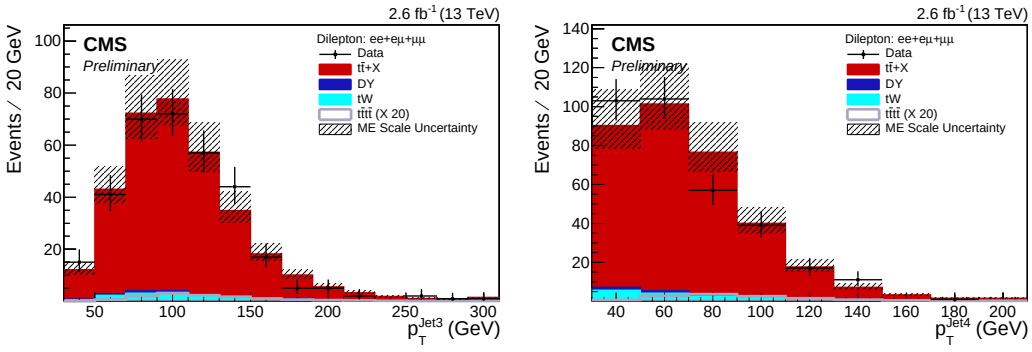

Figure 9.4: The transverse energy of the 3rd hardest (left) and and 4th hardest (right) jets.

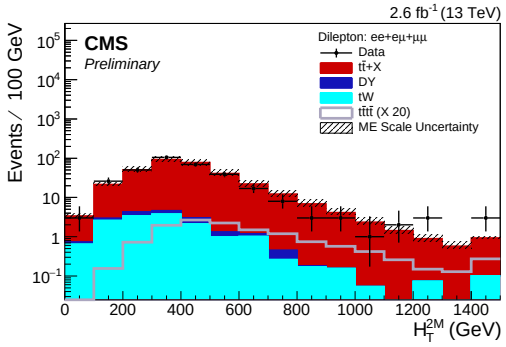

Figure 9.5: The scalar sum of the transverse jet energy minus the transverse energy of the two selected b-jets.

eigenvalues of $S^{\alpha\beta}$.

$$S^{\alpha\beta} = \frac{\sum_i p_i^\alpha p_i^\beta}{\sum_i |\vec{p}_i|^2} \tag{9.2}$$

Additionally, angular separations of the two leptons or the two b-jets selected in the event could provide additional discrimination. The separation in the polar-azimuthal space defined as $\Delta R = \sqrt{\Delta\phi^2 + \Delta\eta^2}$ is used to calculate $\mathrm{dR_{ll}}$ and $\mathrm{dR_{bb}}$ respectively.

9.0.4 B-jet content

As the branching ratio of top quarks to a b quark and a W boson is $\approx 100\%$, signal events containing four top quarks will contain four b quarks; while the main background

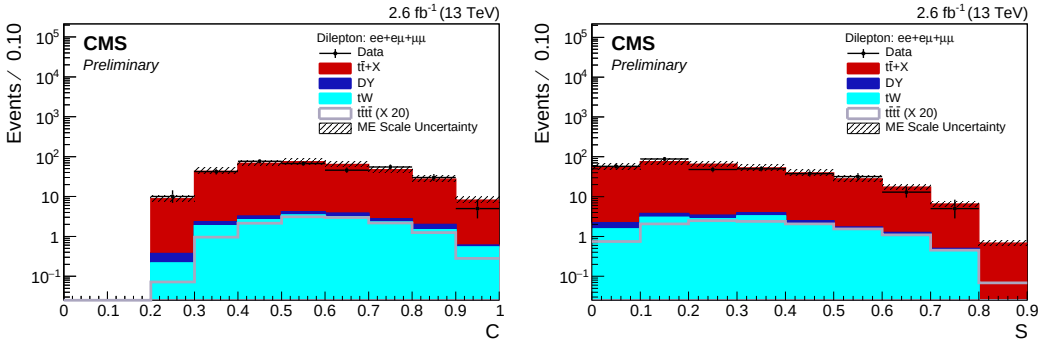

Figure 9.6: The ratio of the scalar sum of the transverse jet energy to the scalar sum of the jet energy (left) and the sphericity of all reconstructed objects in the event (right).

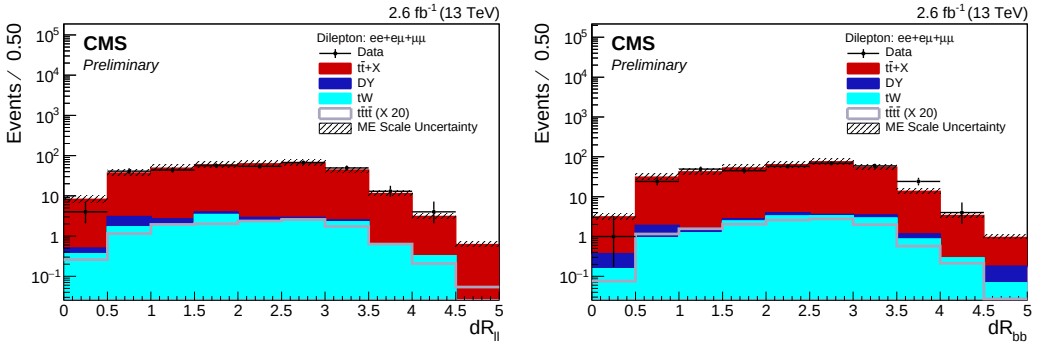

Figure 9.7: The separation in polar-azimuthal space of the lepton pair (left) and the two selected b-jets (right).

process, $t\bar{t}$ + $l\bar{l}$, typically produces two b-quarks. Hence, the presence of more than two b-tagged jets is a potentially important source of discriminating power. While the event level selection is done using the medium tagging working point, the distributions of the light tagging working point also provides additional discriminating power.

9.0.5 Lepton content

Finally, the p_T and η of the leading lepton in the event may provide discrimination based on the kinematic differences between $t\bar{t}t\bar{t}$ and $t\bar{t}$ and is not strongly correlated to the

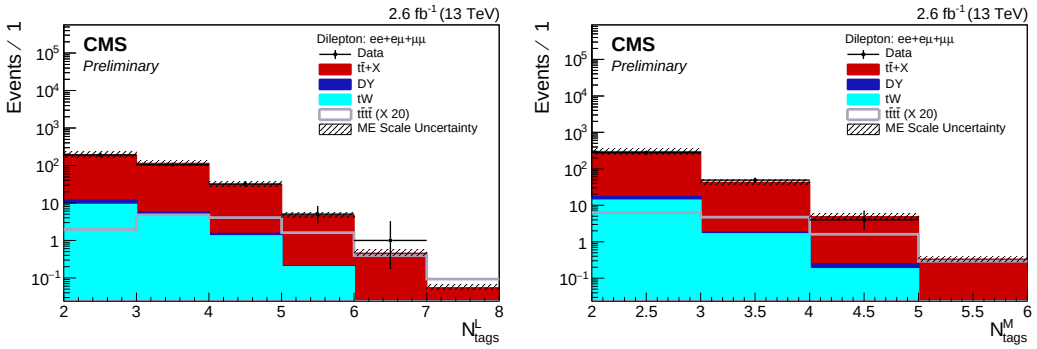

Figure 9.8: The number of jets passing the light (left), medium (center), and tight (right) working points of the CSVv2 b-tagging algorithm.

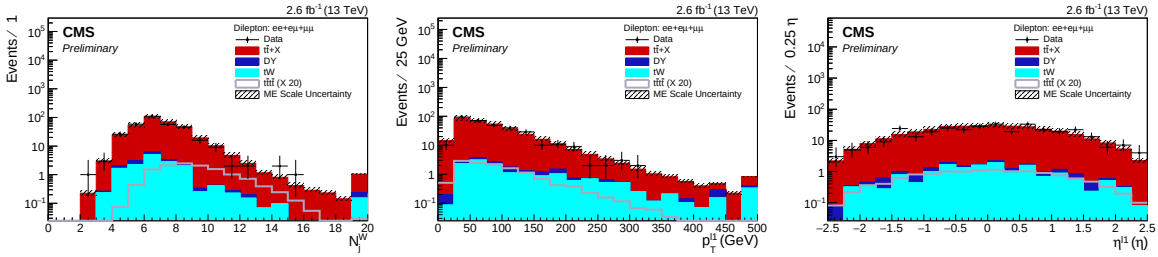

Figure 9.9: The weighted jet multiplicity (left), p_T of the leading lepton (center), and η of the leading lepton (right).

hadronic information presented above.

9.0.6 Event-level BDT

The event-level variables described thus far will now be used the input variables for an event-level, BDT discriminator. The distributions of these variables are shown in Figure 9.10. Due to the limited statistics available in each channel in the dilepton final state, the event level BDT is trained on a combination of all three final states simultaneously. Since, there should be little to no kinematic difference between the final states due to lepton species this allows for a larger sample of events and ensures the smoothness of the distributions used in the BDT training.

Evaluation of the BDT discriminator is carried out on a channel by channel basis

and is combined in the final limit setting process, is described in Chapter 11. The agreement of the BDT discriminator distributions between data and simulation will also be discussed in Chapter 11.

Training of the Event-level BDT is carried out using version 4.2.0 of the TMVA library[14, 37, 40] using the AdaBoost boosting algorithm. A forest of 400 decision trees are generated using the Gini Index to determine separation at each node. The trees are restricted to a maximum depth of 3 cuts with a minimum amount of events per node of 5% of the total input samples. The aggregate, weighted response of the forest is used to output the discriminator value.

While each variable provided to the BDT training is expected to contribute to the discrimination between signal and background, the jet multiplicity, N_j, provides the most out of the box differentiation between signal and background and thus will contribute highly in the BDT. As mentioned in Section 8.1, the poor modeling of the parton showering in the default tune of PYTHIA8 causes deviation of the data/simulation agreement in the tails of hadronic distributions such as N_j. A scale factor is used to correct this disagreement and is applied as a weight to events entering the BDT training so that the shape of the N_j tail is properly modeled. This is done in an attempt to prevent sub-optimal efficiency in the BDT when it is applied to data caused by a discrepancy in the shape of the highest contributing variable.

A study was carried out concerning the use of negative event weights from the aMC@NLO generator. This is shown in Appendix B. The results of the study were inconclusive with a marginal preference to the GradNeg strategy. However, after much discussion, the AdaBoost strategy was chosen to extract limits. For this, all events provided to the BDT training are assigned a unity weight. Any mismodeling uncertainty coming from this choice will be significantly smaller than other dominant sources of systematic uncertainty.

TMVA separates the input events into a training and test sample in order to test that the forest has not been over-trained and has learned to pick out individual fluctuations in the training sample. If the forest has not been over-trained, then the output discriminator distributions of the test and training sample should be the same assuming there are enough events to populate the bins sufficiently. Figure 9.11 shows that the response of the signal and background for both the test and training samples agrees quite well but could be tuned prevent further overtraining. Additionally, the separation is quite good.

Table 9.1: Rankings of the variables used in the BDT training.

Rank	Variable Name	Variable Frequency
1	N_j	1.177e-01
2	$BDT_{trijet1}$	1.134e-01
3	N_j^W	8.614e-02
4	S	6.478e-02
5	p_T^{Jet4}	6.358e-02
6	N_{tags}^M	6.150e-02
7	dR_{bb}	6.143e-02
8	H_T^{2M}	5.964e-02
9	H_T^{Rat}	5.810e-02
10	dR_{ll}	5.381e-02
11	N_{tags}^L	5.305e-02
12	H_T^b	4.892e-02
13	C	4.465e-02
14	η_{l1}	4.023e-02
15	p_T^{l1}	3.937e-02
16	p_T^{Jet3}	3.373e-02

9.0.7 BDT Variable Ranking

After training, TMVA reports on the frequency of the use of each input variable. This can be thought of as a measure of the discrimination power of the variables used in the BDT and are shown in Table 9.1. Figures 9.12 and 9.13 show the correlation matrix from the BDT training for the signal and background samples respectively.

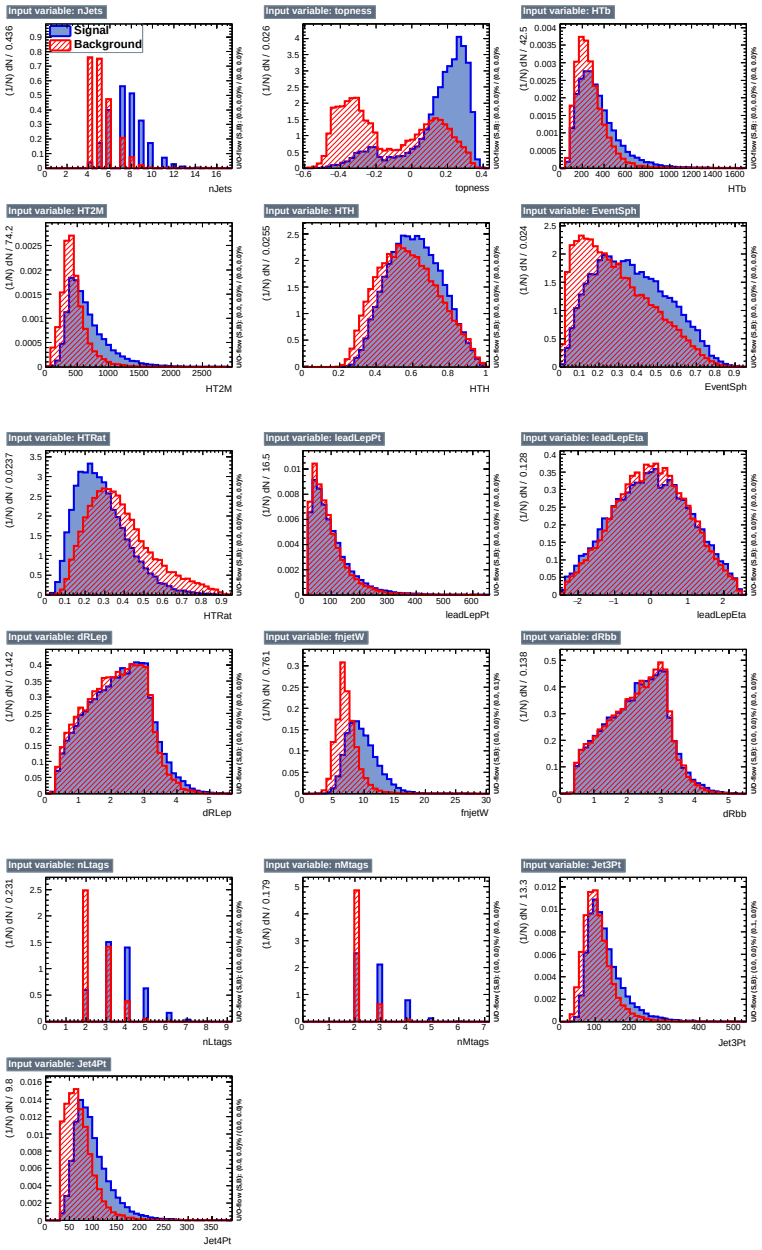

Figure 9.10: Input variable distributions to the BDT for signal (blue) and background (red).

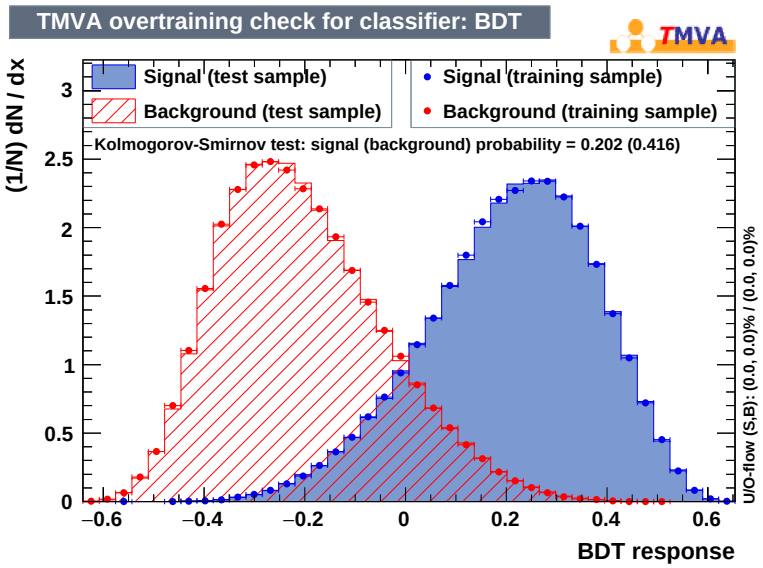

Figure 9.11: Classifier response for the trained BDT.

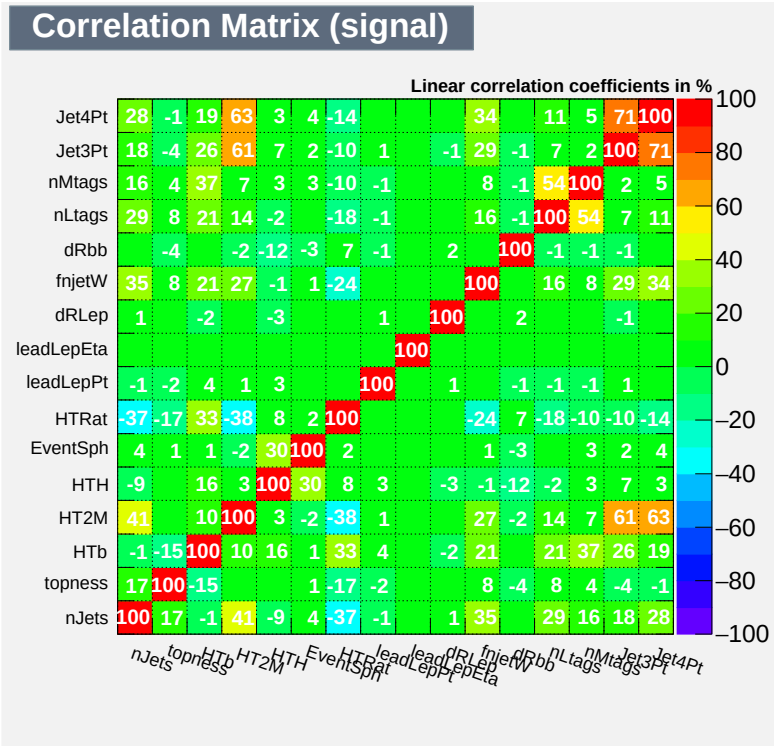

Figure 9.12: Correlation Matrix of BDT variables after training for Signal.

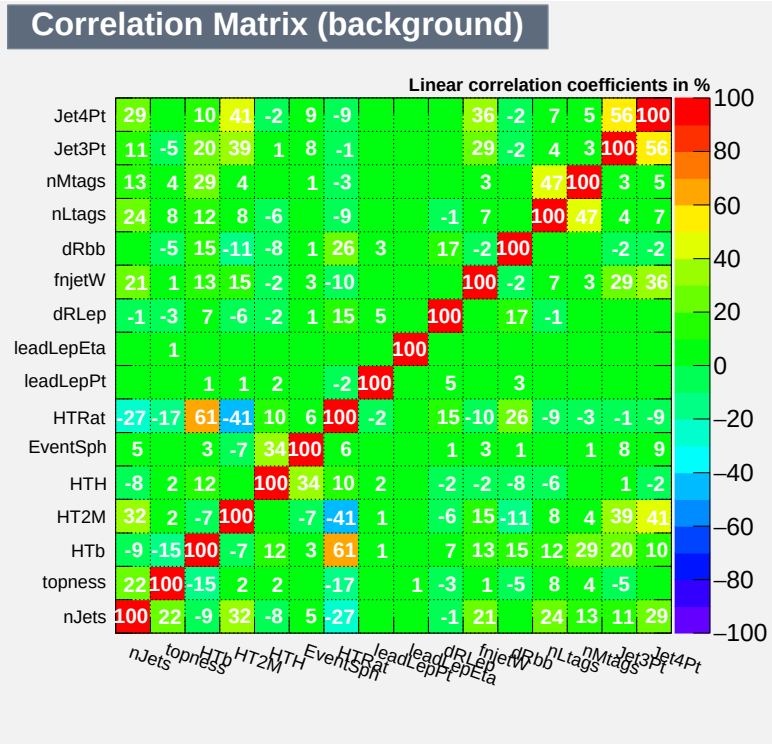

Figure 9.13: Correlation Matrix of BDT variables after training for Background.

Chapter 10

Estimating the Systematic Uncertainties

The systematic uncertainties considered in this analysis may be separated into two categories: uncertainties which affect the normalization and those which affect shape of the distributions. The normalizations of the simulated components which enter into the limit setting procedure are calculated via a template fit to data. Thus, the normalization uncertainties should only affect the uncertainty on the expected and observed limits, not the limits themselves. In this section, each source of systematic uncertainty is discussed with details of the method of its calculation and its estimated size.

10.1 Normalization Uncertainties

Luminosity A luminosity uncertainty of 2.7% is included from the recommendations of the CMS luminosity group.

Monte Carlo cross sections As the $t\bar{t}$ process dominates the sample of events selected by the baseline selection, the cross section uncertainty on this process is expected to be dominant cross section uncertainty. It is taken from [33] and gives an asymmetric uncertainty of $^{+2.5\%}_{-3.4\%}$ (scaling) $^{+6.2\%}_{-6.4\%}$ (pdf).

Lepton Trigger, ID, and Isolation The uncertainty coming from the choice of triggers and lepton identification criteria is included as a nuisance parameter in the limit calculation (see Chapter 11). Combined, these yeild a total lepton uncertainty of 4.3% in the $\mu\mu$ channel, 4.6% in the μe channel, and 4.8% in the ee channel.

10.2 Shape Uncertainties

Matrix Element Factorization and Renormalization scales In this section, the effect on the final results originating from imperfect knowledge of the appropriate factorization and renormalization scales is discussed. Because of the dominance of the $t\bar{t}$ component of the background, only the effect on the $t\bar{t}t\bar{t}$ signal and the $t\bar{t}$ backgrounds are considered. LHE weights are available in the $t\bar{t}$ MINIAODSIM sample which correspond to the variation of the factorization and renormalization scale (μ_f, μ_s) individually through the values of $1/2\mu$, μ and 2μ, where μ indicates the central value, giving nine weights in total. An envelope is calculated around the six alternative histograms which do not include the central value (u,u) or the extreme values with the scale parameters moving in opposite directions; namely (2μ, $1/2\mu$) and ($1/2\mu$, 2μ). The effect on the $t\bar{t}t\bar{t}$ signal and background are considered uncorrelated.

Parton Shower Scale To evaluate the effect on the background shape due to imperfect knowledge of the scale used in the parton shower calculations, the Q^2 scale is shifted up and down by a factor of 4 in a similar way to the matrix element scale. Independent samples are produced with these shifts in the Q^2 scale and used as the Up and Down shape uncertainties. Since changing the scale translates into changing the value of α_S, the parton shower scale shapes have been inflated relative to the nominal shape by a factor of 1.5 in order to also cover the uncertainty on the value of α_S used in the α_S adjustment.

JES As previously mentioned, the standard jet energy corrections are applied. To evaluate the effect on the signal and $t\bar{t}$ background shapes due to imperfect knowledge of the jet energy scale, we vary it by $\pm 1\sigma$ and produced the corresponding BDT discriminator distributions.

JER As described in section 6.1, the energies of jets in simulation are smeared by 10 % to account for the observed discrepancy between the jet energy resolution, JER, in data and simulation. To evaluate the systematic effect, the smearing is varied it by $\pm 1\sigma$ for both signal and the $t\bar{t}$ background.

B-tagging As detailed in section 7.2.1, the difference between b-tagging efficiency in data and simulation is accounted for by the application of scale factors to simulated events via and event weighting procedure. Given the significant uncertainty on the scale factors, and the fact that the number of b-tagged jets, N^{M}_{tags} is an input variable to the BDT algorithm, a significant systematic effect is expected. This is quantified by varying

independently the scale factors for light (u,d,s) and heavy (c,b) jets by $\pm 1\sigma$ for both the signal and $t\bar{t}$ background shapes. Since the raw CSV value is used in the Hadronic top reconstruction BDT, we have inflated the btagging systematics by a factor of four to account for the discrepancy in the CSV distribution observed between data and simulation.

$t\bar{t}$ Heavy flavor content Differences between simulation of $t\bar{t}$ and data due to the fraction of additional b quarks from gluon splitting have been observed. To account for this uncertainty, the contribution from events with extra heavy flavor jets is varied based on the uncertainty on the measured $\sigma_{t\bar{t}b\bar{b}}$ cross section[32]. An anti-correlated uncertainty on the measured cross section of $\sigma_{t\bar{t}l\bar{l}}$ is evaluated simultaneously.

Pile up The systematic uncertainty on the signal and $t\bar{t}$ background shapes introduced by the pile-up re-weighting procedure described in Section 7.2 is quantified by varying by $\pm 1\sigma$ the mean of the true of interactions distribution to which the simulation is re-weighted in order to match.

Generator choice The systematic uncertainty introduced by the choice of matrix element generator for the $t\bar{t}$ sample (Powheg) is evaluated by comparing the output BDT shape with that of a sample created with a different generator (MadGraph MLM). The difference of these shapes is taken to be a symmetric, systematic uncertainty.

Chapter 11

Results for Each Decay Channel

11.1 Calculating an upper limit on SM four top production

In lieu of an excess of events over the background expectation consistent with SM $t\bar{t}t\bar{t}$ production, upper limits on $\sigma_{t\bar{t}t\bar{t}}$ will be calculated. The previous result, described in [31], was determined by splitting the BDT distributions into N_j categories and substantially increased the expected sensitivity over that of an inclusive N_j bin strategy. We replicate that strategy for this analysis.

11.1.1 Blinding strategy

If an effort to not bias future results, this analysis was blinded during the initial review stage by the CMS TOP analysis group. Thus, the final BDT discriminant or the data in the signal region was not viewed and no observed limits were extracted. Following approval by the TOP analysis group conveners, this analysis was unblinded in June 2016.

11.1.2 Limit extraction using BDT distributions in exclusive N_j categories

The N_j categorization used for this analysis is defined by combining the 4 and 5 jet events, the 6 and 7 jet events, and all events above 8 jets inclusive. The BDT output distributions for these categories in each final state can be seen in Figures 11.1 through 11.3.

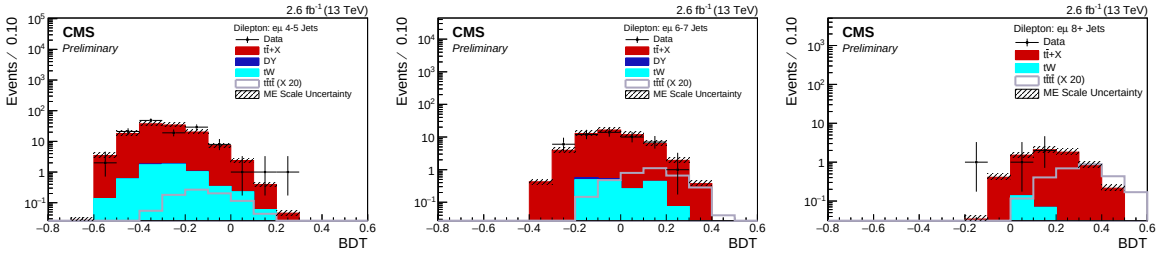

Figure 11.1: *BDT* output for the pre-fit 4-5 jet (left), 6-7 jet (center), and 8+ jet (right) categories in the μe channel.

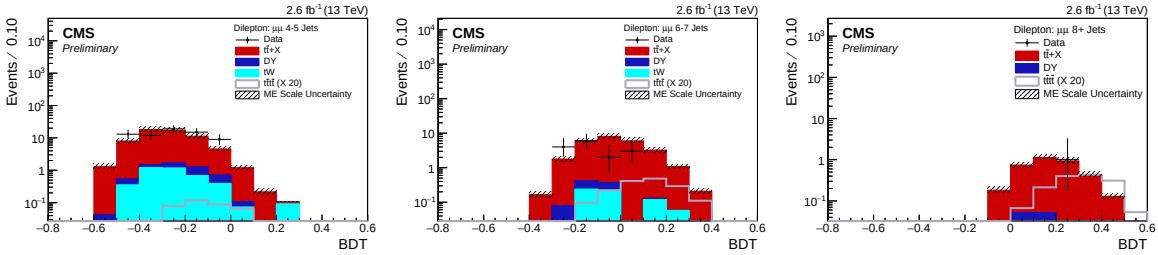

Figure 11.2: *BDT* output for the pre-fit 4-5 jet (left), 6-7 jet (center), and 8+ jet (right) categories in the $\mu\mu$ channel.

11.2 Simultaneous Maximum Likelihood Fit

As no deviation from the background-only prediction is expected in the SM, an upper limit is set using the asymptotic CL_S method included in the ROOSTATS framework [43, 10]. The BDT output distributions of signal and background are fitted using a simultaneous maximum likelihood fit to the data. Log-normal functions are used to model the normalization nuisance parameters, whereas the shape uncertainties are modelled using gaussian nuisance parameters. The "Lightweight Beeston-Barlow" method [11] is used to model statistical uncertainties where one nuisance parameter is associated with the estimate of the total simulation and the statistical uncertainty in each bin.

The 95% confidence level (CL) upper expected limits are extracted from the fit to the data for each dilepton final state channel and then combined to improve the sensitivity of the measurement. Table 11.1 contains the limits for each final state as well as the combination for both categorized and inclusive strategies. Just as in the 8 TeV single

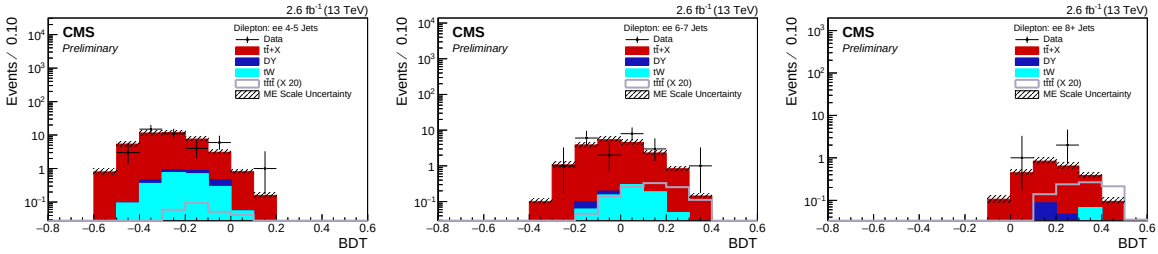

Figure 11.3: *BDT* output for the pre-fit 4-5 jet (left), 6-7 jet (center), and 8+ jet (right) categories in the *ee* channel.

Channel	Inclusive			Categorized		
	Observed	Expected	Uncertainty	Observed	Expected	Uncertainty
$\mu\mu$	30.2	40.9	$+37.0 - 19.1$	27.6	45.7	$+15.3 - 18.4$
μe	26.8	39.4	$+28.0 - 15.2$	21.6	35.6	$+25.3 - 13.3$
ee	106.3	82.6	$+63.9 - 33.3$	105.3	81.7	$+58.5 - 31.1$
Combined	18.6	27.6	$+19.6 - 10.5$	15.9	23.6	$+16.4 - 8.8$

Table 11.1: Extracted limits for both inclusive and N_j categorized strategies in multiples of $\sigma^{SM}_{t\bar{t}t\bar{t}}$.

lepton analysis, an improvement in the sensitivity from event categorization is seen here.

Tests on the goodness of the fit are shown in Appendix C.

Chapter 12

Combination of Results from Single Lepton and Dilepton Channels

12.1 Single Lepton Channel Analysis

Developed in parallel to this analysis, a search for four top production in the single lepton channel was also carried out. This search used complimentary strategies but modified to be appropriate for the single lepton channel topology. One of the biggest differences is that in the main $t\bar{t}$ background for the single lepton final state, there is one real hadronically decaying top quark present in the event. Thus, when using the hadronic top reconstruction BDT, one has to look for the *second* most likely tri-jet combination which is exclusive from the highest ranked tri-jet. This requires the baseline selection to require 6 jets in order to accommodate in number of jets needed to reconstruct these two tri-jets.

The single lepton channel occupies a much larger piece of the four top branching fraction and thus many more events pass the baseline selection. This increase in statistics allows the categorization of the single lepton channel to be more granular. In addition to splitting into jet categories, the single lepton analysis also splits into categories based on the number of b-tagged jets. This two dimensional categorization improves the reach of the search and is expected to perform well in the dilepton channel once more data is available.

A combination is performed with this analysis to extend the sensitivity of the search. The treatment of the systematic uncertainties has been coordinated between the channels and these have been taken to be correlated where appropriate to provide a global fit on the nuisance parameters. Only a combination of the categorized fits is performed. A

summary of the single lepton, dilepton, and combined 95% CL upper limits can be see in Table 12.1.

Table 12.1: Expected and observed 95% CL upper limits on the standard model four top quark production as a multiple of $\sigma^{SM}_{t\bar{t}t\bar{t}}$. The values quoted on the expected limits are the 1σ uncertainties.

Channel	Expected Limit (x $\sigma^{SM}_{t\bar{t}t\bar{t}}$)	Observed Limit (x $\sigma^{SM}_{t\bar{t}t\bar{t}}$)
Single Lepton	$12.7^{+7.8}_{-4.4}$	16.1
Dilepton	$22.3^{+16.2}_{-8.4}$	14.9
Combined	$10.8^{+6.7}_{-3.8}$	10.2

12.2 Impact of Uncertainties on Combined Analysis

A study was then performed to determine the most significant source of systematic uncertainty. This was done by removing shape uncertainties from the fit one at a time and then observing the change in the central expected limit post fit. Only shape parameters are considered as normalization parameters will only effect the uncertainty on the extracted limit. As seen in Table 12.2, the choice of matrix element scale for the signal has the greatest effect on the expected limit. This is to be expected, as changes in the signal strength would dramatically alter the limit calculation. Other uncertainties impact the limit calculation only slightly indicating that there is sufficient coverage from other sources of uncertainty.

Table 12.2: Central Expected Limits with sources of systematic uncertainty removed.

Removed Uncertainty	Expected Central Upper Limit
JER	10.6
JES	10.5
btag light	10.1
btag heavy	11.4
PU	10.5
$t\bar{t}$ ME Scale	11.8
$t\bar{t}$ Hadronization Scale	10.8
$t\bar{t}$ Generator Choice	10.5
$t\bar{t}t\bar{t}$ ME Scale	9.5
$t\bar{t}t\bar{t}$ $t\bar{t}$ Heavy Flavor re-weighting	10.8

Chapter 13

Conclusions

A search for events containing four top quarks has been performed using the entire 2015 CMS dataset with $\sqrt{s} = 13$ TeV. The analysis focuses on the $\mu\mu$, μe, and ee final states and consists of three stages. First, a baseline selection is used to broadly select signal events while suppressing backgrounds. Secondly, to further enhance sensitivity to four top production, an event classification scheme based on a BDT algorithm is defined. This exploits the differences in *event activity*, *event topology*, *b-content*, *lepton content*, and *top-content* to discriminate between signal and background. Events are then separated into exclusive jet categories in each channel and a simultaneous fit is made to the distributions. Combining the $\mu\mu$, eμ, and ee final states yields a combined 95% CL upper limit on the four top production cross-section in the of $14.9\times\ \sigma^{SM}_{t\bar{t}t\bar{t}}$ with an expected upper limit of $22.3^{+16.2}_{-8.4}\times\ \sigma^{SM}_{t\bar{t}t\bar{t}}$.

By combining the results of this analysis with those from a parallel analysis in the single lepton channel, the 95% CL upper limit on the four top production cross-section is improved and a results in a combined upper limit of $10.2\times\ \sigma^{SM}_{t\bar{t}t\bar{t}}$ observed with $10.8^{+6.7}_{-3.8}\times$ $\sigma^{SM}_{t\bar{t}t\bar{t}}$ expected.

Bibliography

[1] Computer graphic of LHC in the tunnel. Le futur collisionneur LHC dans le tunnel du LEP. Feb 1996.

[2] First combination of Tevatron and LHC measurements of the top-quark mass. 2014.

[3] Performance of b-tagging algorithms at 13 TeV. Technical Report CMS-AN-2016/036, CERN, Geneva, 2016.

[4] R. et al Aaij. Observation of $j/\psi p$ resonances consistent with pentaquark states in $\Lambda_b^0 \to j/\psi K^- p$ decays. *Phys. Rev. Lett.*, 115:072001, Aug 2015.

[5] S. et al Abachi. Observation of the top quark. *Phys. Rev. Lett.*, 74:2632–2637, Apr 1995.

[6] M. Aldaya, T. Arndt, C. Diez Pardos, A. Harb, J. Hauk, J. Kieseler, and A. Meyer. Trigger and lepton efficiencies for topanalyses in runii. CMS Note 2016/025, 2016.

[7] J. Alwall, R. Frederix, S. Frixione, V. Hirschi, F. Maltoni, O. Mattelaer, H. S. Shao, T. Stelzer, P. Torrielli, and M. Zaro. The automated computation of tree-level and next-to-leading order differential cross sections, and their matching to parton shower simulations. *JHEP*, 07:079, 2014.

[8] Johan Alwall, Michel Herquet, Fabio Maltoni, Olivier Mattelaer, and Tim Stelzer. MadGraph 5 : Going Beyond. *JHEP*, 06:128, 2011.

[9] Chiara Arina et al. A comprehensive approach to dark matter studies: exploration of simplified top-philic models. 2016.

[10] LHC Higgs Combination Group ATLAS, CMS. Procedure for the LHC Higgs boson search combination in Summer 2011. Technical Report CMS-NOTE-2011-005. ATL-PHYS-PUB-2011-11, CERN.

[11] Roger Barlow and Christine Beeston. Fitting using finite monte carlo samples. *Computer Physics Communications*, 77:219, 1993.

[12] G. Bevilacqua and M. Worek. Constraining BSM Physics at the LHC: Four top final states with NLO accuracy in perturbative QCD. *JHEP*, 07:111, 2012.

[13] E. Boos and L. Dudko. The Single Top Quark Physics. *Int. J. Mod. Phys.*, A27:1230026, 2012.

[14] Leo Breiman, Jerome Friedman, R. A. Olshen, and Charles J. Stone. *Classification and regression trees*. Chapman and Hall/CRC, 1984.

[15] Maximilien Brice. First half of CMS inner tracker barrel. Oct 2006.

[16] Maximilien Brice. People at work on the CMS detector open during the LS1. Apr 2013.

[17] CMS BTV-POG. Methods to apply b-tagging efficiency scale factors. Technical Report , 2013.

[18] Giacomo Cacciapaglia, Haiying Cai, Aldo Deandrea, Thomas Flacke, Seung J. Lee, and Alberto Parolini. Composite scalars at the LHC: the Higgs, the Sextet and the Octet. *JHEP*, 11:201, 2015.

[19] Matteo Cacciari, Gavin P. Salam, and Gregory Soyez. The anti-k_t jet clustering algorithm. *JHEP*, 04:063, 2008.

[20] Matteo Cacciari, Gavin P. Salam, and Gregory Soyez. FastJet User Manual. *Eur. Phys. J. C*, 72:1896, 2012.

[21] Samuel Calvet, Benjamin Fuks, Philippe Gris, and Loic Valery. Searching for sgluons in multitop events at a center-of-mass energy of 8 TeV. *JHEP*, 04:043, 2013.

[22] Qing-Hong Cao, Shao-Long Chen, and Yandong Liu. Probing Higgs Width and Top Quark Yukawa Coupling from $t\bar{t}H$ and $t\bar{t}t\bar{t}$ Productions. 2016.

[23] Jean-Luc Caron. Magnetic field induced by the LHC dipole's superconducting coils.. Champ magnetique cree par les bobines superconductrices des aimants dipolaires du LHC. AC Collection. Legacy of AC. Pictures from 1992 to 2002., Mar 1998.

[24] S Chatrchyan et al. Performance of CMS Hadron Calorimeter Timing and Synchronization using Test Beam, Cosmic Ray, and LHC Beam Data. *JINST*, 5:T03013, 2010.

[25] Serguei Chatrchyan et al. Determination of jet energy calibration and transverse momentum resolution in CMS. *JINST*, 6:P11002, 2011.

[26] CMS. Cms miniaod documentation. Technical Report , 2015.

[27] CMS. Utilities for accessing pileup information for data. Technical Report , 2015.

[28] CMS Collaboration. CMS technical design report, volume II: Physics performance. *J. Phys. G*, 34:995–1579, 2007.

[29] CMS Collaboration. Commissioning of the particle-flow event reconstruction with the first LHC collisions recorded in the CMS detector. CMS Physics Analysis Summary CMS-PAS-PFT-10-001, 2010.

[30] CMS Collaboration. Identification of b quark jets at the CMS Experiment in the LHC Run 2. CMS Physics Analysis Summary CMS-PAS-BTV-15-001, 2016.

[31] CMS Collaboration. Search for standard model four top quark production at 8 TeV in the lepton + jets channel. 2013.

[32] CMS Collaboration. Measurement of the cross section ratio $t\bar{t}b\bar{b}/t\bar{t}jj$ using dilepton final states in pp collisions at 13 TeV. CMS Physics Analysis Summary CMS-PAS-TOP-16-010, 2016.

[33] Micha Czakon, Paul Fiedler, and Alexander Mitov. Total Top-Quark Pair-Production Cross Section at Hadron Colliders Through $O(\alpha_S^4)$. *Phys. Rev. Lett.*, 110:252004, 2013.

[34] Cinzia De Melis. The CERN accelerator complex. Complexe des acclrateurs du CERN. Jul 2016. General Photo.

[35] Daniel Dominguez. Standard Model. Le modle standard. Mar 2015. General Photo.

[36] Otilia Ducu, Lucien Heurtier, and Julien Maurer. LHC signatures of a Z' mediator between dark matter and the SU(3) sector. *JHEP*, 03:006, 2016.

[37] H. Jerome Friedman. Recent advances in predictive (machine) learning. *Journal of Classification*, 23:175, 2006.

[38] CMS Top group. Top reference selections for analyses using 2012 data. Technical Report , 2013.

[39] Laurent Guiraud and Patrice Loez. CMS lead tungstate crystals. Nov 2000.

[40] Andreas Hocker et al. TMVA - Toolkit for Multivariate Data Analysis. *PoS*, ACAT:040, 2007.

[41] Vardan Khachatryan et al. Measurement of $t\bar{t}$ production with additional jet activity, including b quark jets, in the dilepton decay channel using pp collisions at $\sqrt{s} = 8\,\text{TeV}$. *Eur. Phys. J. C*, 76:379, 2016.

[42] Vardan Khachatryan et al. Search for new physics in same-sign dilepton events in proton-proton collisions at $\sqrt{s} = 13$ TeV. 2016.

[43] L. Moneta, K. Belasco, K. S. Cranmer, A. Lazzaro, D. Piparo, G. Schott, W. Verkerke, and M. Wolf. The RooStats Project. In *13^{th} International Workshop on Advanced Computing and Analysis Techniques in Physics Research (ACAT2010)*. SISSA, 2010. PoS(ACAT2010)057.

[44] K. A. Olive et al. Review of Particle Physics. *Chin. Phys.*, C38:090001, 2014.

[45] CMS EGM POG. Instructions for applying electron and photon id. Technical Report , 2015.

[46] CMS Muon POG. Cms muon id run2 wiki. Technical Report , 2015.

[47] Torbjörn Sjöstrand, Stephen Mrenna, and Peter Skands. Pythia 6.4 physics and manual. *JHEP*, 05:026, 2006.

[48] Torbjörn Sjöstrand, Stephen Mrenna, and Peter Skands. A brief introduction to pythia 8.1. *Computer Physics Communications*, 178:852, 2008.

[49] Manuel Toharia and James D. Wells. Gluino decays with heavier scalar superpartners. *JHEP*, 02:015, 2006.

Appendix A

Study on Corrections to Jet Activity

During the course of the analysis, it became known that an error was made in the generation of the MC simulation samples used. Pythia8 was used to calculate the parton showering simulation prior to the digitization and reconstruction of the event by the CMS generator group. When the Pythia8 calculations were made, an incorrect value of the strong coupling $\alpha_S = 0.137$ was used to determine the profile of the initial state radiation, resulting in harder simulated gluon emission in the showering step. This is manifested in our simulation samples in the presence of extra ISR jets and a slight increase of the energy of ISR jets present in the events. This upsets the data/simulation agreement the further one looks out into the tails of jet spectra where the amount of simulated events exceeds the data as seen in Fig. A.1.

This analysis is particularly vulnerable to this choice as we are looking far out in the tail of the $t\bar{t}$ sample. Requiring a minimum of 4 jets and an HT of at least 500 GeV preferentially selects events where there are both more and slightly harder jets. Thus, a correction needs to be made in order to have a good model of the data.

A.1 Behrend's Scaling

In the grand scheme, the motivation for a correction is less important than that the simulation properly models the data. As a first attempt we decided to use a Behrend's

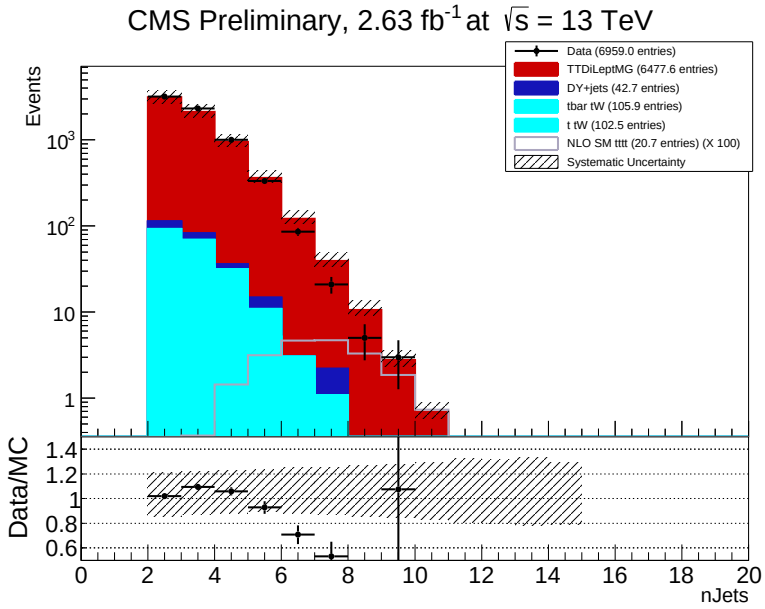

Figure A.1: Uncorrected jet multiplicity with relaxed pre-selection.

style scaling of the jet multiplicity. This operates on the assumption that for each extra jet in the event beyond the tree level diagram, the rate for that number of jets should be further suppressed by a factor of α_S.

In practice there are other factors present, but the hypothesis that the jet multiplicity spectrum should vary approximately as a power law until higher order corrections begin to take over is the essence of Behrend's scaling. To this end, we performed independent fits of power laws, such as in Eq. A.1, to the jet multiplicity spectra of the data and the $t\bar{t}$ simulation. We can then derive a scale factor to apply to the simulation as a function of jet multiplicity to attempt to correct the mismatch.

$$f(x) = p_0 \cdot p_1^{(x-5)} \tag{A.1}$$

For the $t\bar{t}$ sample used, MadGraph5 was used to generate the LHE of the events. Beyond the tree level, MadGraph also generates the multi leg +1 jet, +2 jets, and +3 jet events. Beyond this point, additional simulated jets come from the Pythia8 showering. Thus the scaling really only need be applied in the 6 jet and higher bins. With this hypothesis, we set the 'zero' of the fit to the 5 jet bin to ensure that the last correctly modelled bin is where the first step of α_S was measured.

In order to ensure good convergence of the fit, the requirements on the pre-selection for the analysis were relaxed to only requiring 2 jets and removing the HT requirement to reduce statistical fluctuations and uncertainty. The first round of fits can be seen in Fig. A.2. The uncertainty on the Data is purely statistical based on the number of events in each bin, where the uncertainty on the simulation is taken from the scale systematic uncertainty as it is the dominant source of systematic uncertainty.

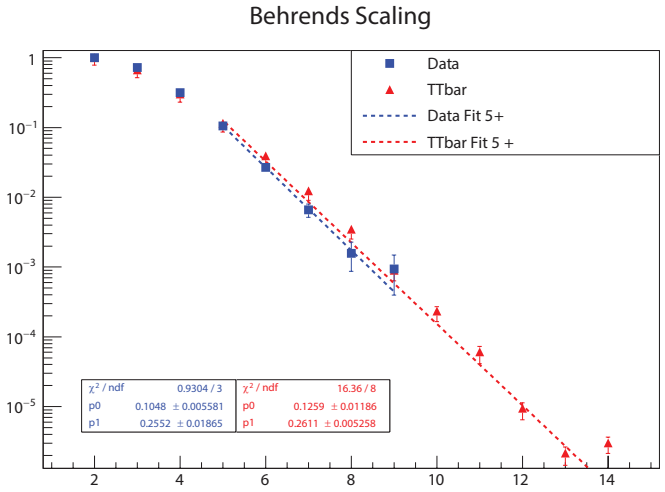

Figure A.2: First pass at fits for Behrens scaling.

In order to ensure that the fits merged smoothly into the MadGraph multileg region, the coefficient parameter was fixed to an average of the fitted parameters p_0 as shown in A.2. This resulted in the new fit function:

$$g(x) = 0.11535 \cdot p_0^{(x-5)}. \tag{A.2}$$

. This function was then again fit and the resulting functions were used to derive the scale factor,

$$SF_{behrens}(x) = \frac{g_{Data}(x)}{g_{MC}(x)} = \frac{p_{0,Data}^{(x-5)}}{p_{0,MC}^{(x-5)}}, \tag{A.3}$$

which is shown in green in Fig. A.3.

Applying this scale factor to the $t\bar{t}$ simulation samples results in the multiplicity spectrum seen in Fig. A.4. The agreement between data and simulation is considerably

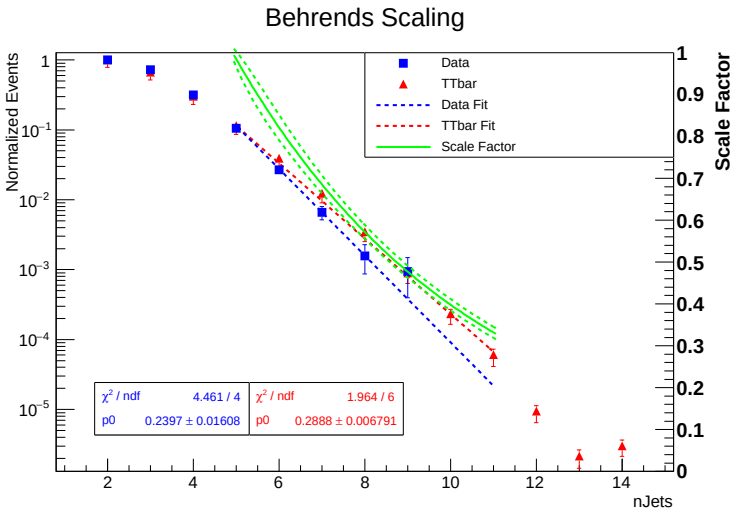

Figure A.3: Behrens scaling fits and scale factor

better and the corrected simulation is in agreement with the data to within the systematic uncertainties.

A.2 α_S Tuning Study

Another possible method of correction is attacking the problem a bit more directly. A study carried out in the CMS TOP analysis group was presented at the April 19, 2016 meeting. This compared the jet multiplicity spectra in dileptonic ttbar of several samples which had been tuned to use different values of α_S in the Pythia parton showering. These samples were compared to the 8 TeV data to find which tune best represented the multiplicity observed in that data. The best tune was observed to be one with a value of $0.113^{+0.012}_{-0.010}$ where the errors are derived from the upper and lower envelope on the data's statistical error. Starting from this result, a ratio of the event yields in a particular jet bin between this tune and a sample using the default value for α_S can be used as a scale factor to correct for the discrepancy between simulation and data. The plot of the ratio can be seen in figure A.5. This method has been documented in reference [41].

The purpose of applying a correction is to correct the spectrum of the jets resulting from ISR. Since the ratios in figure A.5 were derived for the single lepton channel, where

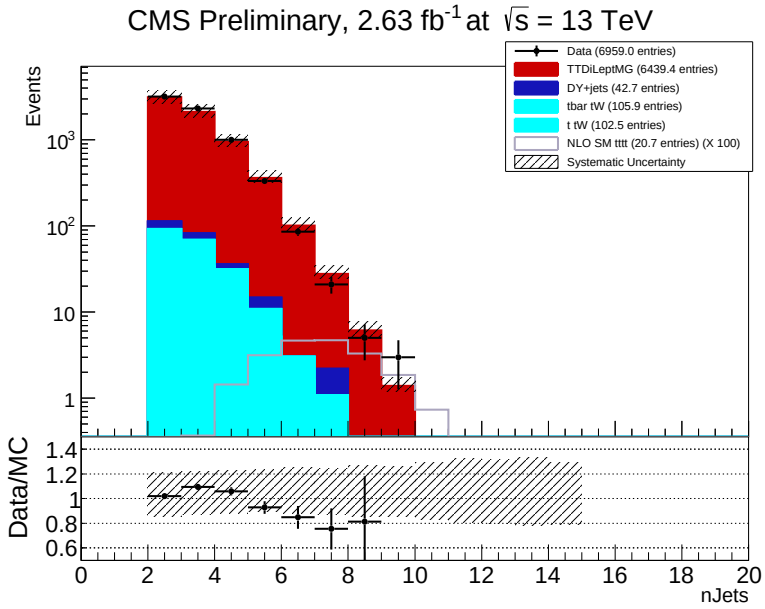

Figure A.4: Uncorrected jet multiplicity with relaxed pre-selection.

the number of final state partons is larger than in the dilepton case, an adjustment of the correction is necessary. In the single lepton case, the parton shower calculation begins at the fifth jet. Whereas, for the dilepton channel, it begins at the third jet. Thus, the ratio in the 5 jet bin shown in figure A.5 should be applied to events with 3 jets in dileptonic ttbar. Similar considerations can be made for other samples simulated using the same assumptions based on their phenomenology.

Since the ratios seen in figure A.5 are of the default tune to the preferred tune, the actual scale factor to be applied should be the reciprocal of the ratio shown. After applying this correction, the corrected jet spectra of samples used in this analysis can be seen in figure A.6.

The systematic uncertainty for this correction can be estimated from the uncertainty on the value of α_S used for the tune assuming a power law behavior.

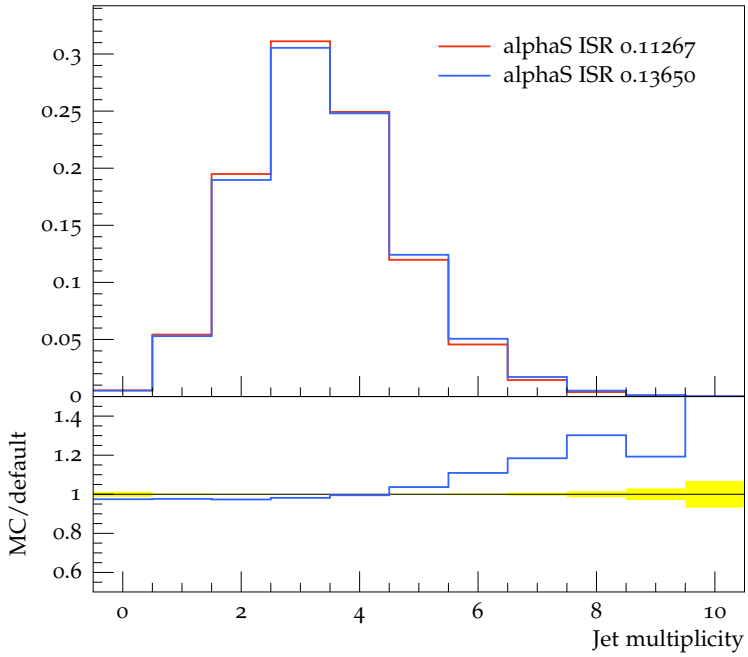

Figure A.5: Ratio of the $\alpha_S = 0.137$ tune to the $\alpha_S = 0.113$ tune.

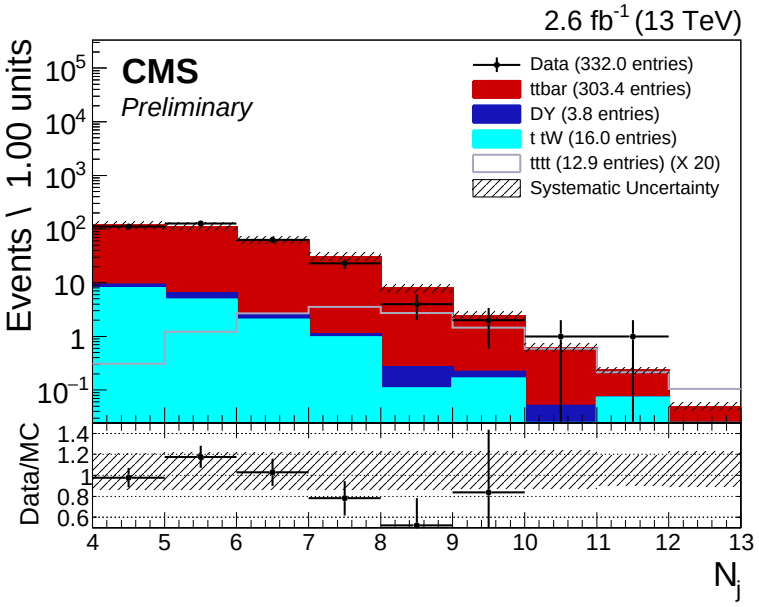

Figure A.6: Jet multiplicity spectrum after the α_S correction.

Appendix B

Study on the choice of Boosting Algorithm and Treatment of Negative Weights in Training

B.1 A Primer on NLO Generation and MVA

For this analysis, the signal sample was generated using the aMC@NLO generator package which is capable of generating events to the next to leading order QCD precision. Because the $t\bar{t}t\bar{t}$ process is already a higher order process, the number of possible NLO diagrams can highly impact the overall cross section calculation as well as the event kinematics. Thus, the use of the NLO sample is expected to increase performance of the analysis through better modeling of the signal process. However, the use of aMC@NLO comes with a downside.

As one calculates higher order perturbative corrections to cross sections, one must take into account terms, that cancel out other term such that the cross section converges. The aMC@NLO package implements this by assigning a negative weight to some of the events it generates. These events are designed to cancel out other events, leaving the differential cross section for those pieces of phase space correctly simulated. This results in the 'effective size' of an aMC@NLO sample being reduced to

$$N_{eff} = N_{pos} - N_{neg} = N_{total} - 2 \cdot N_{neg}. \tag{B.1}$$

and the scaling factor for scaling simulation to data being changed to

$$SF_\sigma = \frac{L_{Data}}{L_{MC,eff}} = \frac{L_{Data}}{N_{MC,eff} \cdot \sigma_{MC}} = \frac{L_{Data}}{(N_{total,MC} - 2 \cdot N_{neg,MC}) \cdot \sigma_{MC}}. \tag{B.2}$$

This reduction factor means that one must generate more NLO events to cover the same luminosity than one would leading order events. While the time required to generate the samples is possibly large, it is not outside the scope of the computing resources provided by CMS.

The other implication of the presence of negative weights comes in the training of Boosted Decision Trees. Nominally in CMS analyses involving BDTs, the AdaBoost algorithm is used to boost the event weights between nodes and trees. However in the presence of negative weights, the AdaBoost algorithm will fail to produce the desired effect due to the use of exponential functions in determining the error function of the boosting. Several possible solutions have been proposed.

First, one could use gradient boosting as the functional form of the boosting should be transparent to the presence of a negatively weighted event. The negatively weighted events will be subtracted from the output classifier spectrum effectively reducing the size of the training and test samples.

Second, one could train only on positive events. This would present a false representation of the signal sample feature space to the training as well as reduce the events available for training and testing. It is unclear if the incorrect proportion of higher order events in a training sample would make a significant difference to the classifier as it would still be using events with valid kinematics to evaluate the node purity at each step.

Third, one could ignore the weighting information entirely. This would again present an incorrect representation of the feature space, but it would provide the maximal amount of training events to the BDT.

The discussion of which method is the most correct is ongoing inside CMS. It is clear that each method has merits, but for the purpose of this analysis, we performed an empirical study to determine the strategy we would use. Given that we do not have access to arbitrary signal generation, arguments about the relative size of the training sample between strategy are relevant and provide motivation for examining those strategies.

B.2 MVA Study

For this study, we trained 3 BDTs using the following strategies:

1. Gradient boosting taking into account negative weighting information in training and testing

2. Gradient boosting ignoring negative weighting information in training and testing

3. AdaBoost boosting ignoring negative weighting information in training and testing

It was decided that if we were going to ignore the negative weight information, than there was no reason to not include them in the training sample and thus the second strategy in section B.1 was not included in the study. Additionally, if one was to ignore the negative weight information than there is no reason to not examine using AdaBoost. Strategy 1 is referred to as *GradNeg*; strategy 2 as *GradBoost*; and strategy 3 as *AdaBoost*. These tags will be referenced in plots in this section.

Each BDT was trained with the same set of input features, which are described in Chapter 9.

The three MVA strategies were trained using the same sample of events to train and test the BDTs. The response of the signal and background samples as well as the ROC curves for the derived classifiers for each strategy are shown in Figures B.1 through B.3.

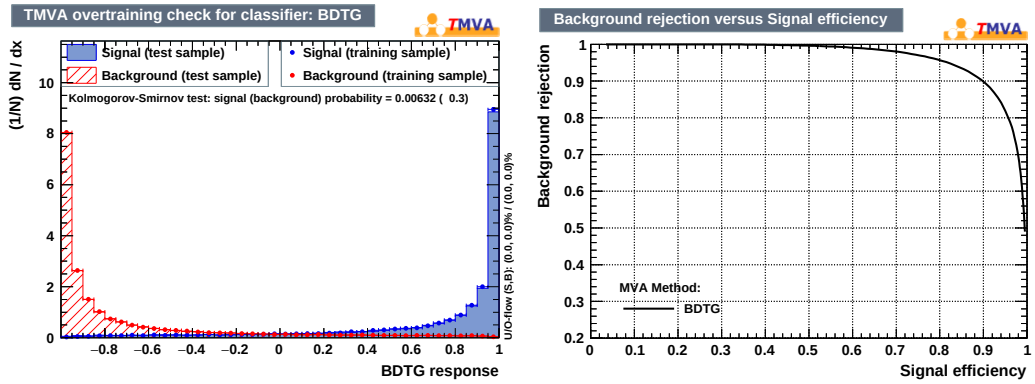

Figure B.1: Classifier response and ROC curve for the GradNeg strategy.

Looking at the Figures B.1 through B.3 with the eye alone, it seems like the GradBoost strategy slightly outperforms the other classifiers. However, BDTs are complicated objects and their interaction with a limit setting process even more complicated. Thus, each

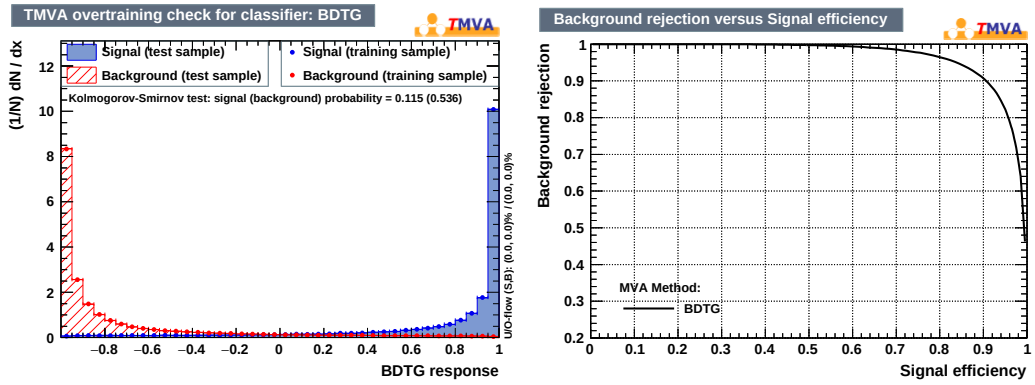

Figure B.2: Classifier response and ROC curve for the GradBoost strategy.

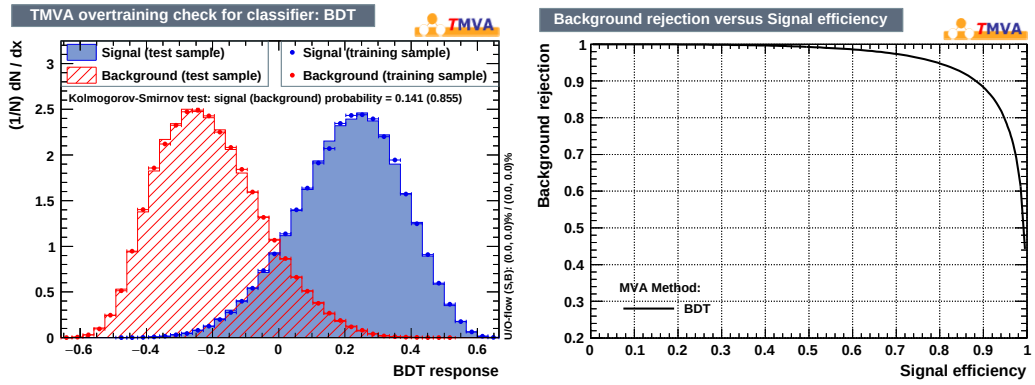

Figure B.3: Classifier response and ROC curve for the AdaBoost strategy.

of these classifiers was evaluated for each simulation sample used in the analysis and expected limits were extracted for each of them using the same jet multiplicity categorization methodology described in Chapter 11. The expected limits are tabulated in Table B.1.

While the GradNeg strategy performed the best when it came to the central limit, the differences between each strategy is very small and entirely within uncertainty of each other and thus deserves further study. Additionally, the overtraining test indicates that the GradNeg BDT is overtrained and that the BDT parameters need to be re-tuned. Based on these observations, the AdaBoost strategy was chosen for this analysis given the lack of available training events to ensure that the GradNeg BDT was not overtrained.

Strategy	Inclusive	Uncertainty	Categorized	Uncertainty
GradNeg	19.6	$+11.7 - 7.1$	18.1	$+10.8 - 6.5$
GradBoost	20.1	$+12.0 - 7.1$	18.2	$+10.7 - 6.3$
AdaBoost	20.8	$+12.2 - 7.4$	19.1	$+11.4 - 7.9$

Table B.1: Extracted expected limits for both inclusive and N_{jet} categorized strategies.

Appendix C

Tests on the Goodness of the Fit

In order to test the goodness of the fit during the limit setting, an examination of the post-fit nuisance parameters is performed.

A maximum likelihood fit is performed first for the dilepton channel to test the inputs to the fitting algorithm. In Figure C.1, the best fit values for the nusiance parameters for this check are shown. The best fit values for the full four top single lepton and dilepton combination fit are shown in Figure C.2.

The post-fit values of each of the nuisance parameters falls within the prefit uncertainty indicating that the sizes of the uncertainties are appropriate with respect to the data. Some parameters, such as the hadronization scale uncertainty and the $t\bar{t}$ generator uncertainty, have had their uncertainties significantly reduced post-fit. This indicates that the data is highly constrained by these parameters and can not deviate significantly from the best fit values. This is expected of these parameters as they were already expected to have a large impact on the fit. Additionally, while the choice of $t\bar{t}t\bar{t}$ matrix element scale has a large effect on the best fit central value of the limit setting, the goodness of the fit is stable across the whole width of the pre-fit uncertainty on this parameter indicating once again, that $t\bar{t}$ uncertainties are the most sensitive in the fit.

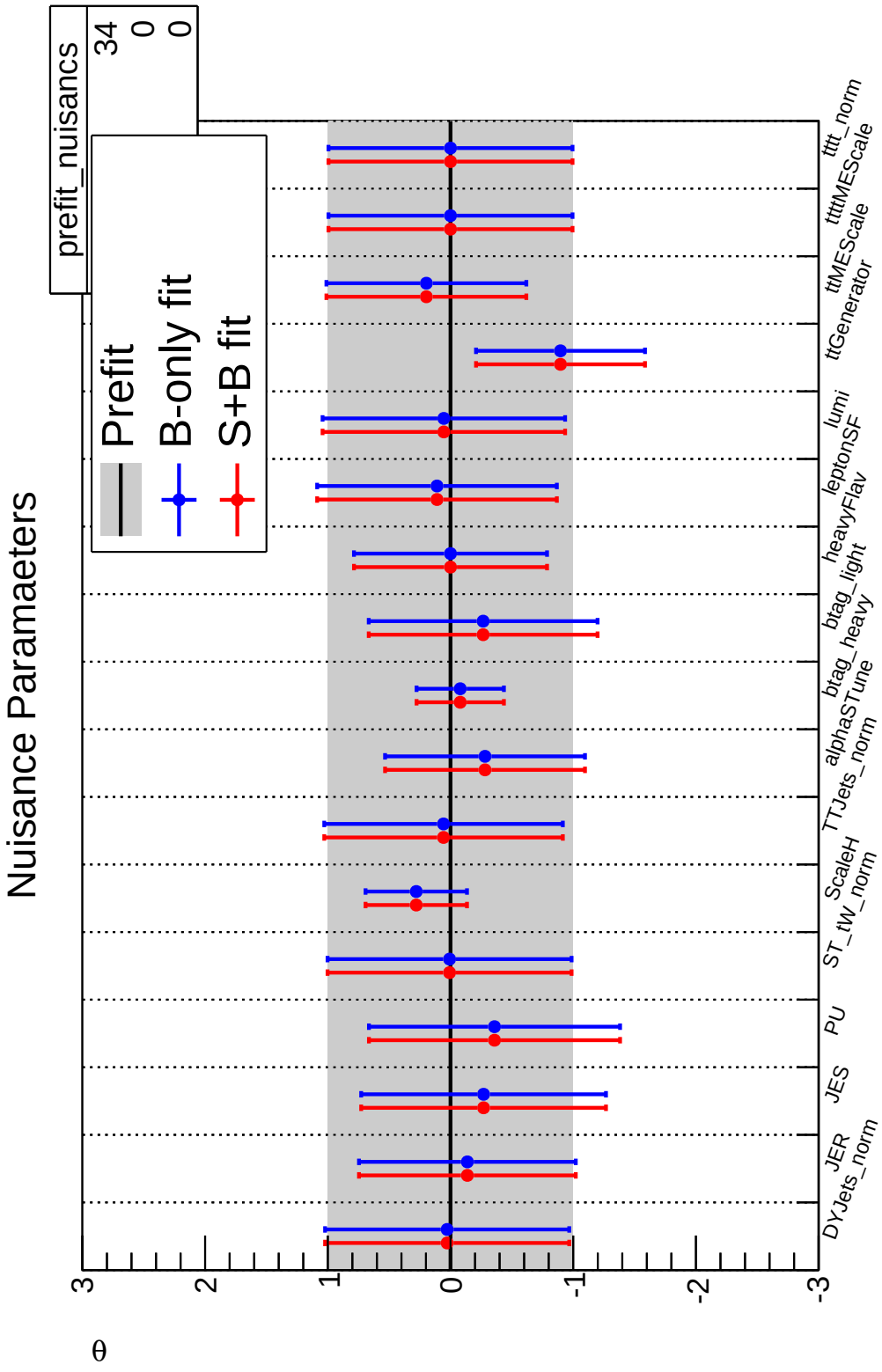

Figure C.1: Pre and post-fit nuisance parameters for the full dilepton channel combination.

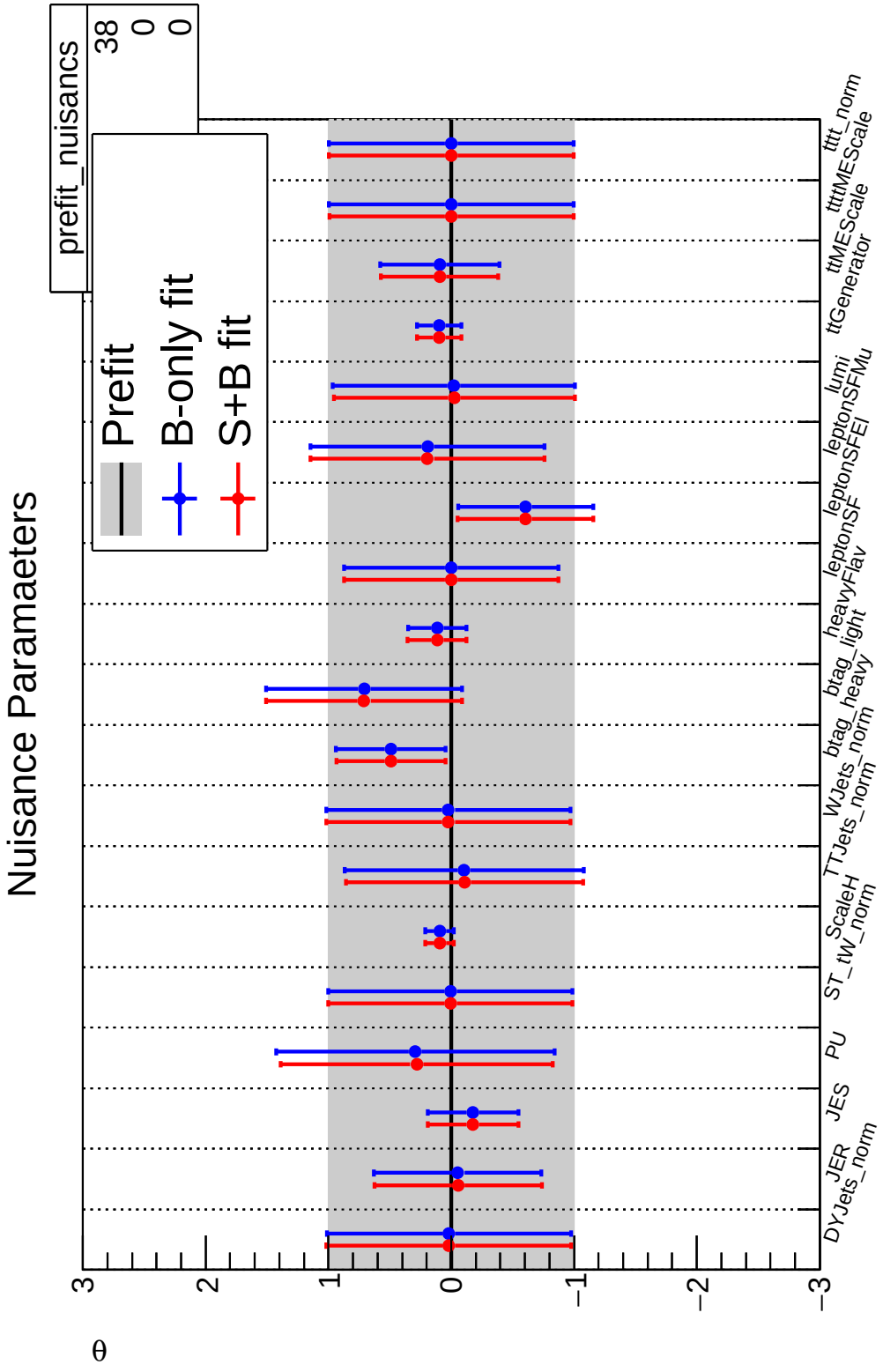

Figure C.2: Pre and post-fit nuisance parameters for the full four top single lepton and dilepton combination.

Appendix D

Study of the Size of Shape Systematic Uncertainties

This appendix catalogs the shapes of the sources of systematic uncertainty coming from the $t\bar{t}$ background. The shapes are shown in Figures D.1 through D.4. The Parton Shower scale shape and Generator Choice shapes deviate the most from the nominal and thus are the dominant sources of uncertainty from $t\bar{t}$. However, the Matrix Element scale shapes form the largest envelope and thus they are the best candidate to use for systematic uncertainty bands on plots. The plots are derived from the μe final state baseline selection but each channel behaves in the same ways. Descriptions for how these uncertainties are calculated can be found in Chapter 10.

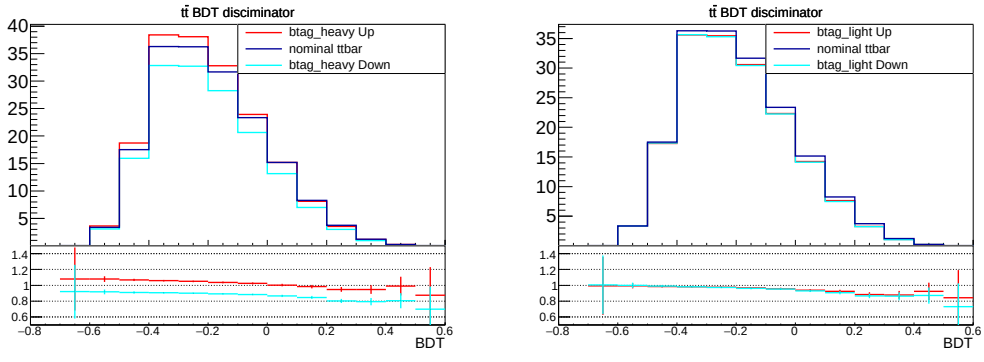

Figure D.1: Heavy (left) and Light (right) btagging uncertainties (up/down) on the BDT classifier distributions from $t\bar{t}$ samples.

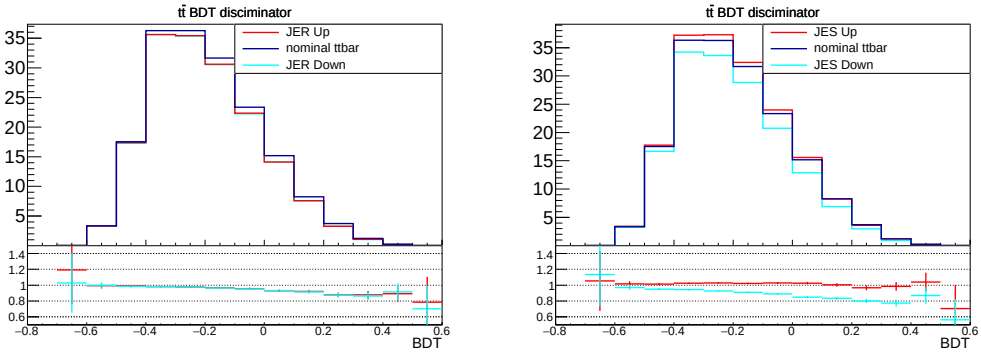

Figure D.2: JER (left) and JES (right) uncertainties (up/down) on the BDT classifier distributions from $t\bar{t}$ samples.

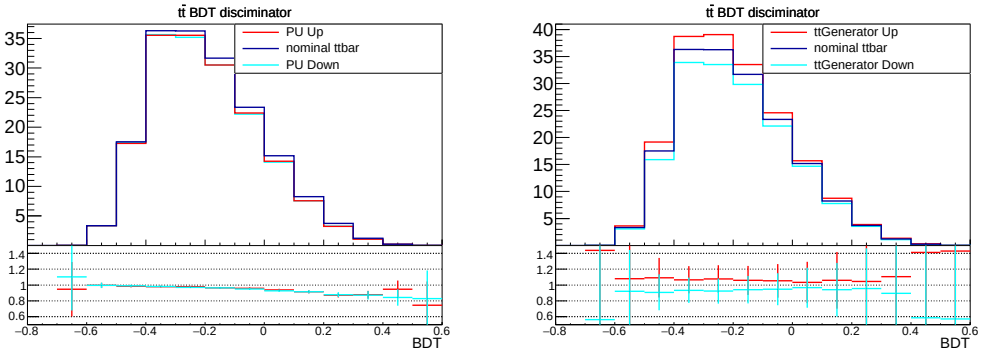

Figure D.3: PU (left) and Generator Choice (right) uncertainties (up/down) on the BDT classifier distributions from $t\bar{t}$ samples.

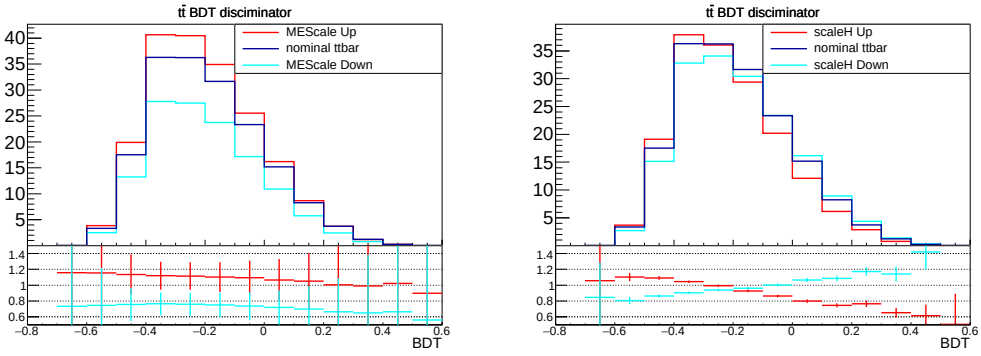

Figure D.4: Matrix Element Scale (left) and Parton Shower Scale (right) uncertainties (up/down) on the BDT classifier distributions from $t\bar{t}$ samples.

Appendix E

B-tagging Scale Factor Uncertainty

The so-called 'CSV reshaping' approach to the b-tagging systematic variation accommodates multiple sources of uncertainty[3]. For this study, individual components were added in quadrature and symmetrized for comparison with nominal b-tagging systematic uncertainty. JES component of the CSV reshaping systematic was not included because it is not available in the nominal approach and is correlated with the dedicated JES systematics. The effect on the event-level BDT distribution in multiple b-tag and jet multiplicity categories is illustrated in Figures E.1 and E.2 for $t\bar{t}$ and $t\bar{t}t\bar{t}$ samples, respectively. It was observed that the nominal approach reasonably accounts for the effects of imperfect modelling of the shape of the CSV discriminant distribution if the size of heavy-flavour and light-flavour components of uncertainty are inflated by a factor of 2.

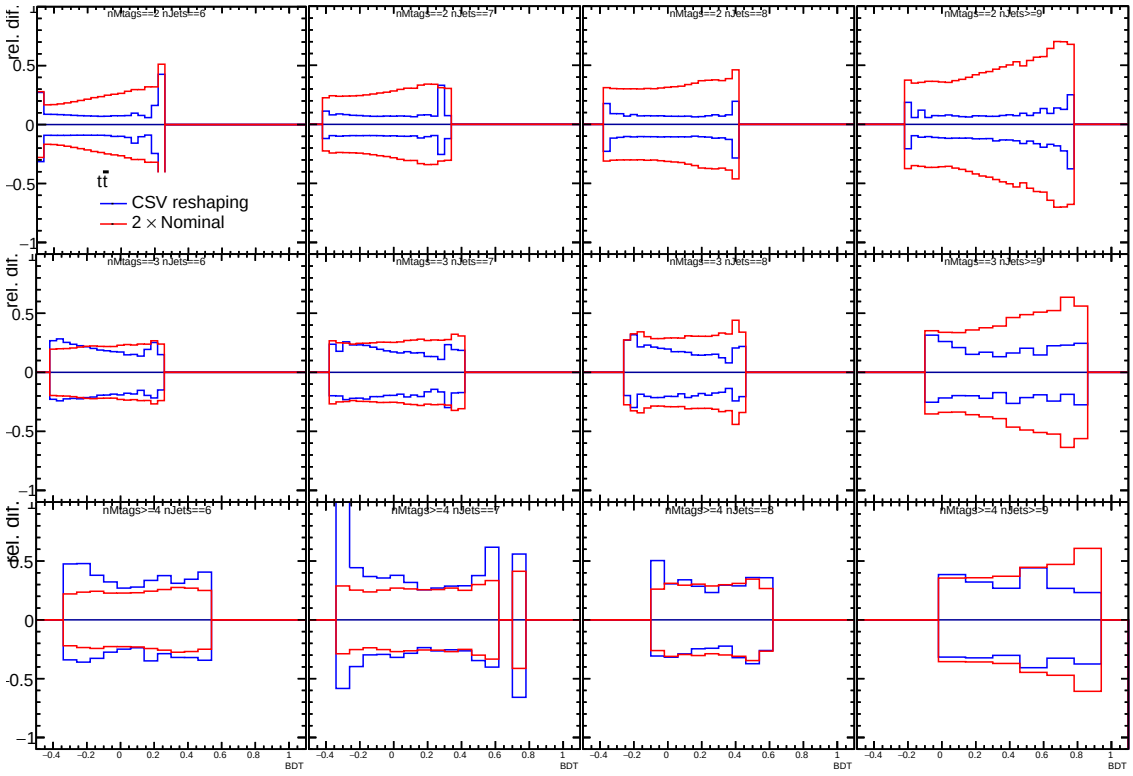

Figure E.1: Comparison of the effect of nominal (red) and 'CSV reshaping' (blue) systematic variations of b-tagging scale factors on single lepton $t\bar{t}$ event-level BDT distribution split into N_j and N^M_{tags} categories with light flavor uncertainties inflated.

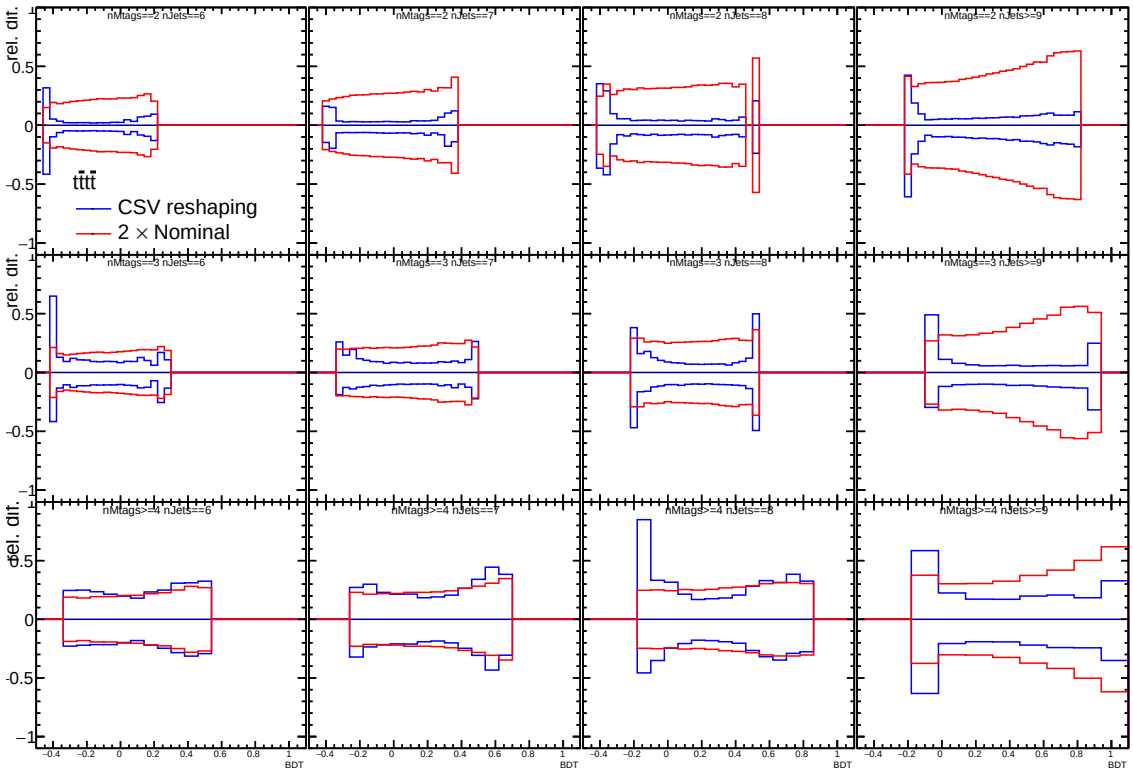

Figure E.2: Comparison of the effect of nominal (red) and 'CSV reshaping' (blue) systematic variations of b-tagging scale factors on single lepton $t\bar{t}t\bar{t}$ event-level BDT distribution split into N_j and N_{tags}^{M} categories with heavy flavor uncertainties inflated.

Appendix F

Muon Endcap Upgrade

During the Long Shutdown 1 (LS1) the CMS Endcap Muon (EMU) system underwent a major upgrade. During the original construction of CMS, the outermost ring of CSCs, ME4/2, was not completed due to constraints on time and budget. The omission of these chambers only reduced the muon system performance by a few percent but it did leave a lack of redundancy in the detector's fiduciary volume. Leading up to LS1, the 72 new CSCs making up ME4/2 were constructed at CERN. These chambers were then installed in the CMS cavern and commissioned during LS1 and have been actively taking data since the LHC restart in 2015. While at CERN, I played an integral role in the construction, characterization, installation, and commissioning of these new CSCs.

F.1 Cathode Strip Chambers Construction

Based on the multi-wire proportional counter technology, each chamber is constructed from 7 panels. These panels are the basic element of the chambers' mechanical structure and are stacked creating six detection gaps. The panels are constructed from a polycarbonate core bonded on both sides to a 1.6 mm FR4 fiberglass skin. These skins are commercially produced and are laminated on one side with a 34 μm layer of copper. The skins are bonded to the core with the copper facing outward.

The panels are then separated into 4 categories: Inner Cathode (IC), Lower Cathode (LC), Upper Cathode (UC), and Anode (A). These categories determine the details of the milling artwork and their placement in the panel stack. Each chamber has a single UC, a single LC, two IC, and 3 anode panels. The anode panels have wires attached to each

side of the panel which collect the anode signals. The UC, IC, and anode panels have strips milled into one of their sides. Thus, when stacked, each detection gap has strips on one side of the gap, wires in the middle, and a continuous ground on the other side of the gap. The LC panel have no milling as they are a continuous ground on one side and the chamber exterior on the other.

The Cathode Panels have gap bars fixed around their periphery. These are bonded down to the copper cathodes with an epoxy that acts as part of the gas seal on the sensing gap. These bars define the full gap between the cathodes and provide the proper separation of the panels. Inside these gap bars on the long edges of the panels, insulating guard strips are glued down to the panel to insulate the solder joints on the anode panels from the cathodes.

Anode panels are wound with sensing wires which are then soldered and epoxied to wire fixation bars which are bonded to the anode panels. The primary mechanical contact is from the epoxy so that possible weaknesses in the wired exposed during soldering, such as compromising the wire jacket, are not held by the solder. This helps to ensure the proper tensioning of the sensing wires over the life of the chamber.

The anode panels then have a suite of protection boards, capacitors, and resistors soldered onto particular traces to prepare them for high voltage testing. Each anode panel is tested up to a voltage of 4.5 kV in air to ensure that no contaminants have been introduced to either the panel or wires that will contribute to significant leakage current once the chamber is completely assembled. This is extremely delicate as the voltage on the wires is near that of the breakdown voltage of the gap in air. Special skills and training were required to perform the high voltage tests while ensuring the safety of both the tester and the panel.

Once the electronic properties of the wires have been confirmed, the pitch and tension of each wire must be measured to ensure it is within design tolerance as well as for record keeping. This is accomplished by an automated tension meter that electrostatically induces a vibration in each individual wire and then measures the frequency of the base harmonic through a device similar to an electric guitar pickup. High resolution cameras precisely placed at each end of a wire compare their position relative to the panel to ensure that the wire pitch is acceptable.

Once all 7 panels are shown to be inside design parameters, the chamber is stacked and sealed. Pressure tests are performed to ensure that the gas seals are tight and there

will be no significant leakage of the sensing gasses once they populate the chamber. This is important not only to maintain the effectiveness of the chambers but also to lessen the environmental impact of the whole CSC system as CF_4 (one of the gasses used in the CSC gas mixture) is a recognized greenhouse gas. Next the chamber is energized and the leakage current for each layer is checked. If any of theses tests are failed during assembly, the chamber must be disassembled, cleaned, checked, and reassembled.

Once assembly tests have been performed the chamber is hooked up to high voltage and left energized for a period of ≈ 1 month. This allows the chamber sufficient time to reach it's ground state energy and ensures that there is no energy buildup in the chamber that will result in arcing that could damage the chamber or degrade its performance.

The final step in the assembly of a CSC is the integration of the raw chamber with all the on-board electronics. Electronic boards controlling power distribution, front end readout, and signal timing are fixed to the chamber and cabled. The chamber is then hooked up to a basic DAQ system which performs connectivity, gain performance, and electronic integrity tests before the chamber is designated ready for installation in the CMS cavern.

The assembly process for all the ME4/2 chambers took place over roughly two years leading up to and during the start of the LHC Long Shutdown 1. During this time, I participated in each stage of the chamber assembly and testing but was specially trained to be responsible for the assembly, winding, and testing of the anode pannels.

F.2 Cathode Strip Chamber Installation

The process of effecting all the upgrades planned by CMS during LS1 was a logistically complicated process requiring the harmonious operation of many teams from many different subdetector system groups. Prior to the window that was scheduled for the installation of the ME4/2 chambers, all required cabling and services had to be prepared so that the installation of the chambers could proceed as efficiently and quickly as possible. A team of mostly graduate students, lead by myself, prepared and laid all the required cabling (HV power, LV power, readout, and timing control) and assisted in the preparation of the gas and cooling services.

Once the installation window arrived, I joined the team that installed the ME4/2 chambers in the CMS cavern. This process involved integrating with crane operator tech-

nicians and driving a cherry picker to guide each chamber to its position on the endcap and then securing it in place. This process was very involved and proceeded at a rate of between 7 and 10 chambers per day on average. I received special training in order to both work in the CMS cavern as well as drive a cherry picker in the cavern's confined space. A photo of the installation process, involving two teams in two cherry pickers, can be seen in Figure F.1 and a close up of one team fixing a chamber end to the disk can be seen in Figure F.2.

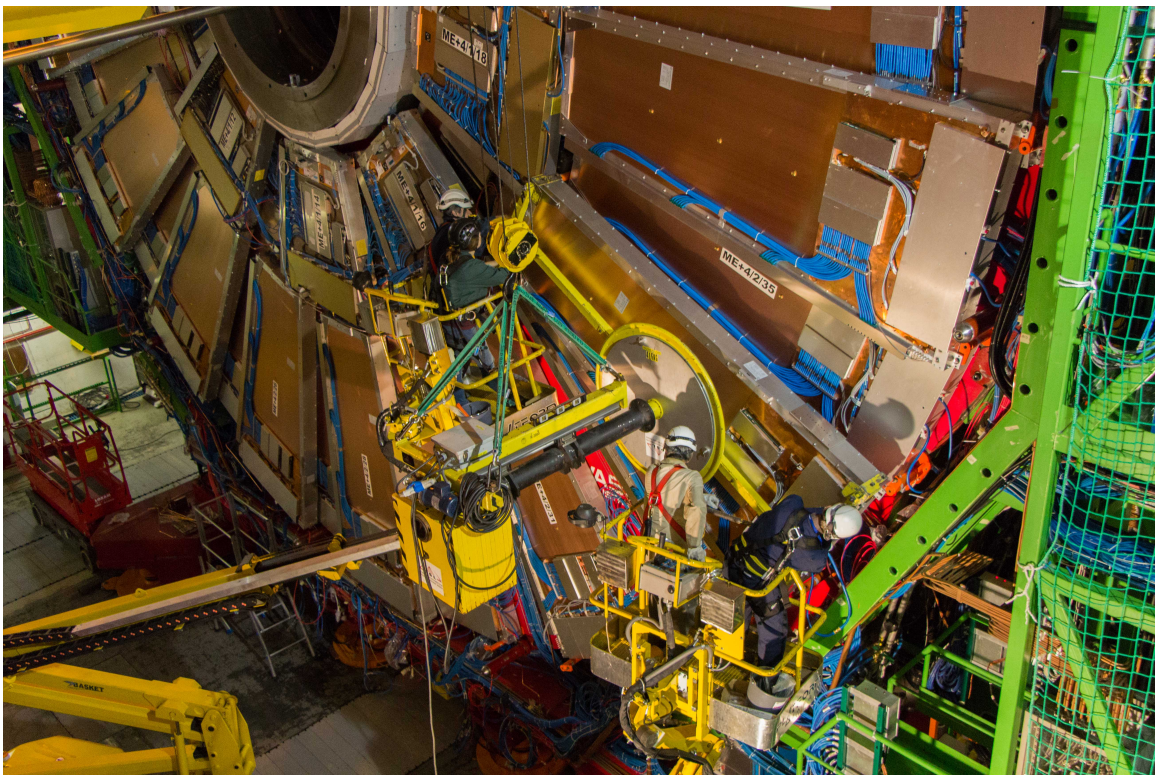

Figure F.1: The CSC installation team attaching a chamber to its position on the ME4/2 ring.

Each chamber weighs $\approx$ 400 kg and needs to be lifted into its proper place, rotated, and attached to mounting posts on the YE3 ring. This involves the use of a custom, counter-weighted lifting fixture. This fixture, shown in Figure F.3, has the ability to rotate the chamber about its center so that it can be oriented with the narrow side pointing to the center of the ring. Additionally, the attachment point of the crane can be moved forward

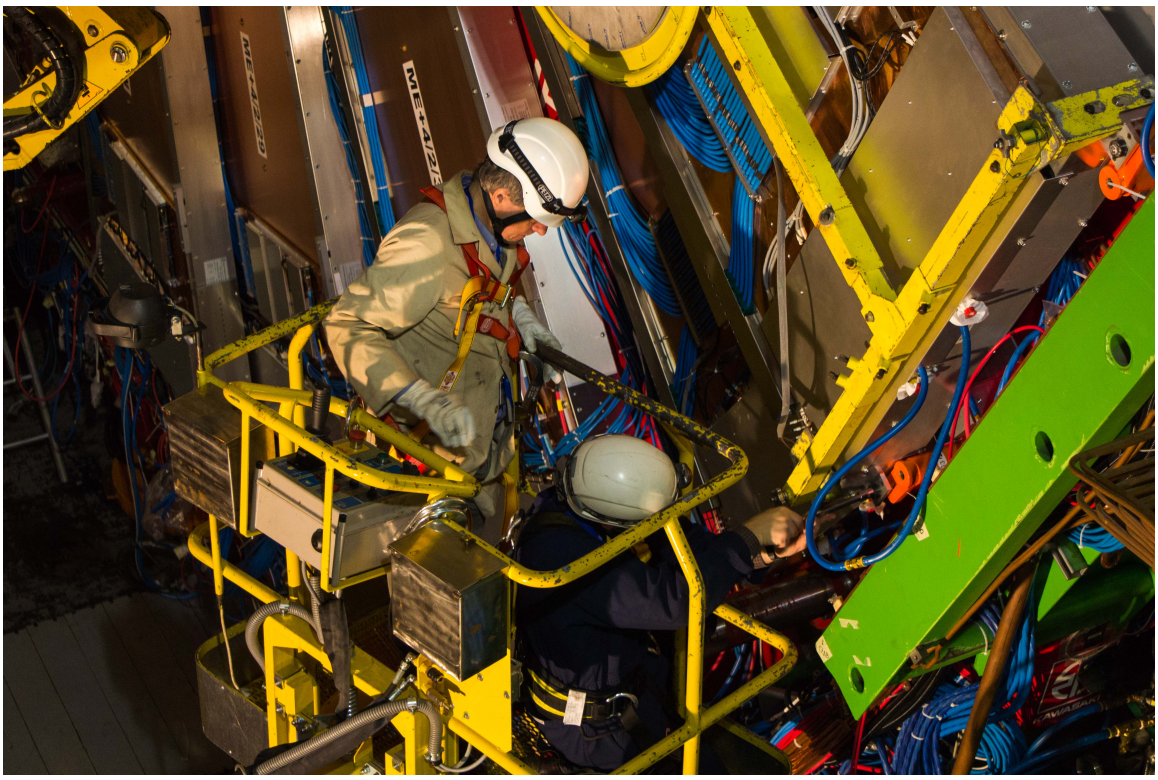

Figure F.2: Closeup of part of the installation team attaching a chamber to its position on the ME4/2 ring.

Figure F.3: A closeup of the crane fixture used to install CSCs in the CMS Cavern.

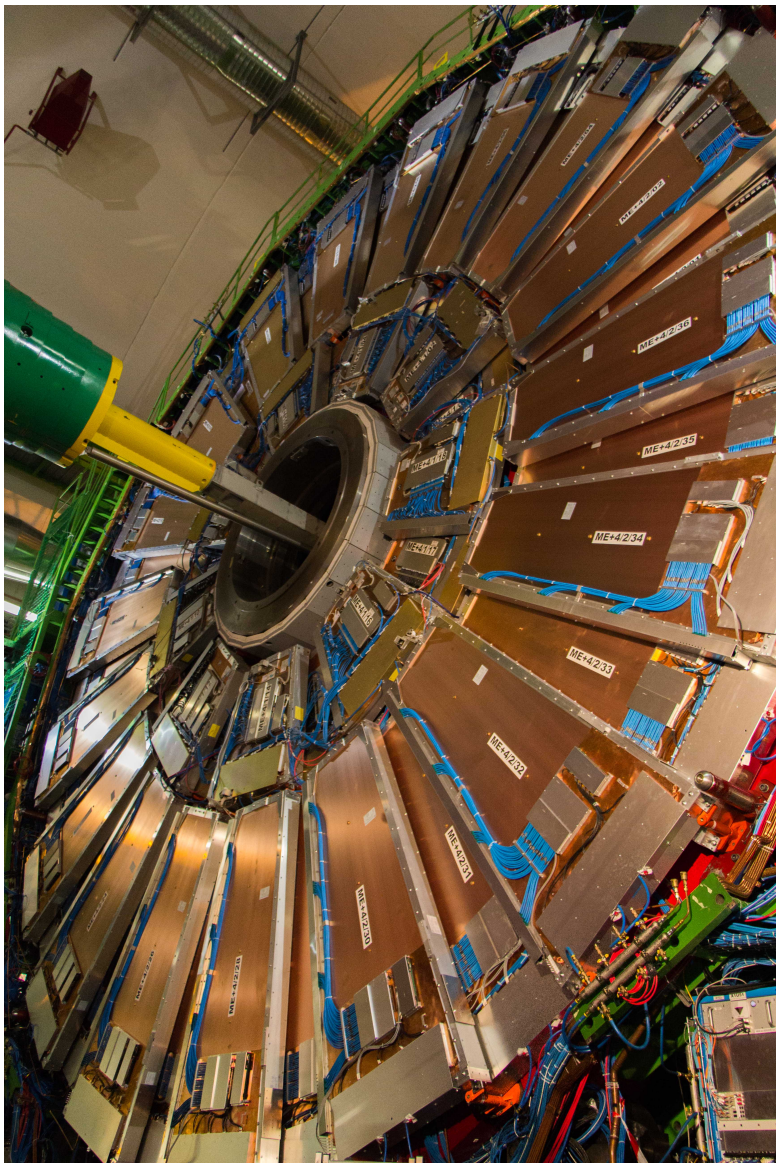

Figure F.4: One of the completed ME4/2 rings after all chambers have been installed.

and backward, with respect to the chamber-counterweight axis, through an electric motor. This allows for the chamber's angle with respect to the YE3 disk to be adjusted as it is not normal to the cavern floor. Once the chamber is fixed to the mounting posts, the balance of the fixture must them be moved again, so that the fixture can be safely extracted from the disk interface.

Once the chambers were fixed onto the YE3 disks, we connected all the cabling and services so that the chambers could be commissioned and eventually take data. One of the completed ME4/2 rings is shown in Figure F.4.

The chambers were commissioned and tested in tandem with the data acquisition system for several months until the LHC was ready to begin the RunII commissioning phase. During this time, I served as an on-call expert (DOC). DOC shifts lasted a week and over the course of 2014 and 2015 I served as DOC for several shift periods. During this time, the DOC is on call 24 hours a day and spends the work day in the CMS control room monitoring the CSCs and coordinating commissioning efforts with other experts. Perhaps the most exciting DOC shift I served on was during the first 'splashes' of RunII.

Splashes is the term given to a stage of the LHC commissioning where the beams, at low energy, are deflected into the columnators just outside of the IPs. This allows the LHC to test the magnet systems as well as measure the current of the bean as it is deflected. For CMS, this means that a large 'splash' of particles goes through the detector and acts as a first test with real particles from the LHC triggering the detectors. The CSCs performed very well during these first splashes and went on to begin providing quality data once nominal collisions began.